UNIVERSITÀ
DI PAVIA

Dipartimento di Fisica

Master's Degree in Physical Sciences

NMR relaxation profiles: role of Brownian and Néel correlation times in Au-Fe magnetic nanoparticles

MSc thesis by:

Marco Pacini

Supervisor:

Prof. Alessandro Lascialfari

Co-supervisors:

Dr. Margherita Porru

Dr. Francesca Brero

A.Y. 2024 – 2025

Abstract

Magnetic nanoparticles (MNPs), particularly hybrid systems composed of gold and iron oxide, are of growing interest in biomedical applications due to their multifunctional capabilities. Among their many uses, Magnetic Resonance Imaging (MRI) exploits the magnetic properties of such nanoparticles for diagnostic purposes, like enhancing image contrast. MRI is based on Nuclear Magnetic Resonance (NMR), a technique that probes the relaxation behavior of proton spins in response to magnetic field perturbations. This thesis investigates Au–Fe_3O_4 nano-heterostructures as potential MRI contrast agents, with a particular focus on their NMR relaxation profiles and the respective contributions of Brownian and Néel correlation times to their relaxivity behavior.

Two main types of hybrid nanoparticles were studied: dumbbell-like Au-Fe_3O_4@CTAB (DB) and nano-urchin-like Au-Fe_3O_4@PEG (NU), all featuring a magnetite core with an average diameter of 11.6 nm. A total of four samples were investigated: one aqueous dispersion of dumbbell-like particles (DB_0.1_H_2O), two agarose gel dispersions of dumbbell-like particles at different iron concentrations (0.1 and 0.2 mM), and one sample of nano-urchin-like particles embedded in agarose gel (concentration < 0.1 mM). Agarose gel was chosen as a tissue-mimicking medium due to its biocompatibility and diffusion properties comparable to the tumor extracellular matrix.

A comprehensive morphological, structural, magnetic, and relaxometric characterization was performed. Transmission Electron Microscopy (TEM) provided morphological information, X-Ray Diffraction (XRD) confirmed the crystal structure, and SQUID magnetometry assessed magnetic behavior and properties. Longitudinal and transverse NMR relaxation profiles (r_1 and r_2) were acquired across a wide range of Larmor frequencies using Fast Field Cycling (FFC) and NMR spectrometers.

To interpret the relaxation behavior, a semi-empirical heuristic model (Roch-Müller-Gillis) was employed and later modified to account explicitly for both Néel and Brownian relaxation mechanisms through their respective correlation times. At 63.864 MHz, the dumbbell nanoparticles in aqueous dispersion exhibited the highest transverse relaxivity ($r_2 \sim 364\ s^{-1}mM^{-1}$) and a

large r_2/r_1 ratio of (about) 85, indicating strong T_2 contrast efficiency. When embedded in 1% agarose, both r_1 and r_2 decreased ($r_2 \sim 150$–175 $s^{-1}mM^{-1}$), consistent with the reduced Brownian motion and partial immobilization of the particles in the gel matrix. The nano-urchin particles showed significantly lower relaxivities at 63.864 MHz compared to the dumbbells ($r_2 \sim 72.5$ $s^{-1}mM^{-1}$), probably due to the higher amount of gold present in the urchin shape that might further reduce the Brownian rotation.

The DB_0.1_mM_H_2O was compared to the relaxivity of a retired contrast agent called ENDOREM. Our sample showed a transverse relaxivity ~3 times larger than the r_2 values (in the range 7.2 - 63.864 MHz) of ENDOREM, reflecting its potential as T_2-relaxing agent.

The modified model enabled the extraction of key physicochemical parameters such as saturation magnetization, effective core radius, and characteristic relaxation times. The fitting parameters obtained from the RMG model (and its variants) have shown values of $\tau_B \sim 3{\cdot}10^{-6}$ s in water and $2{\cdot}10^{-5}$ s in agarose for dumbbell dispersions, while a value of $5.6{\cdot}10^{-5}$ s for the nano-urcins sample was found, resulting in the longest Brownian relaxation time (as expected from the nanoparticle with the largest hydrodynamic radius). Respectively, τ_N remained in the same order of magnitude, varying from $2.3{\cdot}10^{-8}$ s (for the dumbbell dispersion in water) to nearly $3{\cdot}10^{-8}$ s for the agarose dispersions, as expected for the same particles in different media. The analysis highlighted the influence on the particles spin dynamics due to a specific environment (liquid vs. gel) and to their morphology, demonstrating that when Brownian rotation is restricted (as in agarose gels) the Néel mechanism becomes more and more dominant.

Contents

INTRODUCTION

Magnetic Resonance Imaging (MRI) is a non-invasive imaging technique applied in diagnostics, which utilises magnetic fields and radiofrequency (RF) pulses to probe the spin dynamics of hydrogen nuclei (protons), providing detailed anatomical and functional information. The Nuclear Magnetic Resonance (NMR), *i.e.*, physical principle of MRI, describes the behavior of nuclear spins in an external magnetic field and their subsequent relaxation following RF excitation. Through the application of spatially varying magnetic field gradients, the NMR signal can be spatially encoded to reconstruct images in which contrast directly reflects the local relaxation properties of tissues.

The ability of MRI to discriminate between soft tissues comes from differences in proton density (ρ), in the T_1 (longitudinal) and T_2 (transverse) nuclear relaxation times. These intrinsic relaxation parameters govern how rapidly the excited proton spins return to equilibrium. However, in the majority of clinical cases, (*e.g.*, the detection of early-stage tumors or small lesions) the natural contrast of biological tissues is not sufficient to clearly distinguish pathological regions. To overcome this limitation, it is possible to administer exogenous contrast agents (CAs), to locally alter the relaxation rates of surrounding water protons, increasing both image contrast and diagnostic sensitivity.

The two major classes of contrast agents (CAs) used in clinics are: T_1-relaxing agents, which are typically gadolinium-based complexes, and T_2-relaxing agents, which are typically superparamagnetic iron oxide-based nanoparticles (SPIOs). These latter are very effective because of their high magnetic moments that generate strong local magnetic field inhomogeneities, leading to rapid dephasing of neighboring proton spins. Over the past few years, research has been focused on the synthesis of *hybrid* nanoparticles that combine magnetic and non-magnetic components to achieve multifunctionality. Among these, gold–iron oxide (Au–Fe_3O_4) nanostructures have attracted particular interest because they combine the magnetic properties of iron oxide with the plasmonic and biocompatibility of gold, enabling applications in imaging and therapy.

This thesis focuses on the study of the relaxometric behavior of Au–Fe_3O_4 nano-

heterostructures, with particular attention to their potential as T_2-weighted MRI contrast agents. Two different morphologies were investigated: dumbbell-shaped Au–Fe_3O_4@CTAB nanoparticles and nano-urchin-shaped Au–Fe_3O_4@PEG nanoparticles. The two systems share the same magnetite core with an average diameter of 11.6 nm. A total of four samples were analyzed: an aqueous dispersion of dumbbell-like nanoparticles (DB 0.1 H_2O), two samples of dumbbell-like nanoparticles embedded in agarose gel at different iron concentrations (0.1 and 0.2 mM), and one samples of agarose-embedded nano-urchin-like particles at a concentration below 0.1 mM. The agarose gel was selected as a tissue-mimicking environment, as it reproduces the diffusion properties and microstructure of biological tissues, providing a more realistic evaluation of the performance of nanoparticles *in vitro*.

All the samples analyzed in this thesis were subjected to a full physicochemical and magnetic characterization. The particle size and the morphology were analyzed through Transmission Electron Microscopy (TEM), and X-Ray Diffraction (XRD) was used to verify the crystalline phase of magnetite. Magnetic measurements were performed using a Superconducting Quantum Interference Device (SQUID) magnetometer, and showed a typical superparamagnetic behavior at room temperature. Relaxometric data were collected by measuring the longitudinal (r_1) and transverse (r_2) nuclear relaxation rates over a broad range of frequencies, providing the Nuclear Magnetic Relaxation Dispersion (NMRD) profiles of each sample.

To interpret the experimental NMRD data, a semi-empirical model originally proposed by Roch, Müller and Gillis (RMG) was used and subsequently adapted to explicitly include both Néel and Brownian relaxation mechanisms through their respective correlation times. This extended model allows one to evaluate how the local spin dynamics of nanoparticles is influenced by the surrounding medium. The analysis demonstrated that in aqueous environments, where Brownian rotation is unhindered, both mechanisms contribute to the overall relaxation; whereas in gel matrices, Brownian motion is largely suppressed, making Néel fluctuations the dominant relaxation process. From the model fitting, key parameters such as saturation magnetization, effective magnetic radius, and characteristic correlation times were extracted, providing valuable information on the relationship between structural and spin dynamics governing MRI contrast efficiency.

Thesis Overview

This thesis is divided into the following chapters:

- **Chapter 1** provides an overview of magnetism and magnetic materials, focusing on their characterizing interactions, *e.g.*, dipole-dipole, spin-orbit and exchange interaction. Details about their main properties and hysteresis loops are also discussed.

- **Chapter 2** introduces the fundamental principles of nanomagnetism, focusing on single-domain particles and the phenomenon of superparamagnetism, which plays a crucial role in biomedical applications, such as diagnostics and targeted therapy.
- **Chapter 3** presents the theoretical basis of Nuclear Magnetic Resonance (NMR) and relaxometry, discussing the main relaxation mechanisms and models used to interpret the relaxivity of magnetic nanoparticles.
- **Chapter 4** discusses the physico-chemical properties of magnetic nanoparticles relevant to the biomedical field of interest, outlining their applications in Magnetic Resonance Imaging (MRI) and Magnetic Fluid Hyperthermia (MFH), with special emphasis on gold–iron oxide hybrid nanoparticles.
- **Chapter 5** details the experimental methods and instrumentation used for this research, including synthesis protocols, structural and magnetic characterization techniques, and the setup of NMR relaxometric measurements over different frequency ranges.
- **Chapter 6** presents and discusses the experimental results, which include morphological, magnetic and relaxometric characterizations, followed by the analysis of the NMRD profiles using the heuristic Roch, Müller and Gillis model and its modified versions.

CHAPTER 1

FUNDAMENTALS OF MAGNETISM

The study of magnetism has played a fundamental role in both classical and modern physics. Understanding the origin and behavior of magnetic phenomena is essential not only for interpreting a wide range of physical systems, but also for the design of advanced materials and technologies. In particular, magnetic interactions at the atomic scale give rise to collective behaviors, such as ferromagnetism, antiferromagnetism and ferrimagnetism, which can be described using theoretical models based on exchange interactions and statistical mechanics.
This chapter provides a general overview of the fundamental principles of magnetism. Starting from the atomic origin of magnetic moments, we describe the main theoretical models that explain their macroscopic properties. Concepts such as magnetic susceptibility, the Langevin model, exchange coupling, and the formation of magnetic domains are introduced as a basis for understanding more complex behaviors [1]. These classical concepts lay the groundwork for the following chapters, where we will explore how magnetism changes at the nanoscale and how such effects are exploited in biomedical applications.

1.1 Magnetic properties of matter

Magnetism in matter arises from the motion of electric charges, which can be treated as current loops generating magnetic dipoles [2]. Most materials do not exhibit macroscopic magnetism, generally because their magnetic moments tend to cancel out unless an external magnetic field is applied to align them, thereby creating a net magnetization. From a classical point of view, matter consists of negatively charged electrons orbiting around nuclei composed of positively charged protons and neutral particles called neutrons. The intrinsic rotation of electrons about their own axis, called spin (a quantum mechanical quantity with the properties of angular momentum),

together with their orbital angular momentum, is responsible for magnetism at the microscopic scale. At the macroscopic level, the magnetic behavior depends on the atomic structure of the material and on the interactions among the magnetic moments.

1.1.1 Magnetic moment and magnetization

Atoms or ions are described by their **magnetic moment**, defined as:

$$\vec{\mu} = \gamma\hbar\vec{J} = \gamma\hbar(\vec{L} + \vec{S}) \tag{1.1}$$

where $\vec{J} = \vec{L} + \vec{S}$ is the total angular momentum, given by the sum of the orbital angular momentum $\vec{L}$ and the spin angular momentum $\vec{S}$, $\hbar$ is the Planck constant ($6.626 \cdot 10^{23}$) and γ is the gyromagnetic ratio of the electron. This ratio is defined by the Landé factor g (which is $\simeq 2$ for electrons) and the Bohr magneton μ_B, such that $\gamma = -\frac{\mu_B g}{\hbar}$, with:

$$\mu_B = \frac{e\hbar}{2m} = 9.274 \cdot 10^{-24} Am^2 \tag{1.2}$$

where e is the elementary charge and m is the electron mass [2].

Since most studies deal with complex systems constituted by interacting nuclei rather than isolated atoms, the magnetic properties of a material are described based on their **magnetization** $\vec{M}$:

$$\vec{M} = \frac{\sum_i^n \vec{\mu}_i}{V} \tag{1.3}$$

The magnetization represents the medium magnetic moment per unit volume, whereas its average value describes the internal order of a magnetic system:

- $\langle\vec{M}\rangle = 0$: magnetic moments in the volume are randomly oriented, indicating a disordered state;
- $\langle\vec{M}\rangle \neq 0$: magnetic moments are aligned along a certain direction, indicating instead an ordered state of the system.

When exposed to an external magnetic field $\vec{H}$, the magnetic moments tend to align with that field, generating an additional field called magnetic induction field $\vec{B}$, given by:

$$\vec{B} = \mu_0(\vec{H} + \vec{M}) \tag{1.4}$$

with $\mu_0 = 4\pi \cdot 10^{-7}$ H/m (the vacuum permeability), and where $\vec{M}$ and $\vec{H}$ are expressed in A/m, and $\vec{B}$ in Tesla (T).

Not all materials respond in the same way to an external field; this depends on their atomic structure. The main quantity used to describe their response, also known as the system's response

function, is the **magnetic susceptibility** χ (dimensionless in the SI):

$$\overline{\overline{\chi}} = \frac{\partial \vec{M}}{\partial \vec{H}} \tag{1.5}$$

For small values of $\vec{H}$, the susceptibility can also be approximated as:

$$\overline{\overline{\chi}} \simeq \frac{\vec{M}}{\vec{H}} \quad \rightarrow \quad \vec{M} \simeq \chi \vec{H} \tag{1.6}$$

Magnetic susceptibility values describe how the system responds to an applied magnetic field: positively, if the magnetic moments align with the field (also known as paramagnetic behavior), or negatively, if they oppose it and tend to disalign along another direction (diamagnetic behavior) [3], [4]. Typical magnetic susceptibility values vary depending on the magnetic behavior of the material. Paramagnetic systems exhibit positive susceptibilities, generally ranging from 10^{-6} to 10^{-1}, while diamagnetic materials show negative susceptibilities, typically between -10^{-6} to -10^{-3}.

1.2 Magnetic interactions

In order to understand the behavior of the different magnetic systems, it is necessary to introduce and describe the main interactions that occur inside them. The magnetic moments in the medium interact through long or short range interactions: **dipolar**, **spin-orbit** and **exchange interaction** [4].

1.2.1 Dipolar interaction

The magnetic dipolar interaction originates from the mutual influence between two (or more) magnetic moments, $\vec{\mu_1}$ and $\vec{\mu_2}$, at distance $\vec{r}$, that produces an energy E describable as:

$$E = \frac{\mu_0}{4\pi r^3}[\vec{\mu_1} \cdot \vec{\mu_2} - \frac{3}{r^2}(\vec{\mu_1} \cdot \vec{r})(\vec{\mu_2} \cdot \vec{r})] \tag{1.7}$$

The energy E scales with the third power of the distance r, implying a low contribution if the two moments are treated as independent, or sufficiently distant, inside the medium; only for temperatures inferior to milliKelvin, this effect becomes appreciable and can be compared to the other interactions.

1.2.2 Exchange interaction

Exchange interaction is an electrostatic interaction dominating at long range, that influences the magnetic moment orientations [4]. Let's consider, for the simplest case, two interacting electrons described by the spatial coordinates $\vec{r_1}$ and $\vec{r_2}$. The spatial wave-function used to describe the joined states can be obtained from the product of the two single electron states, such that:

$$\psi(\vec{r_1}, \vec{r_2}) = \psi_A(\vec{r_1})\psi_B(\vec{r_2}) \tag{1.8}$$

where A and B are the respective electronic states. Since the two electrons are indistinguishable from the quantum-mechanics point of view, the probability of finding the first electron in the second electron position (and vice versa) has to be the same, so it follows:

$$|\psi(\vec{r_1}, \vec{r_2})|^2 = |\psi(\vec{r_2}, \vec{r_1})|^2 \tag{1.9}$$

bringing to:

$$\psi(\vec{r_1}, \vec{r_2}) = \pm\psi(\vec{r_2}, \vec{r_1}) \tag{1.10}$$

If we exchange the position of the two electrons, $\vec{r_1}$ with $\vec{r_2}$, the only states allowed are those that are symmetric or antisymmetric to coordinate exchange; however, this is not what we get if we perform the exchange of the two particle states, obtaining instead: $\psi(\vec{r_2}, \vec{r_1}) = \psi_A(\vec{r_2})\psi_B(\vec{r_1})$. For electrons (*i.e.*, fermions), the total wave-function Ψ has to be anti-symmetric, due to their half-integer spin. It can be separated in two components: an orbital one (described previously as $\psi(\vec{r_1}, \vec{r_2})$), related to the spatial coordinates of the two particles, and a spin one χ related to spin, such that:

$$\Psi(1,2) = \psi(\vec{r_1}, \vec{r_2})\chi(1,2) = -\Psi(2,1) \tag{1.11}$$

For the spin component, there are two possible states:

- **Singlet state**, with eigenvalue S = 0 related to the operator $S^2 = (S_1 + S_2)^2$
- **Triplet state**, with eigenvalue S = 1.

The first one has anti-symmetric spin component, so the spatial component has to be symmetric in order to achieve the anti-symmetry of the final wave-function, usually referred to as:

$$\Psi_S = \frac{1}{\sqrt{2}}[\psi_A(\vec{r_1})\psi_B(\vec{r_2}) + \psi_A(\vec{r_2})\psi_B(\vec{r_1})]\chi_S \tag{1.12}$$

On the other side, the triplet state wave function has an anti-symmetric spatial component and a symmetric spin one. So:

$$\Psi_T = \frac{1}{\sqrt{2}}[\psi_A(\vec{r_1})\psi_B(\vec{r_2}) - \psi_A(\vec{r_2})\psi_B(\vec{r_1})]\chi_T \tag{1.13}$$

At this point the energies related to the two possible states can be calculated as:

$$E_S = \int \Psi_S^* U(\vec{r_1} - \vec{r_2})\Psi_S \, d\vec{r_1} d\vec{r_2} \tag{1.14}$$

$$E_T = \int \Psi_T^* U(\vec{r_1} - \vec{r_2})\Psi_T \, d\vec{r_1} d\vec{r_2} \tag{1.15}$$

where $U(|\vec{r_1} - \vec{r_2}|) = \frac{1}{4\pi\epsilon_0}\frac{q^2}{|\vec{r_1} - \vec{r_2}|}$ is the electrostatic potential energy between the two charged particles.
The energy difference of the two states can be then expressed in terms of the exchange integral:

$$E_S - E_T = 2\int \psi_A^*(\vec{r_1})\psi_B^*(\vec{r_2})U(\vec{r_1} - \vec{r_2})\psi_B(\vec{r_2})\psi_A(\vec{r_1})d\vec{r_1}d\vec{r_2} \tag{1.16}$$

From which the solution can be expressed as the **exchange constant** J:

$$J = \frac{E_s - E_T}{2} \tag{1.17}$$

The exchange energy, introduced to describe the coupling of the electron spins, can be re-formulated with the use of J as:

$$H = -2J\vec{S_1} \cdot \vec{S_2} \tag{1.18}$$

For $J > 0$, $E_s > E_T$, so the triplet state with S = 1 is energetically preferred; vice versa, for $J < 0$, $E_s < E_T$, implying that the singlet state with S = 0 is the favored one [4].

Extending the discussion to a system of N magnetic moments, represented by N neighboring atoms, the Hamiltonian of the **Heisenberg** model is given by the summation of all the exchange constants over the N atoms:

$$H_{Heisemberg} = -\sum_{i,j} J_{ij}\vec{S_i} \cdot \vec{S_j} \tag{1.19}$$

where the factor 2 is omitted, as each pair of spins is counted only once.

1.2.3 Spin-orbit interaction

The spin-orbit interaction arises from the relative orbital motion of an electron (and its spin) around the nucleus, causing a coupling between the nuclear magnetic field and its magnetic

moment:

$$\vec{B} = \frac{\vec{E} \times \vec{v}}{c^2} \tag{1.20}$$

where $\vec{E} = -\vec{\nabla}V(r)$ is the electric field felt by the electron (electron's reference frame) due to its interaction with the charged nucleus and where $V(r)$ is the electric potential generated in the space by the charged nucleus [5].
The Hamiltonian of the interaction is then described by:

$$H_{SO} = -\frac{1}{2}\vec{\mu} \cdot \vec{B} = A\vec{S} \cdot \vec{L} \tag{1.21}$$

where $A \propto \frac{1}{r}\frac{dV(r)}{dr}$, $\hbar\vec{L} = m_e\vec{r} \times \vec{v}$ is the angular orbital momentum of the electron, $\vec{\mu} = \frac{ge\hbar}{2m}\vec{S}$ the magnetic momentum of the electron and 1/2 is a relativistic correction term [4].

1.3 Classification of magnetic materials

As it was discussed in the first paragraph, it is possible to observe in nature more than one kind of magnetic behavior. They originate due to their microscopic properties, such as the number of unpaired electrons or the presence of internal constraints, and can be distinguished based on their response to an external applied magnetic field.
The magnetic response of a material depends on its magnetic susceptibility, which is capable of directly influencing the magnetic moments inside the medium and force them to change their orientation.
Magnetic materials can be broadly classified in three main categories: **paramagnetic**, **diamagnetic** and **ferromagnetic**, where the last one comprises two related cases, anti-ferromagnetic and ferrimagnetic materials, that will be discussed [1].

1.3.1 Paramagnetism

Paramagnetism arises from the presence of unpaired electrons inside the atomic structure, which will give a non-zero net magnetic moment. Their interaction with the nearby atoms is relatively weak and, without an external magnetic field, those spins are free to point in any direction and distribute casually in space, as they can be considered independent from each other [4].

Following the application of an external field, the unpaired electrons respond positively to the perturbation, resulting in a positive magnetic susceptibility. As a consequence, the magnetic moments partially tend to align with the direction of the applied field, with a degree of alignment that depends on the field strength and temperature.

From the quantum mechanics point of view, the application of an external magnetic field generates a Zeeman energy $E = -\vec{\mu} \cdot \vec{B} = g\mu_B m_j B$, where m_j is the azimuthal quantum number

associated to the total angular momentum $\vec{J} = \vec{L} + \vec{S}$ and that ranges from $-J, -J+1, ..., +J$. This leads to a splitting of the states into $(2J+1)$ equally spaced energy levels, where the lowest energy state is the most probable at null temperature.

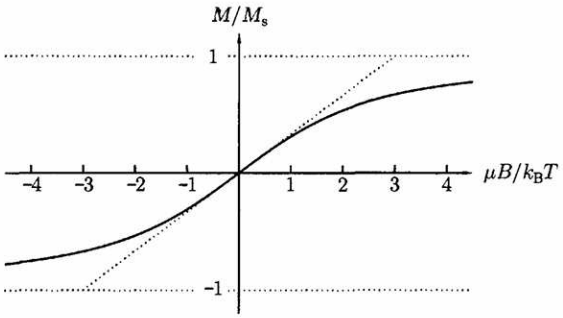

Figure 1.1: *Langevin function $L(y) = coth(y) - \frac{1}{y}$, M_s is the saturation magnetization, the maximum magnetization obtainable when all the spins in the medium are aligned [4].*

Using the semi-classical approach, it is possible to obtain the curve that described the magnetization as a function of the applied magnetic field H. Considering a number N of atoms, the mean statistical moment $\langle \mu_z \rangle$ is defined as:

$$\langle \mu_z \rangle = \frac{\sum_i^N \mu_{i,z} e^{\frac{-E_i}{K_B T}}}{\sum_i^N e^{\frac{-E_i}{K_B T}}} \tag{1.22}$$

with $E_i = -\vec{\mu_{i,z}} \cdot \vec{B}$. The result of the summation brings to the so-called **Langevin function** $L(y)$:

$$L(y) = \coth(y) - \frac{1}{y} = \frac{\langle \mu_z \rangle}{\mu} \tag{1.23}$$

with $y = \frac{\mu B}{K_B T} = \frac{g_L J \mu_B B}{K_B T}$ and $k_B = 1.38 \cdot 10^{-23}$ J/K the Boltzmann constant, which describes the behavior of paramagnetic magnetization as a function of the external field H and the temperature T of the system (Figure 1.1).
However, the Langevin function can be considered a special case, when $J \to \infty$ (corresponding to a large number of unpaired electrons), of another function, named **Brillouin function** $B(y)$, which also describes the behavior of an ideal paramagnet, but using a formulation that originates from the quantum mechanics:

$$B(y) = \frac{2J+1}{2J} \coth\left(\frac{(2J+1)y}{2J}\right) - \frac{1}{2J} \coth\left(\frac{y}{2J}\right) \tag{1.24}$$

For y $\ll 1$, which corresponds to sufficiently high temperatures, the Brillouin function can be expanded using the Taylor's series, leading to the expression for the magnetic susceptibility for

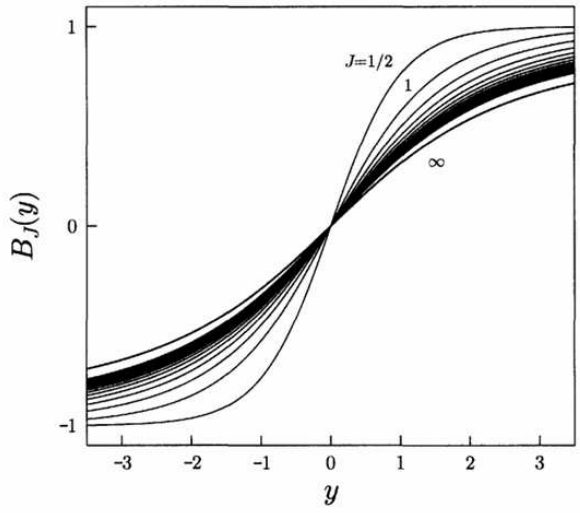

Figure 1.2: *Brillouin function $B_J(y)$, that ranges from $J = 1/2$ to $J \to \infty$. For the case $J = 1/2$, the function reduces to $B_{1/2}(y) = \tanh(y)$ [4].*

an ideal paramagnet at temperature T:

$$\chi = \frac{M}{H} = \frac{M_s B(y)}{H} \simeq \frac{g^2 \mu_B^2 N J(J+1)}{3K_B T} \sim \frac{C}{T} \tag{1.25}$$

also called **Curie's law**, which relates temperature with magnetic susceptibility. It shows the decrease in χ with increasing temperature of the system (Figure 1.2).

1.3.2 Diamagnetism

Diamagnetism exhibits a magnetic response opposite to that of paramagnetic systems when exposed to an external magnetic field. In this case, the atomic structure contains no unpaired electrons, resulting in a null net magnetic moment and, consequently, a tendency to oppose external magnetic perturbations.

When an external field is applied, it slightly perturbs the orbital motion of the electrons, thereby altering the magnetic flux generated by the circulating current of these charged particles. As a consequence, an electromotive force (EMF) is induced, in accordance to the Lenz's law, as a response to the applied field. This induced current generates a magnetization opposite to the external field, which is directly proportional to the field strength. Therefore, the magnetic susceptibility, defined as the ratio between the magnetization and the applied field [4] [1], is negative for diamagnetic materials:

$$\chi \simeq \frac{M}{H} < 0 \tag{1.26}$$

1.3.3 Ferromagnetism

Ferromagnets are characterized by the presence of unpaired electrons, like in the case of paramagnets, presenting at the same time an internally ordered structure known as **Weiss domains** [4]. Within these domains, a large number of atomic spins are enclosed and aligned, producing a net magnetization in a specific region of this material. The primary interaction responsible for this ordering and for the appearance of a spontaneous magnetization is the exchange interaction.

When an external field is applied, the resulting Hamiltonian can be described as follows:

$$H = -\sum_{i,j} J_{ij}\vec{S}_i \cdot \vec{S}_j + g\mu_B \sum_j \vec{S}_j \cdot \vec{B} \tag{1.27}$$

consisting of two contributions: the Heisenberg exchange interaction and the Zeeman interaction. The exchange constants J_{ij} that characterize the Hamiltonian are strictly positive, indicating that neighboring spins tend to align in the same direction [4].

In the Weiss model, assuming $L = 0$ for which $\vec{J} = \vec{L} + \vec{S} = \vec{S}$, the Heisenberg term can be rewritten in the form of a Zeeman Hamiltonian. It is assumed that, at the i-th site of the ferromagnetic crystal, all neighboring spins generate an effective molecular magnetic field $\vec{B_{\text{mf}}}$:

$$\vec{B_{mf}} = -\frac{2}{g\mu_B}\sum_j J_{i,j}\vec{S}_j = \lambda\vec{M} \tag{1.28}$$

where λ is a positive constant that characterizes the strength of the molecular field for ferromagnets.

Using the previous relation, the original Hamiltonian becomes:

$$H = g\mu_B \sum_i \vec{S}_i \cdot (\vec{B} + \vec{B_{mf}}) \tag{1.29}$$

which has the form of a paramagnet Hamiltonian in an effective magnetic field $\vec{B_{tot}} = \vec{B} + \vec{B_{mf}}$.

When an external field is applied, the spins tend to align along its direction, creating a total net magnetization M_S known as the **saturation magnetization**; when it is removed, the crystal may still exhibit residual magnetization, and to completely reset the system to its original null total magnetization, a certain magnetic field has to be applied in the opposite direction, referred to as **coercive field** H_C.

The model's solution is achieved by solving the two equations:

$$\frac{M}{M_s} = B_J(y), \quad y = \frac{g_j\mu_B J(B + \lambda M)}{k_B T} \tag{1.30}$$

with $M_s = \mathrm{N}\, g_j\mu_B J$.

As shown in Figure 1.3, assuming $B = 0$, three different behaviors can be observed depending on

the temperature relative to the Curie temperature T_c.

- For $T > T_c$, the system has only one solution: $y = 0$, hence $M = 0$.
- For $T < T_c$, three solutions are found: $y = 0$ and $y = \pm M_s$, indicating spontaneous magnetization.
- For $T = T_c$, in proximity of the origin, the curve and the Brillouin function have the same slope.

According to the Weiss model, at temperatures higher than T_c, thermal agitation dominates and erases residual magnetization. However, below T_c, the exchange interaction sustains spontaneous magnetization, even in the absence of an external field, due to the presence of the molecular field $\vec{B}_{\mathrm{mf}}$.
For small y, the Brillouin function can be approximated to:

$$B_J(y) \simeq \frac{(J+1)y}{3J} + O(y^3) \tag{1.31}$$

from which it is possible to define the Curie's temperature as:

$$T_c = \frac{g\mu_B(J+1)\lambda M_s}{3k_B} = \frac{g^2\mu_B^2 J(J+1)\lambda N}{3k_B} \tag{1.32}$$

The magnetic susceptibility for a ferromagnet can be deduced starting from:

$$\frac{M}{M_s} \simeq \frac{T_c}{\lambda M_s}\left(\frac{B+\lambda M}{T}\right) \tag{1.33}$$

which can be rearranged as:

$$\frac{M}{M_s}\left(1 - \frac{T_c}{T}\right) \simeq \frac{T_c B}{\lambda M_s} \tag{1.34}$$

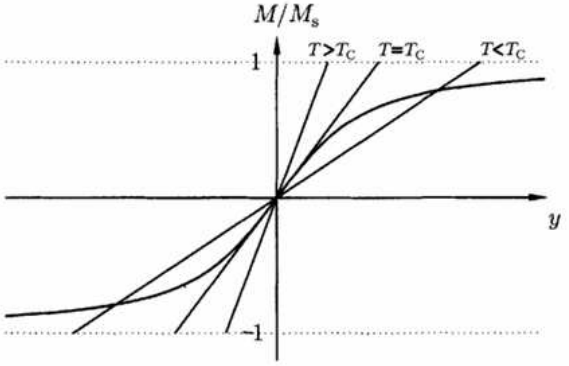

Figure 1.3: *Magnetization curve of a ferromagnet as a function of y with $B = 0$ [4].*

so that, in the limit of small B, this leads to the **Curie–Weiss law** for ferromagnets [2]:

$$\chi = \lim_{B->0} \frac{\mu_0 M}{B} \sim \frac{1}{T - T_c} \tag{1.35}$$

1.3.4 Anti-ferromagnetism and ferrimagnetism

Two notable cases of magnetic ordering that deserve to be mentioned are **anti-ferromagnetism** and **ferrimagnetism**.

Anti-Ferromagnetism occurs in materials characterized by a negative exchange constant (*i.e.*, $J < 0$), where adjacent magnetic moments tend to arrange in an anti-parallel configuration. This behavior arises because antiferromagnetic materials typically consist of atoms distributed over two interpenetrating sub-lattices that occupy distinct positions within the crystal lattice. Similar to ferromagnets, one can introduce a molecular magnetic field experienced by neighboring atoms for each sub-lattice (parallel and antiparallel) that can be expressed as:

$$B_+ = -|\lambda| M_- \quad , \quad B_- = -|\lambda| M_+ \tag{1.36}$$

where λ is now a negative constant. The magnetization resulting from the respective molecular field is given by:

$$M_\pm = M_s B_j(-\frac{g_j \mu_B J |\lambda| M_\mp}{k_B T}) \tag{1.37}$$

The two sub-lattices possess magnetization of equal magnitude but opposite orientation, such that the total magnetization can be expressed as:

$$M = M_s B_j(-\frac{g_j \mu_B J |\lambda| M}{k_B T}) \tag{1.38}$$

This expression is formally analogous to the one derived for ferromagnetic systems, suggesting that the molecular field acts with a similar mechanism. However, due to the antiparalled alignment of the sub-lattice magnetizations, the overall magnetic moment cancels out at the equilibrium and the net magnetization vanishes above a critical temperature called **Néel's temperature**, defined as:

$$T_N = \frac{g \mu_B (J+1) |\lambda| M_s}{3 k_B} \tag{1.39}$$

As in the ferromagnetic case, for small values of y, the Brillouin function can be approximated, and a Curie-like law for antiferromagnets is deduced, where the susceptibility behaves as:

$$\chi = \lim_{B->0} \frac{\mu_0 M}{B} \sim \frac{1}{T + T_c} \tag{1.40}$$

If the total magnetization of the two sub-lattices is non-zero, meaning that $\vec{M}_- + \vec{M}_+ \neq 0$, the

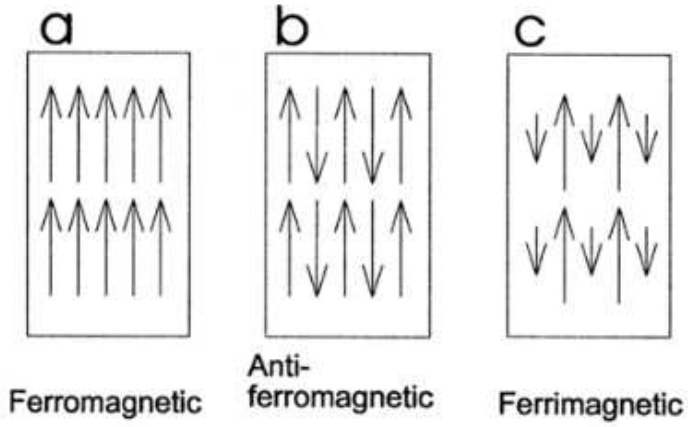

Figure 1.4: *Schematic representation of magnetic moments orientation in a ferromagnet (a), in an anti-ferromagnet (b) and in a ferrimagnet (c) [6].*

material is referred to as a ferrimagnet [4]. The magnetizations of the two sub-lattices do not completely cancel each other, giving rise to a net spontaneous magnetic moment. Since each sub-lattice contributes differently as a function of the temperature, the simple Curie–Weiss model is no longer valid for describing the thermal dependence of the magnetization in ferrimagnetic systems. A representation of these different behaviors is shown in Figure 1.4, where:

- **Case A**, the net magnetization is greater than zero (ferromagnet).
- **Case B**, total net magnetization is zero (anti-ferromagnet)
- **Case C**, typical of ferrimagnets, the magnetization is non-zero but smaller than in A.

Ferrimagnetic materials include **magnetite** (Fe_3O_4), which we will discuss in the next chapters as they constitute the magnetic core of the samples studied in this thesis project, and **maghemite** $\gamma-Fe_2O_3$, both belonging to the $ferrite$ class.

Ferrites exhibit a **spinel crystal structure** (Figure 1.5), characterized by two types of lattice sites: tetrahedral sites, coordinated by four oxygen atoms, and octahedral sites, coordinated by six [7]. The general formula for such structure is $MO{\cdot}Fe_2O_3$, where M is a divalent cation, for example Fe^{2+} or Mn^{2+}. With this provision, only 8 tetrahedral sites are occupied by cations (with four oxygen atoms nearby) while 16 positions are available in the octahedral sub-lattice (with six oxygen atoms instead) [7].

1.4 Magnetic domains and demagnetizing field

As discussed in the previous section, ferromagnets exhibit a magnetic susceptibility much greater than zero (ranging from 10^3 to 10^5), which leads to large magnetization values when an external magnetic field is applied.

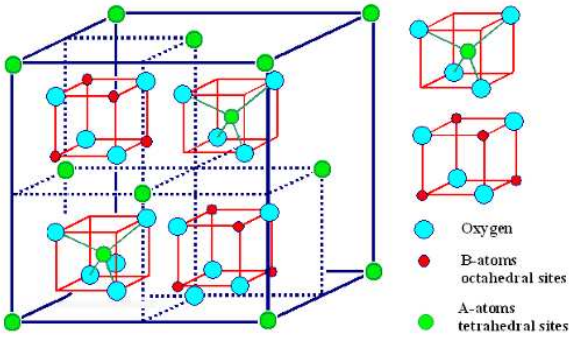

Figure 1.5: *Representation of ferrite spinel structure [7].*

1.4.1 Demagnetizing field

When a ferromagnetic material is placed in free space, a discontinuity in magnetization arises at the interface between the material and its surroundings. This discontinuity leads to a divergence in the magnetization field, described by the equation:

$$\vec{\nabla} \cdot \vec{H} = -\vec{\nabla} \cdot \vec{M} \tag{1.41}$$

which leads to the formation of a **demagnetizing field** as a response to the field generating the magnetization inside the material [4]. This insurgent field opposes the magnetic perturbation, resulting in a magnetic field of the form:

$$\vec{H} = \vec{H}_a - \vec{H}_d = \vec{H}_a - N\,\vec{M} \tag{1.42}$$

where:

- $\vec{H}_a$ is the applied external field,
- $\vec{H}_d$ is the demagnetizing field,
- N is the demagnetizing factor, determined by the specimen's shape and geometry.

The energy associated with the demagnetizing field, known as **magnetostatic energy**, is given by:

$$E_{\text{dip}} = -\frac{\mu_0}{2} \int_{\text{Vol}} \vec{M} \cdot \vec{H}_d \, \mathrm{d}\tau. \tag{1.43}$$

This term represents the energetic cost of maintaining a magnetized state in the presence of the demagnetizing field. To eliminate any residual magnetization that remains when the external field is removed, so that $\nabla \cdot \mathbf{H} \neq 0$, the magnetostatic energy must be overcome.

1.4.2 Magnetic domains

In ferromagnetic materials, a break in internal symmetry can lead to the formation of regions called **magnetic domains**, where groups of spins align collectively, giving rise to a net local magnetization (Figure 1.6). Each domain is typically magnetized up to the saturation value, but the orientation of the magnetic moments varies from one domain to another.

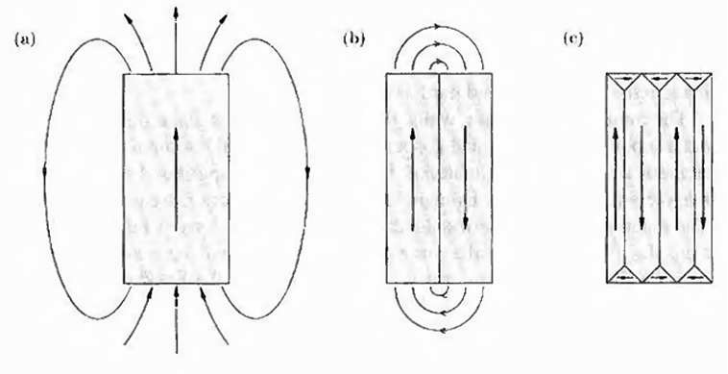

Figure 1.6: *Formation of magnetic domains. It is shown a gradual transition form a single domain configuration, uniformly magnetized (a) to a sample with two magnetic domains (b) to a multi-domain configuration, in which closure domains are present (c). The demagnetizing field is represented by the lines, and decreases as the number of domains increases [4].*

The interfaces separating these regions are called **domain walls**, typically classified in **Bloch walls** or **Néel walls** (Figure 1.7):

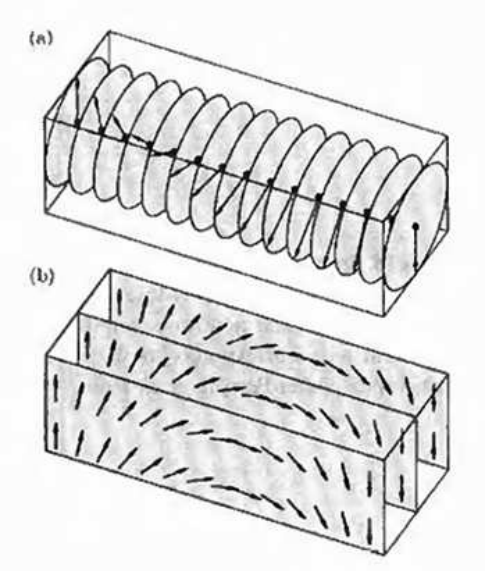

Figure 1.7: *(a) Bloch walls, characterized by spins rotating within a plane parallel to the domain wall, (b) Néel walls, characterized by spins rotating within a plane perpendicular to the domain wall [4].*

In a Bloch wall, the magnetization rotates within the plane of the wall and parallel to it. Conversely, in a Néel wall, the magnetization rotates in a plane perpendicular to the domain wall. When adjacent spins are required to rotate from one orientation to another, this process involves an energy cost.

As discussed previously, the Heisenberg Hamiltonian for a pair of spins in a ferromagnet gives an energy:

$$U = -2J\,\vec{S}_1 \cdot \vec{S}_2 = -2J\,S^2 \cos\theta. \tag{1.44}$$

Assuming that the angle θ between neighboring spins is small, a Taylor expansion of the latter relation leads to:

$$U \approx -2J\,S^2 + J\,S^2\,\theta^2, \tag{1.45}$$

The first term represents the exchange energy between parallel spins, whereas the second term corresponds to the additional energy arising from a small deviation from perfect alignment. The latter allows us to estimate the energy per unit area associated with the formation of a domain wall.

Considering a Bloch wall composed of N atomic layers over which the total angular rotation is π, the angle between each adjacent spins is given by $\theta = \frac{\pi}{N}$. The exchange energy per pair of neighboring spins can be written as:

$$U_{\mathrm{BW}} = J\,S^2\,\frac{\pi^2}{N^2}, \tag{1.46}$$

and therefore the total exchange energy across the wall becomes:

$$E_{\mathrm{ex}} = N\,U_{\mathrm{BW}} = J\,S^2\,\frac{\pi^2}{N} \tag{1.47}$$

This result suggests that increasing the number of atomic layers across the wall (*i.e.*, letting $N \to \infty$) reduces the energy per atom, implying that the domain wall tends to broaden throughout the material to minimize its total energy [4][1].

1.4.3 Magnetocrystalline anisotropy

This idealized model does not account for competing interactions that constrain the width of the domain wall. The most significant of these is the **magnetocrystalline anisotropy**, which arises from the preferred directions of magnetization dictated by the crystal structure [4][1]. This anisotropy direction distinguishes between:

- **easy axis**, along which magnetic moments preferentially align
- **hard axis**, along which alignment is energetically unfavorable

Some crystals may have multiple easy axes, but many ferromagnets exhibit **uniaxial anisotropy**, characterized by a single dominant easy direction for magnetization. For a uniaxial anisotropy ferromagnetic system, the energy density can be expanded as

$$E_{uniaxial} = K_0 + K_1 \sin^2\theta + K_2 \sin^4\theta + \cdots \approx K \sin^2\theta, \tag{1.48}$$

where K is the anisotropy constant (units of J/m^3), typically ranging from 10^2 to 10^7 J/m^3. This is often simplified to the first non-constant term, as higher-order contributions are typically negligible:

$$E_{uniaxial} = K sin^2(\theta) \tag{1.49}$$

1.4.4 Equilibrium domain wall width

An important consequence of anisotropy is its effect on the width of the domain walls. While increasing the wall thickness tends to reduce the exchange energy, anisotropy acts to confine the spins within energetically preferred directions, resulting in a compromise between these two competing energy terms. Near the boundary separating two adjacent domains, the spins gradually rotate from the orientation of one domain to that of the adjacent one, producing a local energy associated to the magnetic anisotropy. Assuming a Bloch wall and summing the contributions from N spins across the wall, the anisotropy energy density can be estimated as:

$$\sum_i^N K \sin^2\theta_i \simeq \frac{N}{\pi}\int_0^\pi K sin^2\theta d\theta = \frac{NK}{2} \tag{1.50}$$

This energy increases linearly with N, while the exchange energy (see Eq. 1.47) decreases inversely with N, meaning that the two contributions, for certain values of N, give regions in which one is dominant over the other. By considering the lattice spacing a of a ferromagnetic system, the total energy per unit area can be expressed as:

$$\sigma = J\,S^2\,\frac{\pi^2}{N\,a^2} + \frac{N\,K\,a}{2}, \tag{1.51}$$

Minimizing the latter relation with respect to N yields:

$$N = \pi\,S\sqrt{\frac{2J}{K\,a^3}} \tag{1.52}$$

i.e., the equilibrium number of spins across the wall, and, most importantly, to:

$$\delta = N\,a = \pi\,S\sqrt{\frac{2J}{K\,a}} \tag{1.53}$$

the **equilibrium width** of a domain wall. The wall width of a ferromagnet increases with the exchange constant J, meaning that the exchange interaction plays a huge role in the formation and maintenance of multi-domain configurations. In contrast, it decreases with K, the anisotropy constant related to the energy density of the system, and with a, the lattices spacing of the crystal [4].

1.5 Hysteresis Loop

As discussed in the previous section, the magnetic behavior offerromagnetic materials is strongly dependent on temperature. Specifically, the system behaves as a paramagnet for $T > T_c$ and as a ferromagnet for $T < T_c$. Moreover, in typical ferromagnetic materials, the magnetization curve exhibits hysteresis, a non-reversible path during the increase or decrease of the applied magnetic field, in contrast to the reversible Langevin response observed in paramagnets.
Let us consider a ferromagnet initially in a demagnetized state, with zero net magnetization and no external field. When an external field $\vec{H}$ is introduced, magnetization increases as the domain walls begin to move: the domains aligned with $\vec{H}$ grow at the expense of oppositely aligned domains, yielding a net magnetization. As $\vec{H}$ continues to rise, the magnetization approaches its saturation value $\vec{M}_s$. However, when the field is brought to zero, the material does not revert to a completely demagnetized state. Instead, it retains a residual magnetization $\vec{M}_r$, called remanence or residual field. To eliminate this remanence, the field must be driven in the opposite direction to a negative value H_c, known as the coercive field. Based on the magnitude of H_c, ferromagnets are classified as soft (low coercivity) or hard (high coercivity). The resulting closed loop, called **hysteresis loop** (Figure 1.8), illustrates the ability of ferromagnets to "remember" any previous magnetic stimuli, a property absent in paramagnets, as they do not retain any memory of prior magnetic perturbations [4].

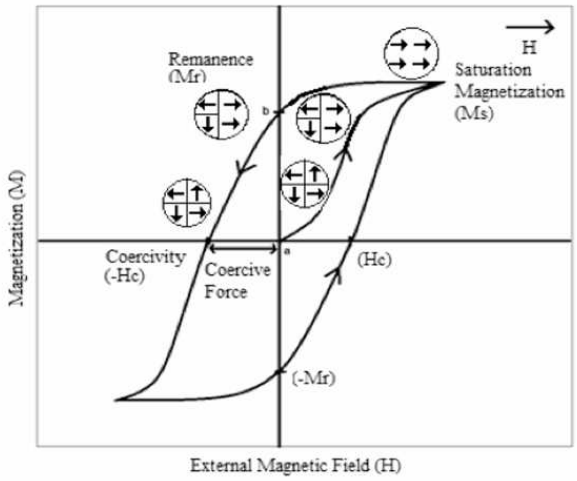

Figure 1.8: *Hysteresis loop of a ferromagnet. The system magnetization does not return to the initial state after interacting with an external field, requiring instead the application of another field to remove it [8]. The coercive field H_c, the residual magnetization M_r and the saturation magnetization M_S are highlighted.*

CHAPTER 2

NANOMAGNETISM

In the previous chapter, the fundamental properties of magnetism have been introduced, with a particular focus on the semi-classical interpretation and meaning of ferromagnetism.
However, when the size of a magnetic system is reduced to the nanometer scale, several assumptions of classical magnetism no longer hold, and new phenomena start to emerge.

This regime, known as **nanomagnetism**, requires a different theoretical and experimental approach to account for the influence of surface effects, finite-size scaling, and quantum mechanical interactions.

In this chapter, the basic concepts of nanomagnetism are presented and described, such as single-domain nanoparticles and superparamagnetism, two of the main topics whose implications find interesting applications in the biomedical field, *e.g.,* diagnostics and targeted drug delivery.

2.1 Single-domain nanoparticles

As discussed in Section 1.5, a ferromagnet is subject to various energy contributions, such as magnetocrystalline anisotropy and magnetostatic energy, which govern the formation of magnetic domains and the stabilization of the demagnetizing field [4]. Additionally, the creation of these domains requires a minimum crystal size to be energetically favorable.

As the crystal size decreases, the system must balance the energy cost between surface effects, which scale with the square of the sample size (*e.g.*, domain wall energy), and volume effects, such as demagnetizing energy, which scale with the cube of the sample size.

Below a certain diameter (typically less than 100 nm), the ferromagnet can no longer sustain more than one domain and instead opts to reach a single-domain configuration. In this regime, the system is referred to as a **single-domain magnetic particle**.

Assuming spherical symmetry, the critical radius below which an isolated particle adopts a single-domain configuration is given by:

$$r_{\text{critical}} \simeq \frac{36\sqrt{AK}}{\mu_0 M_s^2} \tag{2.1}$$

where [8]:

- A is the exchange stiffness constant, which quantifies the strength of spin alignment between neighboring atoms;
- K is the magnetocrystalline anisotropy constant;
- M_s is the saturation magnetization.

For example, in materials such as magnetite (Fe_3O_4) and maghemite (γ-Fe_2O_3), the critical diameter D_c is approximately 128 nm and 168 nm, respectively [3]. In Figure 2.1, a schematic representation of the stability regions of magnetic domains is provided.

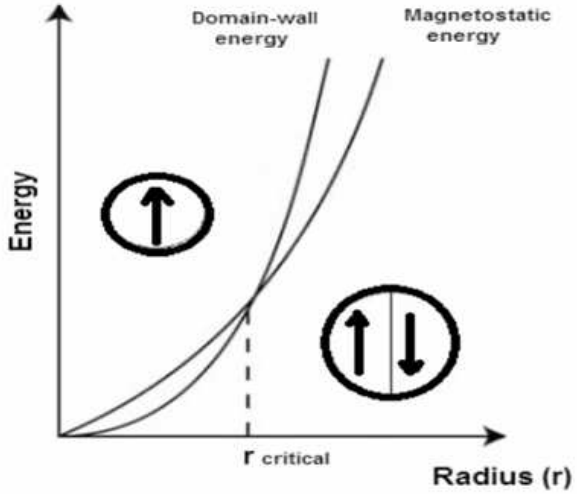

Figure 2.1: *Stability regions of magnetic domains. When the radius r of the particles exceeds the critical radius r_c, the system energetically prefers a multi-domain configurations; vice versa, when it is shorter than r_c it favors a single-domain one [8].*

In a single-domain configuration, all the spins are aligned in the same direction, resulting in a uniformly magnetized system characterized by a unique, large magnetic moment known as a **superspin**, which arises from the collective contribution of all atomic magnetic moments in the domain. Because no domain walls are present, the magnetization of the particle can rotate coherently with the superspin. As anticipated by the Stoner–Wohlfarth model, this behavior leads to higher coercivity, since rotating the entire magnetization requires more energy than simply moving domain walls.

2.2 Magnetic anisotropy

To introduce the key concept of superparamagnetism, it is necessary first to discuss one of the main principles governing the magnetic relaxation of these systems: **magnetic anisotropy** [4].

In Chapter 1, magnetocrystalline anisotropy was introduced as an energy contribution arising from the spin-orbit interaction between electrons, which tends to align the spins along specific crystallographic directions. However, when the system size decreases to the nanoscale and the particles are no longer considered isolated, additional contributions must be taken into account.

Consider a single-domain particle characterized by uniaxial anisotropy, meaning it has a preferential direction known as the **easy axis**. In the absence of any external magnetic field, the anisotropy energy can be expressed as:

$$E_A(\theta) = K_{\text{eff}} V \sin^2(\theta) \tag{2.2}$$

where:

- K_{eff} is the effective anisotropy constant, which includes contributions from bulk and surface anisotropy, representing the energy density per unit volume;
- V is the volume of the nanoparticle;
- θ is the angle between the magnetization direction and the easy axis.

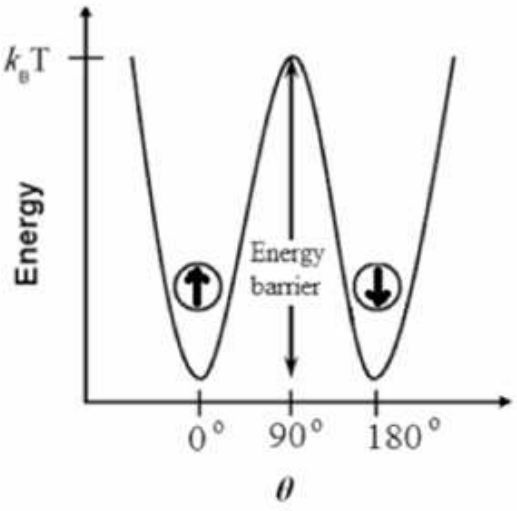

Figure 2.2: *Anisotropy energy as a function of the angle θ between the easy axis and the direction of magnetization in the absence of an external magnetic field [8].*

As shown in Figure 2.2, the function $E_A(\theta)$ has two minima at $\theta = 0$ and $\theta = \pi$, where $E_A = 0$, and one maximum at $\theta = \pi/2$, where $E_A = K_{\text{eff}} V$.

This implies that the magnetization has two energetically favorable orientations: one parallel and one antiparallel to the easy axis. To reverse the magnetization, the system must overcome an energy barrier of height $K_{\text{eff}}V$. The anisotropy energy depends on both the angle θ and the particle size: as the particle volume decreases, the energy required to overcome the anisotropy barrier becomes smaller.
Regarding the anisotropy constant K_{eff}, it is the result of different contributions that can be classified into two main categories: **bulk anisotropy** and **surface anisotropy**.

The total effective anisotropy is thus given by:

$$K_{\text{eff}} = K_B + \frac{5}{6}\frac{K_S}{d} \tag{2.3}$$

where d is the diameter of the particle, k_B is the bulk anisotropy constant, and K_S is the surface anisotropy constant.

2.2.1 Bulk anisotropy

Bulk anisotropy includes contributions arising from structure and crystal symmetry. It can be further subdivided as follows:

- **Magnetocrystalline anisotropy** (K_{MC}): already introduced, this arises from spin-orbit coupling and depends on the crystal lattice structure, but not on the particle shape.
- **Shape anisotropy** (K_F): caused by the demagnetizing field generated when an external magnetic field is applied and it depends on the geometry of the particles. For example, in an asymmetric particle characterized by a long and a short axis, the anisotropy is given by:

  $$K_F = \frac{1}{2}M_s^2(N_c - N_a) \tag{2.4}$$

  where N_c and N_a are the demagnetizing factors along the short (a) and long (c) axes, respectively. For spherical particles, $K_F = 0$ [9].
- **Exchange (or swap) anisotropy** (K_{swap}): this contribution arises from the contact or close interaction with another ferromagnetic material, which can induce new preferential directions for magnetization.
- **Stress anisotropy** (K_{stress}): induced by internal or external mechanical stresses acting on the crystal structure, potentially altering domain configurations or even triggering domain wall motion.

2.2.2 Surface anisotropy

Surface anisotropy accounts for energy contributions arising from broken symmetries at the nanoparticle surface. This causes a spin disorder at the particle boundaries that can lead to uncompensated surface spins, which in turn generate local magnetization and stray fields.

These local fields can significantly affect the orientation of the particle's overall magnetization, especially in systems with a high surface-to-volume ratio. The preferred magnetization direction may be altered by the anisotropy axis generated by these local surface fields.

The direction of the local field acting on a surface spin can be estimated by considering its nearest neighbors. For the i-th spin located at position $\vec{P}_i$, the net direction is given by:

$$\hat{n}_i \propto \sum_{j}^{N} (\vec{P}_i - \vec{P}_j) \tag{2.5}$$

where $\vec{P}_j$ are all the position vectors of the nearby interacting spins. Due to lattice disruptions at the surface, this vector $\hat{n}_i$ is generally non-zero and is oriented approximately orthogonal to the local surface, contributing to surface anisotropy [3].

2.3 Superparamagnetism

Although this topic is the last among the magnetic behaviors discussed in this chapter, it plays a fundamental role in current research, as it directly affects measurable properties such as saturation magnetization, magnetic relaxivity for MRI contrast agents, and the dynamic response to static or alternating magnetic fields.

Superparamagnetism emerges in ferromagnetic nanoparticles whose size is below a critical diameter, typically under 50 nm, such that the particles remain in a single-domain configuration, as discussed at the beginning of Chapter 2 [8].

For a system of non-interacting nanoparticles with sufficiently small diameters and volume V, the anisotropy energy can be described by Equation (2.2). The superspin of the nanoparticle can point either "up" ($\theta = 0$) or "down" ($\theta = \pi$), and a reversal of magnetization requires overcoming an energy barrier equal to KV [4].

When the thermal energy $k_B T$, with k_B being the Boltzmann constant (1.38×10^{-23} J/K) and T the absolute temperature, becomes comparable to or greater than the anisotropy energy barrier, *i.e.*, $k_B T \geq KV$, the system is no longer energetically constrained to maintain a fixed magnetization direction. As a result, the giant spin can spontaneously flip even in the absence of an external magnetic field due to thermal fluctuations, meaning that increasing the temperature of the system further raises the frequency of these fluctuations.

This behavior, known as **superparamagnetism**, is analogous to paramagnetism but with a

fundamental difference: the fluctuating magnetic moments are the ”giant spins” of the entire nanoparticles, yielding a much stronger magnetic response, hence the prefix “super.” These rapid fluctuations, when averaged over time, result in a zero net magnetization, and the particle exhibits no magnetism unless perturbed by an external magnetic field.

2.3.1 Néel relaxation and Vogel-Fulcher law

The time required for a nanoparticle's superspin to reverse its direction is described by the **Néel-Arrhenius law**, valid for non-interacting superparamagnetic particles with uniaxial anisotropy:

$$\tau_N = \tau_0 \exp\left(\frac{\Delta E}{k_B T}\right) \tag{2.6}$$

where:

- τ_N is the characteristic Néel relaxation time;
- τ_0 is the attempt time (typically around 10^{-9} s), which depends on parameters such as the gyromagnetic ratio and temperature;
- $\Delta E = KV$ is the anisotropy energy barrier in the absence of an external field.

Otherwise, in the case of interacting particles, the relaxation process becomes more complex due to the interactions between those superspins. As discussed in Chapter 1, the main interactions that affect a system of interacting magnetic moments are:

- **Dipolar interactions**, long-range interactions between two or more magnetic moments, here representing the giant spins of the nanoparticles, that become negligible if they are sufficiently distant;
- **Exchange interactions**, short-range forces between surface spins of adjacent particles, that tend to align them in an ordered configuration.

These interactions dynamically modify the energy landscape, leading to a distribution of energy barriers instead of a single fixed barrier. Consequently, the magnetization relaxation involves additional energy contributions, which reflect the collective magnetic behavior of the system.

To account for these effects, the Néel-Arrhenius law is extended to include an effective temperature parameter T_0, resulting in the **Vogel-Fulcher law**:

$$\tau_{VF} = \tau_0 \exp\left(\frac{E_{\text{barrier}}}{k_B (T - T_0)}\right) \tag{2.7}$$

Here, T_0, known as the **effective temperature**, serves as an empirical parameter that quantifies the strength of interparticle magnetic interactions by shifting the temperature dependence of the relaxation time [10].

2.3.2 Brownian relaxation

An alternative mechanism for superspin reversal is the **Brownian relaxation**, which occurs when the magnetic moment is rigidly coupled to the crystal lattice and the entire particle physically rotates in a medium. In this scenario, rather than an internal spin flip, the particle reorients its magnetization axis through Brownian motion [8].
The characteristic relaxation time associated with this process is given by:

$$\tau_B = \frac{3\eta V_H}{k_B T} \tag{2.8}$$

where:

- τ_B is the Brownian relaxation time;
- η is the dynamic viscosity of the surrounding fluid;
- V_H is the hydrodynamic volume of the particle, including coatings or surfactants of the nanoparticle;
- T is the temperature, and k_B the Boltzmann constant.

When both the Néel and Brownian relaxation processes are active, the overall relaxation time τ_{eff} is given by the sum of the inverses of the individual relaxation times:

$$\frac{1}{\tau_{\text{eff}}} = \frac{1}{\tau_N} + \frac{1}{\tau_B} \quad \Rightarrow \quad \tau_{\text{eff}} = \frac{\tau_B \cdot \tau_N}{\tau_N + \tau_B} \tag{2.9}$$

Observing Equations (2.6) and (2.8), it is evident that both characteristic times depend on the particle volume V: the Néel relaxation time τ_N increases exponentially with V, while the Brownian relaxation time τ_B increases linearly with it.
Because of this, τ_N dominates the effective relaxation time in Equation (2.9) for smaller particles, whereas τ_B becomes increasingly significant as the particle diameter increases. In Figure 2.3, the relaxation times as a function of the radius of the particles are shown.

Therefore, it is possible to define a specific diameter at which $\tau_N = \tau_B$, known as the **Shliomis diameter**:

$$D_S = \left(\frac{24 k_B T}{\pi K}\right)^{1/3} \tag{2.10}$$

For diameters $D > D_S$, Néel relaxation is no longer dominant and Brownian relaxation becomes the prevailing mechanism [9].

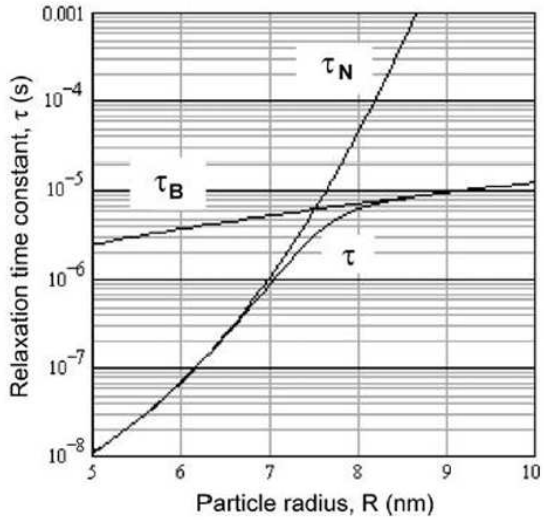

Figure 2.3: *Characteristic times of Brownian, Néel, and effective relaxation as a function of particle radius [11].*

2.3.3 Blocking temperature and measurement time

The temperature of the system critically influences the relaxation time and, consequently, the magnetic behavior of the nanoparticles. The transition from a superparamagnetic state to a blocked state, in which thermal energy is insufficient to overcome the anisotropy barrier and the superspin is blocked along the easy direction, occurs at the **blocking temperature** T_B. However, determining T_B is not absolute; it depends on the measurement timescale, referred to as τ_m, the characteristic measurement time [7].
Three regimes can then be distinguished:

- $\tau_m \ll \tau_N$: the time of measurement is too short to observe magnetization reversal, and the particle appears magnetically blocked;
- $\tau_m \gg \tau_N$: the particle exhibits superparamagnetic behavior as multiple spin flips occur during the measurement. The mean total magnetization reverses so rapidly that, when the external field is null, it is zero;
- $\tau_m = \tau_N$: this is the optimal condition for the measurement to define the blocking temperature, yielding the expression:

$$T_B = \frac{KV}{k_B \ln\left(\frac{\tau_m}{\tau_0}\right)} \tag{2.11}$$

Typically, measurement times are on the order of 100 seconds, which implies that $\ln\left(\frac{\tau_m}{\tau_0}\right) \approx 25$ (assuming $\tau_0 \approx 10^{-9}$ s). This leads to two important estimations:

The critical energy barrier for thermal blocking is given by:

$$\Delta E_{\text{critical}} = 25\, k_B T \tag{2.12}$$

which corresponds to the critical volume above which superparamagnetic behavior is no longer observed [8]:

$$V_{\text{critical}} = \frac{25\, k_B T}{K} \tag{2.13}$$

2.4 Stoner-Wohlfarth Theory

The Stoner-Wohlfarth theory describes how the anisotropy energy barrier of a single-domain magnetic nanoparticle is modified in the presence of an external magnetic field [9].

The model considers a spherical, single-domain particle with uniaxial anisotropy subjected to an external field $\vec{H}$. The total magnetic energy of the system is described by the following expression:

$$E(\alpha, \theta) = KV \sin^2(\theta) - \mu_0 M_s V H \cos(\alpha - \theta) \tag{2.14}$$

where:

- α is the angle between the particle's easy axis and the external field $\vec{H}$;
- θ is the angle between the easy axis and the magnetization vector $\vec{M}$;
- K is the uniaxial anisotropy constant;
- M_s is the saturation magnetization.

Unlike the case with no external field, the energy landscape described by Equation (2.2) is no longer symmetric with respect to $\theta = 0$ and $\theta = \pi$. The applied field shifts the positions of the energy minima and modifies the energy barrier ΔE, which is no longer equal to KV.

To determine the equilibrium positions, the energy is minimized by setting its derivative with respect to θ equal to zero:

$$\frac{dE}{d\theta} = 2KV \sin\theta \cos\theta - \mu_0 M_s V H \sin(\alpha - \theta) = 0 \tag{2.15}$$

In the case of a perpendicular field ($\alpha = \pi/2$), the equation simplifies to:

$$2K \sin\theta \cos\theta = \mu_0 M_s H \cos\theta \tag{2.16}$$

From this, we define the **anisotropy field** H_K as the external field strength required to rotate the

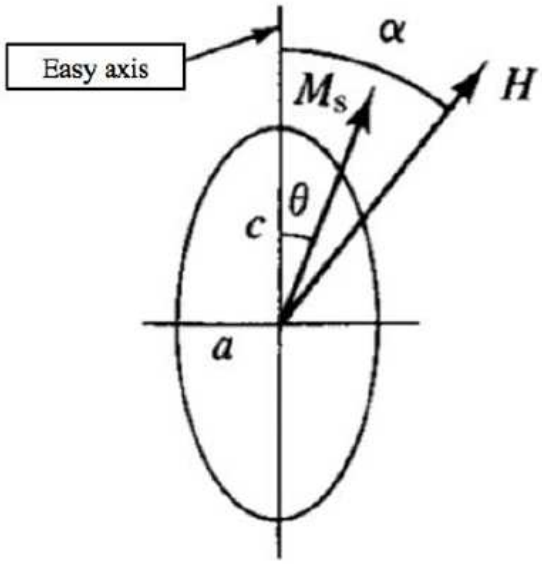

Figure 2.4: *Stoner-Wohlfarth model: representation of a spheroidal nanoparticle with magnetization vector tilted by an angle θ with respect to the easy axis, in the presence of an external field* **H** *forming an angle α with the easy axis [9].*

magnetization to $\theta = \pi/2$:

$$H_K = \frac{2K}{\mu_0 M_s} \tag{2.17}$$

If, instead, the field is applied antiparallel to the easy axis ($\alpha = \pi$), the energy derivative becomes:

$$\frac{dE}{d\theta} = 2KV \sin\theta \cos\theta - \mu_0 M_s V H \sin\theta \tag{2.18}$$

which can be rewritten as:

$$\frac{dE}{d\theta} = \sin\theta(2KV \cos\theta - \mu_0 M_s V H) \tag{2.19}$$

This expression has two extrema at $\theta = 0$ and $\theta = \pi$, corresponding to local minima of the energy. Specifically:

$$E(\alpha = \pi, \theta = 0) = +\mu_0 M_s V H \tag{2.20}$$

$$E(\alpha = \pi, \theta = \pi) = -\mu_0 M_s V H \tag{2.21}$$

indicating that $\theta = \pi$ is the global minimum.

To find the energy maximum (the barrier height), we consider the critical angle θ such that:

$$\cos\theta = \frac{\mu_0 M_s H}{2K} \tag{2.22}$$

Substituting into Equation (2.14), we obtain the maximum energy:

$$E_{\max} = KV\left(1 - \cos^2\theta\right) + \mu_0 M_s V H \cos\theta = KV\left(1 + \frac{\mu_0^2 M_s^2 H^2}{4K^2}\right) \tag{2.23}$$

Thus, the energy barrier is:

$$\Delta E = E_{\max} - E_{\min} \tag{2.24}$$

$$= KV\left(1 + \frac{\mu_0^2 M_s^2 H^2}{4K^2} - \frac{\mu_0 M_s H}{K}\right) \tag{2.25}$$

$$= KV\left(1 - \frac{H}{H_K}\right)^2 \tag{2.26}$$

This last expression shows how the energy barrier decreases with increasing field strength and vanishes when $H = H_K$. However, it is only valid for $\alpha = \pi$. For arbitrary angles α, the barrier can be generalized as:

$$E_B = E_{B,0}\left(1 - \frac{H}{H_{sw}^0}\right)^{\epsilon} \tag{2.27}$$

where:

- $E_{B,0}$ is the zero-field anisotropy energy barrier $K_{eff}V$;
- H_{sw}^0 is the **zero-temperature switching field**, *i.e.*, the field required to reverse the magnetization at $T \approx 0$ K;
- ϵ is an exponent that depends on the angle α: for $\alpha = \pi$, $\epsilon = 2$; for intermediate angles, a typical value is $\epsilon = 1.5$ [9][12][10].

2.5 Hysteresis loop in magnetic nanoparticles

An important aspect of magnetic nanoparticles is how their hysteresis behavior changes as a function of particle size, particularly in single-domain regimes.

As shown in Figure 2.5, the coercive field H_c, the external field required to reduce the net magnetization of a ferromagnet to zero, strongly depends on the particle diameter D.

The behavior can be qualitatively divided into three regimes:

- $D > D_c$: for large diameters, the system adopts a multi-domain configuration to minimize its total energy. In this regime, H_c increases as D decreases, due to the reduced mobility of domain walls, whose motion becomes energetically more costly.

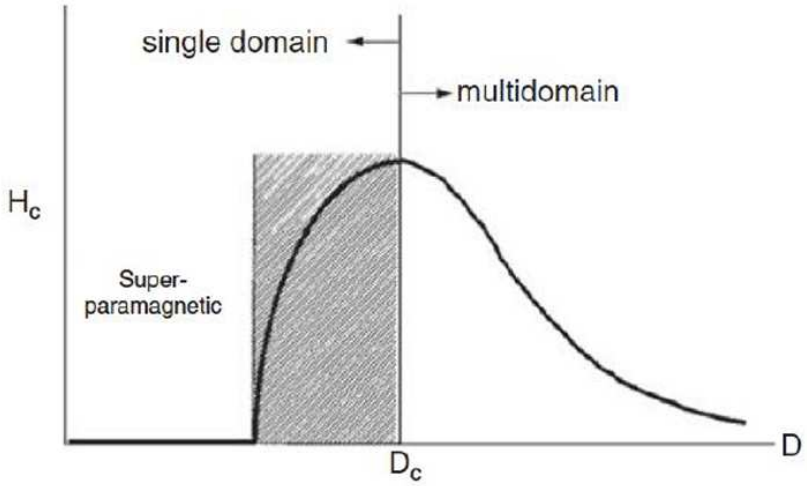

Figure 2.5: *Coercive field H_c as a function of the nanoparticle diameter D[10].*

- $D \sim D_c$: around the critical diameter D_c, the particle assumes a single-domain configuration. The coercive field reaches a maximum, and the corresponding hysteresis loop is the largest possible for the material.
- $D < D_c$: as the diameter decreases further, the system enters the superparamagnetic regime. Thermal fluctuations dominate, leading to a rapid drop in coercivity. In this case, the hysteresis loop collapses, and the magnetization-field response becomes sigmoidal, similar to that described by the Langevin function for paramagnets.

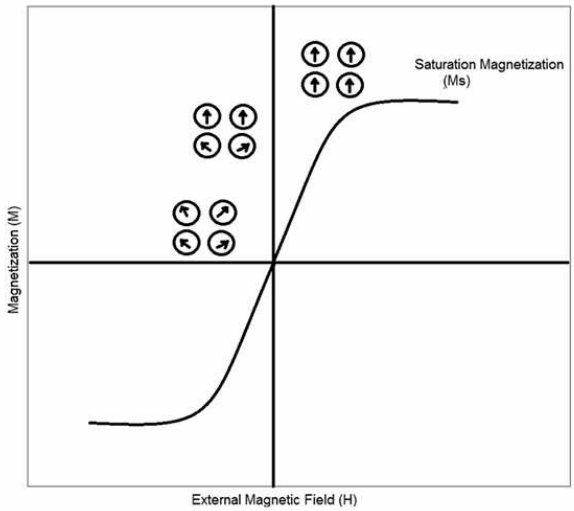

Figure 2.6: *Hysteresis loop of a superparamagnetic nanoparticle [8].*

In the superparamagnetic regime, the system exhibits a magnetization curve without hysteresis: the magnetization can spontaneously reverse its direction due to thermal energy, and there is no remanent magnetization once the external field is removed [13].

The dependence of the coercive field on the particle diameter can be approximated by the following empirical expression:

$$H_c(D) = H_{\max} \cdot \left(\frac{D}{D_c}\right)^{-0.6} \cdot \left[1 - \exp\left(-\left(\frac{D}{D_c}\right)^5\right)\right] \tag{2.28}$$

where:

- $H_{\max}$ is the maximum coercive field, reached at $D \approx D_c$;
- D_c is the critical diameter marking the transition to the superparamagnetic regime.

For very small diameters ($D \ll D_c$), the exponential term dominates, leading to negligible coercivity. As the diameter approaches D_c, the coercivity increases, reaching a peak. For larger diameters ($D \gg D_c$), the formation of multiple domains reduces coercivity approximately according to a power law: $H_c \propto D^{-0.6}$. This non-monotonic behavior of H_c is a key characteristic of ferromagnetic nanoparticles and reflects the interplay between thermal activation, magnetic anisotropy, and domain structure [14].

Chapter 3

NMR Relaxometry

This chapter provides the theoretical foundations of the **Nuclear Magnetic Resonance** (NMR) technique and NMR **relaxometry**. It introduces the methods used to measure nuclear relaxation times T_1 and T_2, as well as the principal theoretical models that describe the relaxivity of magnetic nanoparticles (MNPs), allowing the evaluation of their morphological and chemico-physical characteristics, for example, through the Roch-Müller-Gillis model.

Unlike conventional NMR spectroscopy, which primarily focuses on spectral resolution and molecular identification, relaxometry is used to study the spin dynamics of the investigated systems in a wide range of frequencies, *i.e.*, static magnetic fields.
Following concepts lay the groundwork for the experimental results and interpretations presented in the upcoming sections of the thesis.

3.1 Nuclear Magnetic Resonance principles and pulse sequences

The **nuclear magnetic resonance** (NMR) is a spectroscopic technique used to probe the dynamic interactions of nuclear spins with their microscopic environment[15].
Atomic nuclei possess a magnetic moment μ_I when they have non-zero nuclear spin momentum, through the relation:

$$\vec{\mu_I} = \gamma_I \hbar \vec{I} \tag{3.1}$$

where $\hbar$ is the reduced Planck constant equal to 1.054×10^{-34}Js and γ the gyromagnetic ratio, a parameter that characterize each atom.

To perform an NMR experiment, a nucleus with non-zero spin is needed and different elements

in nature can be exploited for this aim, such as ^{1}H and ^{13}C; the human body, for instance, is overall made by 70% of water and hydrogen protons constitute a huge source to generate an appreciable NMR signal.

Two different approaches can be discussed to introduce how the technique works at the atomic level: a classical description, which mathematically and physically considers the spin (a quantum-mechanics quantity) as an angular moment under the action of an external magnetic field, and a quantum description that exploits the perturbative theory.

3.1.1 Classical and quantum approach of NMR

Physical systems subject to any kind of perturbation evolve towards the configuration with the minimum energy given by the energetic balance between the different interactions that influence them. In the case of a magnetic moment under the action of an external magnetic field, two different approaches can be used to describe the time evolution of it: a classical and a quantum model.

In the **classical approach**, considering a region of space in the laboratory frame of reference Σ_{lab}, an isolated magnetic moment, under the influence of an external magnetic field $\vec{H}_0 = H_0\hat{z}$, is subject to a torque $\vec{\tau}$:

$$\vec{\tau} = \vec{\mu}_I \times \vec{H}_0 \tag{3.2}$$

which causes the magnetic moment to align along the field direction and to precess around it at an angle θ due to the conservation law of angular momentum:

$$\frac{d\vec{\mu}}{dt} = \gamma_I \vec{\mu}_I \times \vec{H}_0 \tag{3.3}$$

as it is illustrated in Figure 3.1. The frequency at which the moment is precessing is called **Larmor frequency** and is related to the static external magnetic field through the relation:

$$\omega_L = -\gamma_I H_0 \tag{3.4}$$

where the minus sign indicates a clockwise rotation of the moment motion.
Extending the same reasoning for a multiplicity of non-interacting magnetic moments, such that we can consider the magnetization $\vec{M}$ instead, the time evolution can be re-written as:

$$\frac{d\vec{M}}{dt} = \gamma_I \vec{M} \times \vec{H}_0 \tag{3.5}$$

The system precesses around the direction of the static magnetic field at the Larmor frequency ω_0 [16].

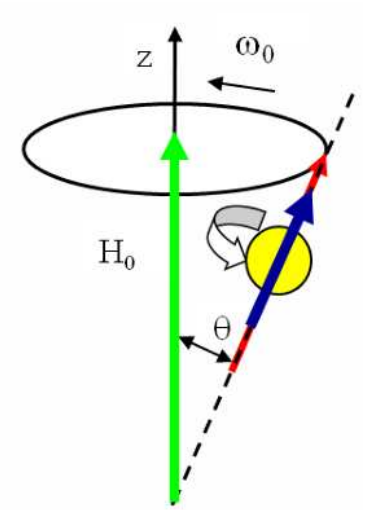

Figure 3.1: *Representation of the precession motion of a magnetic moment around an external magnetic field $\vec{H}_0$ with an angular frequency ω_0. The field and moment directions form an angle θ (which remains constant in time) and the rotation of the system is clockwise oriented.*

A second oscillating magnetic field H_1 is applied:

$$\vec{H}_1(t) = H_1[cos(\omega_{rf}t)\hat{x} + sin(\omega_{rf}t)\hat{y}] \tag{3.6}$$

It is assumed to be much smaller than $\vec{H}_0$ in magnitude, and it can be considered as a radio-frequency field composed of two circularly polarized components, both with amplitude $\vec{H}_1$ but opposite rotating directions (respectively, one clockwise and one counter-clockwise), placed in a perpendicular direction with respect to the first static magnetic field. This perturbation leads to a variation of the precession angle θ, as the system starts to precess around $\vec{H}_1$ once it is displaced from equilibrium.
Adding this new contribution to Equation (3.5), it now becomes:

$$\frac{d\vec{M}}{dt} = \gamma_I \vec{M} \times (\vec{H}_0 + \vec{H}_1) \tag{3.7}$$

The H_1 effect is maximized when it oscillates in resonance with the system, *i.e.*, when it rotates together with the magnetization itself, and so when $\omega_L = \omega_{rf}$.

To properly work under resonance condition, the system is studied from a second non-inertial frame of reference, called **rotating frame** Σ_{rot}, described by the vector triad $(\hat{x}', \hat{y}', \hat{z}')$ such that $\hat{z}' = \hat{z}$.
By applying the transformation laws for relative systems, the magnetization in the rotating frame can be written as:

$$(\frac{d\vec{M}}{dt})' = (\frac{d\vec{M}}{dt}) - \vec{\Omega} \times \vec{M} \tag{3.8}$$

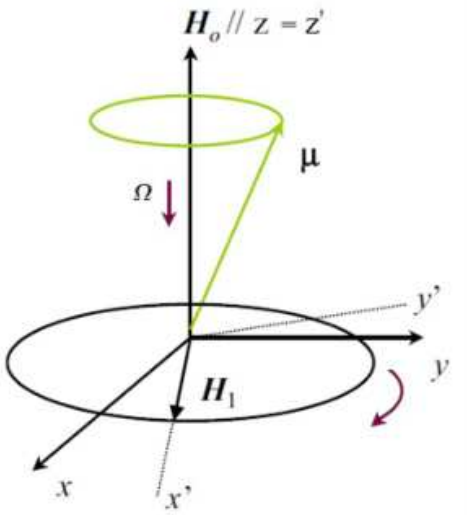

Figure 3.2: *Rotating* $(\hat{x}', \hat{y}', \hat{z}')$ *and laboratory* $(\hat{x}, \hat{y}, \hat{z})$ *frame visualization of the system. After the rf pulse, the magnetization is tilted in* x'-y' *plane and rotates counterclockwise around* H_1 *[17].*

with $\vec{\Omega} = \omega_{rf}\hat{z}'$ the vector angular frequency of the rotating frame.
Since H_1 is fixed in the x'-y' plane, the total magnetic field in Equation (3.7) can be expressed as a function of an effective magnetic field H_{eff}:

$$\vec{H}_{eff} = \gamma_I(H_0 + \frac{\omega_{rf}}{\gamma_I})\hat{z}' + H_1\hat{x}' \tag{3.9}$$

so that:

$$(\frac{d\vec{M}}{dt})' = \gamma_I\vec{M} \times \vec{H_{eff}} = \vec{M} \times [(-\omega_L + \omega_{rf})\hat{z}' - \omega_1\hat{x}'] \tag{3.10}$$

where $\omega_1 = -\gamma_I H_1$ is the angular frequency at which the magnetic moment is rotating around H_1.
From the previous equation, by choosing $\omega_L = \omega_{rf}$, the effect of the field along the $\hat{z}'$ direction is canceled, meaning that the magnetization feels only $\vec{H}_1$ and the resonance condition is completely achieved.

The applied oscillating magnetic field generates a rotation of the magnetization, reversing it onto the x'-y' plane by an angle $\Delta\theta = \gamma_I H_1 \tau_{rf}$, where τ_{rf} is the duration of the radio-frequency field, typically very short as it is of the order of milliseconds.
It is possible to flip the magnetization with different angles based on the relaxometric effect we want to study. The most used flipping angles in NMR experiments (applied perpendicularly to the $\hat{z}'$ axis) are:

- $\pi/2$ **pulse**, which consists of a 90 degree flip of the magnetization into the x'-y' plane so that the resulting magnetization has a null longitudinal component M_z;

- π **pulse**, which consists of a 180 degree flip instead, causing the magnetization to go from (+$\hat{z}'$) into (-$\hat{z}'$), meaning that a complete reversal of its orientation along the longitudinal axis is performed.

A representation of these pulses is shown in Figure 3.3.

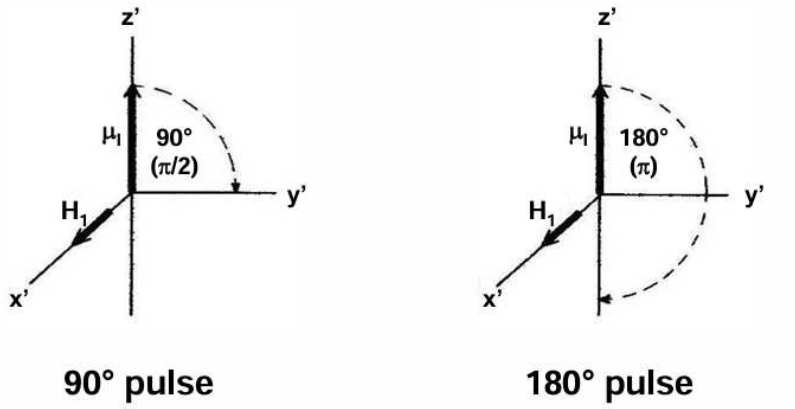

Figure 3.3: *$\pi/2$ and π flip angles visualization. The pulses are applied perpendicularly to the z-axis. The $\pi/2$ pulse flips the magnetization in the $(x^{'}, y^{'})$ plane and completely removes the longitudinal component of the magnetization; the second pulse, instead, completely inverts the magnetization into the $\hat{z}'$ axis of the rotating frame of the system.*

With the **quantum approach**, assuming an ensemble of N non-interacting spins in a volume V, each spin is characterized by a thermal energy contribution, which randomly distributes the spins along any direction, and a magnetic energy contribution, described by the Zeeman energy relation $U = -\vec{\mu_I} \cdot \vec{H}_0$, which aligns spins parallel to $\vec{H}_0$.

Each magnetic moment possesses a spin degeneracy due to the possible available values of the quantized angular momentum: $\mu_I = \gamma_I \hbar m_z$, with m_z assuming $\pm 1/2$ based on the direction of the spin along $\hat{z}$.
At thermal equilibrium, the application of an external field $\vec{H}_0$ causes the splitting of the degeneracy into two energetically distinct levels, called the splitting Zeeman, with $U = -\vec{\mu_I} \cdot \vec{H}_0$ = - $\hbar$ ω m_z H_0:

- $E_{\uparrow}(m = 1/2) = -\frac{\hbar \gamma_I H_0}{2}$
- $E_{\downarrow}(m = -1/2) = +\frac{\hbar \gamma_I H_0}{2}$

with a total energy separation of $\Delta E = \hbar \gamma_I H_0 = \hbar \omega_L$, where ω_L is the already cited Larmor frequency.

Temperature plays an important role in the population density of the two energy states ”up” or ”down”: the respective probability of having one of the configurations is described, respectively,

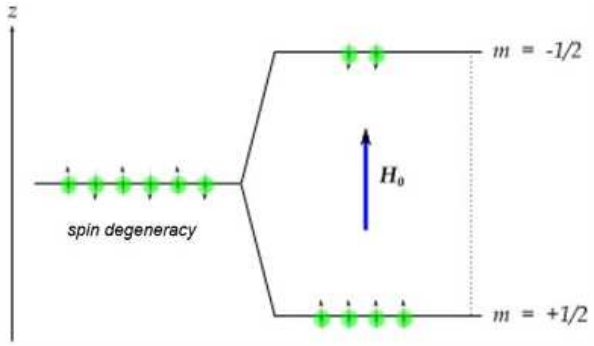

Figure 3.4: *Zeeman energy splitting due to the external static field $\vec{H}_0$. The energy levels for a single magnetic moment are split into two different levels, separated by an energy shift of $\hbar\omega$.*

by the following two relations from the Boltzmann statistics:

$$P_\uparrow = \frac{\exp\left(-\frac{E_\uparrow}{k_B T}\right)}{\exp\left(-\frac{E_\uparrow}{k_B T}\right) + \exp\left(-\frac{E_\downarrow}{k_B T}\right)} \tag{3.11}$$

$$P_\downarrow = \frac{\exp\left(-\frac{E_\downarrow}{k_B T}\right)}{\exp\left(-\frac{E_\uparrow}{k_B T}\right) + \exp\left(-\frac{E_\downarrow}{k_B T}\right)} \tag{3.12}$$

where k_B is the Boltzmann constant already cited in Chapter 2 and T is the temperature of the lattice.
The $|\uparrow\rangle$ state has, statistically, a higher probability than $|\downarrow\rangle$, which makes it more populated by the spins.
The total magnetization that is generated by the field influence can be derived using statistical mechanics:

$$\vec{M}_0 = \frac{N}{V}\langle(\vec{\mu}_i)_z\rangle = \frac{N}{V}\sum_i P(m_i)\hbar\gamma_I m_i \tag{3.13}$$

which gives, for an ideal paramagnet:

$$M_0 = \frac{N_\uparrow - N_\downarrow}{V}\mu_I = \frac{N}{V}\mu_I \tanh(x) \tag{3.14}$$

with $x = \frac{\mu_I H_0}{k_B T}$. As we can see, the result can be brought back to the limit case of $J = 1/2$ of the Brillouin function, for which the curve becomes a hyperbolic tangent.

3.1.2 Bloch equations and relaxation times

After applying the first static field $\vec{H}_0$, the magnetization of the system precesses around the field direction and can be decoupled into two components: a perpendicular (transverse) component

$\vec{M}_{xy}$ (with module $\sqrt{M_x^2 + M_y^2}$) and a parallel (longitudinal) one $\vec{M}_z$.

The transverse component has an expected value of zero, since each projection of the transverse magnetization cancels out over a period, while the longitudinal component is exactly equal to M_0. Once the rf pulse generated by $\vec{H}_1$ is terminated, the spin system is left in an out-of-equilibrium state and starts to precess back around $\vec{H}_0$ to its original condition. For this reason, each spin interacts with the surrounding magnetic moments and with the lattice around by exchanging energy, in order to recover the original magnetization that was modified by the perturbation.

The time required to return to equilibrium is therefore characterized by two time constants: T_1, also known as **spin-lattice relaxation time**, which describes the time required by the spins to recover the magnetization $\vec{M}_z$ that was tilted and put in the transverse plane by exchanging energy with the surrounding environment to go back to equilibrium. T_2, called **spin-spin relaxation time**, instead describes the decaying of $\vec{M}_{xy}$ due to the local magnetic fields created by the neighboring spins and the possible inhomogeneities of $\vec{H}_0$, changing the precession motion of the spins by affecting their ω_L. In fact, such perturbations spread the resonance frequency into a distribution of frequencies felt by the spins, causing them to dephase and rotate with different angular velocities. By comparing the two time parameters, T_1 is approximately two orders of magnitude larger than T_2 [16].

Considering, for instance, a $\pi/2$ pulse perturbation sent to the system in the $\hat{x'}$ direction, the magnetization $\vec{M}$ is now reversed in the transverse plane x'-y' and the relaxation equations, named **Bloch Equations**, in the rotating frame Σ_{rot} are described by:

$$M_z = M_0(1 - e^{-\frac{t}{T_1}}) \tag{3.15}$$

and

$$M_{xy} = M_0 e^{-\frac{t}{T_2}} \tag{3.16}$$

At $t = 0$, which refers to the moment after which $\vec{H}_1$ is removed, the magnetization is completely reversed in the transverse plane and starts to recover by evolving the values of the two components over time. From Figure 3.5, the behavior of the two curves shows that M_z, the longitudinal component, returns to M_0, while M_{xy}, the transverse one, slowly decays to zero according to their time parameters T_1 and T_2, respectively.

Possible inhomogeneities of the static magnetic field affect the resulting T_2 as they rapidly dephase the spins. The relaxation induced is then faster and can be rewritten as:

$$\frac{1}{T_2^*} = \frac{1}{T_2} + \frac{1}{T_2'} \tag{3.17}$$

where $1/T_2'$ describes the inhomogeneity component and $1/T_2^*$ is the transversal relaxation rate of the system affected by field inhomogeneities. It is possible to minimize the effect of T_2^* by

applying precise pulse sequences (see CPMG or Spin-Echo sequences in the following sections), thus allowing for a more accurate determination of T_2.

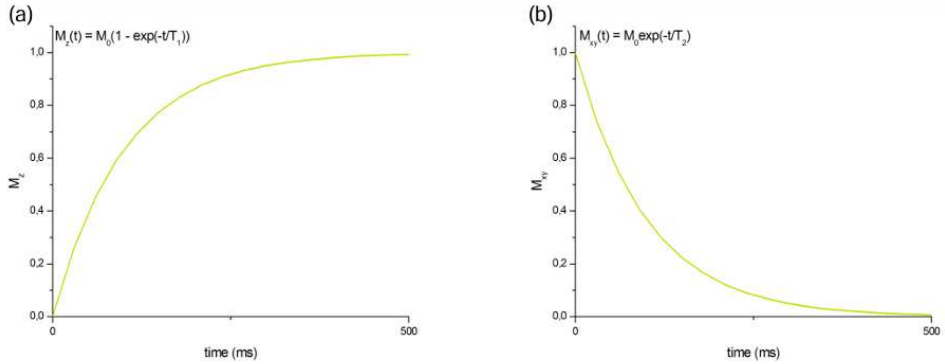

Figure 3.5: *Bloch equations representation in the rotating frame of the system after a $\pi/2$ pulse. Figure (a) shows the longitudinal recovery of the magnetization $M_z(t)$, dictated by T_1, while Figure (b) describes the transverse magnetization $M_{xy}(t)$ fading after the $\pi/2$ pulse, according to T_2 instead.*

The semi-classical equations that describe the total magnetization motion in time can be collected into a unique Bloch Equation:

$$\frac{d\vec{M}}{dt} = \gamma_I \vec{M} \times \vec{H}_0 + \frac{1}{T_1}(M_0 - M_z)\hat{z} - \frac{1}{T_2}\vec{M}_{xy} \tag{3.18}$$

3.1.3 NMR signal and sequences

To produce a signal, two magnetic fields are required: $\vec{H}_0$, a static magnetic field that determines the Larmor frequency at which the magnetization, and so the spins, are precessing around, and $\vec{H}_1$, an oscillating magnetic field, sent to tilt the magnetization out of its equilibrium state and generate a signal from its relaxation. In Figure 3.6 is represented the configuration of the RF coil containing the sample along with the static and oscillating magnetic field.

The radio-frequency field is produced by sending an alternating current through the coil where the sample is inserted. When the perturbing pulse ends, the magnetization M_{xy} changes over time by returning to zero, and this causes the induction of an electromotive force EMF due to the variation of the magnetic flux over the coil itself, as explained by the Faraday-Neumann-Lenz law:

$$S(t) = EMF = -\frac{d\Phi_M}{dt} \tag{3.19}$$

where Φ_M is the magnetic flux through the coil.
The generated signal is called **free induction decay** or FID, and its intensity is proportional to

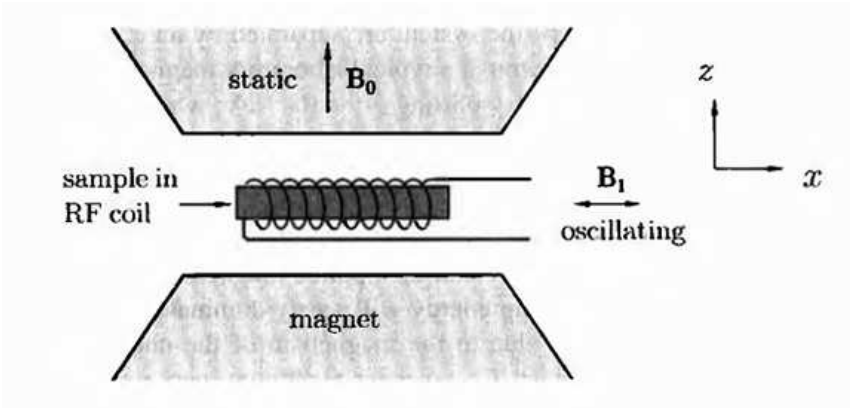

Figure 3.6: *NMR setup configuration of coil, sample and magnetic fields applied.* $\vec{B}_0$=$\vec{H}_0$ *is often referred as the static magnetic field, oriented along the* $\hat{z}$*-direction, while* $\vec{B}_1$=$\vec{H}_1$ *is the oscillating magnetic field, directed in the x or y axis according to the coil direction.*

the transverse magnetization and the magnetic field induced inside the coil:

$$S(t) = -\frac{d}{dt}\int_V \vec{M}_{xy}(\vec{r},t)\cdot\vec{B_{rec}}(\vec{r})d^3\vec{r} \tag{3.20}$$

where V is the sample volume under investigation and $\vec{B_{rec}}$ is the magnetic field per unit current produced at the position $\vec{r}$ inside the coil. The FID is then detected by the same coil, operating in a dual transmission-receiver modality, and processed by the NMR spectrometer, which is discussed in depth in Chapter 5 of this work as part of the instrumentation used for the experimental part.

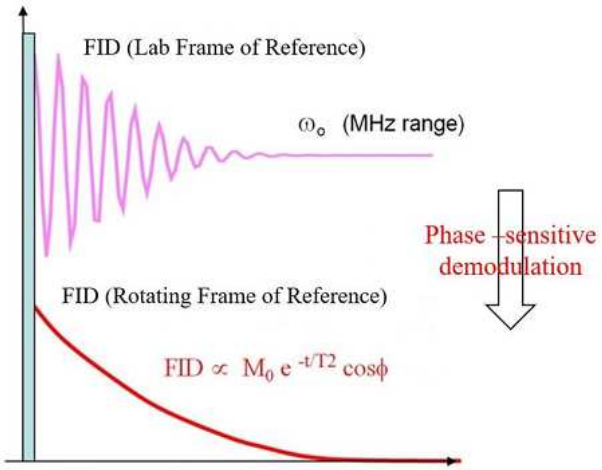

Figure 3.7: *FID signal in laboratory and rotating frame representation. In the Lab frame, the signal appears as an oscillating, fading signal dictated by the transverse magnetization* $\vec{M}_{xy}$*. In the rotating frame, after a phase demodulation which allows to digitize the received signal by removing any oscillating contribution, the signal appears as a decaying curve dependent on* M_0 *and* T_2*.*

The resulting signal after demodulation has the form:

$$FID(t) \sim M_0 e^{\frac{-t}{T_2}} cos(\phi) \tag{3.21}$$

which is a decaying exponential in the rotating frame, as shown in Figure 3.7. The FID sequence allows one to evaluate T_2^* and check if the system has been properly brought into resonance condition.

3.1.4 T_2 measurement techniques

Depending on the sample structure and its characteristics, it is possible to use two main sequences to study the T_2 relaxation time: **spin-echo** (SE) and Carr-Purcell-Meiboom-Gill **CPMG** sequences. They allow us to estimate the T_2 value by removing inhomogeneity effects caused by the static magnetic field or to reduce the diffusive contribution of a sample in the case of liquids.

The Spin-Echo sequence is obtained by sending two consecutive pulses, pulse $\pi/2$ and π, separated by a time τ_{echo} called **echo time**, with perpendicular directions in space.
Assuming that $\vec{H}_0$ is directed along $\hat{z}$ and the $\pi/2$ pulse is sent along $\hat{x}'$, the signal that would be generated, after a time τ_{echo}, is an FID, caused by the decay of $\vec{M}_{xy}$.
The application of a π pulse (in a perpendicular direction with respect to the $\pi/2$ pulse) is needed to rephase back the spins by flipping the accumulated magnetization $\vec{M}_{xy}$ on thex'-y' plane: the presence of static magnetic field inhomogeneities affects the spins relaxation by making them rotate with different frequencies and causing them to dephase their oscillation motion. For this reason, the second perturbation is sent orthogonally to $\hat{x}'$ (and to $\hat{z}$, the direction of $\vec{H}_0$), along the $\hat{y}'$ direction, allowing to completely reverse the spin orientations in the x'-y' plane and force them to refocus and rephase their magnetization. The pulse sequence is represented in Figure 3.8.

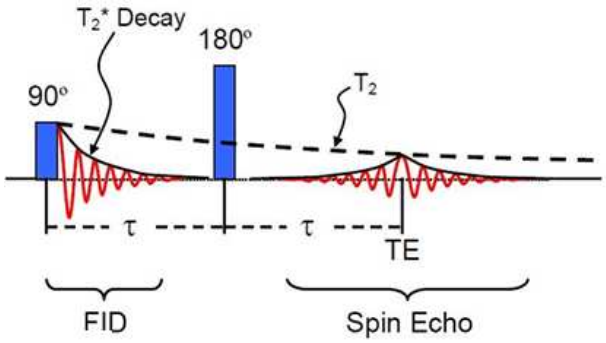

Figure 3.8: *Spin-Echo sequence representation, schematized as an FID sequence (and so a $\pi/2$ pulse along $\hat{x}'$) followed by a π pulse along $\hat{y}'$ after a time τ. TE is called time of echo and it is the time required to generate an echo signal after the sequence.*

Now, after another τ_{echo}, an echo signal is generated and it is generally described through a new modified Bloch equation of the form:

$$M_{xy} = M_o e^{\frac{-2\tau_{echo}}{T_2}} e^{-\gamma^2 G^2 D \frac{(2\tau_{echo})^3}{3}} \tag{3.22}$$

where D is the diffusion coefficient of the sample and G is a gradient of the magnetic field introduced to mimic any possible inhomogeneity of H_0. However, the SE sequence is valid only if the spins can be treated as fixed in their positions during the echo time, meaning that any diffusion contribution of those magnetic moments in the sample generates a loss in the signal.

In order to avoid the diffusion problem, Carr-Purcell-Meiboom-Gill created a new sequence, named after them **CPMG**: it consists of a combination of a certain number of π pulses along the $\hat{y}'$ direction, each of them spaced out in time by $2\tau_{echo}$, after the $\pi/2$ and π pulse combination (seen in the SE sequence) to remove any field inhomogeneities. It is designed to minimize the diffusion in the sample by reversing the magnetization multiple times in the x'-y' plane, causing the formation of multiple echo signals through which it is possible to reconstruct the entire magnetization curve. The representation of the sequence is given in Figure 3.9. The behavior

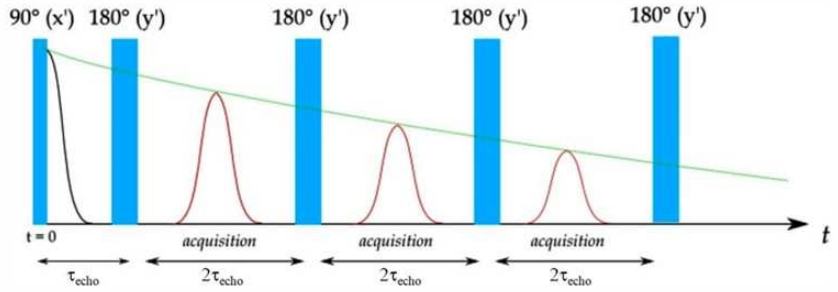

Figure 3.9: *CPMG sequence: an initial SE sequence, consisting of $\pi/2$ and π pulses, respectively along $\hat{x}'$ and $\hat{y}'$, followed by N total π pulses, all of them along $\hat{y}'$, to generate multiple echo signals that enable to completely reconstruct the decaying curve of the magnetization.*

follows a new equation that depends on N, the number of echoes collected, on the second power of $2\tau_{echo}$ and linearly with time t instead of its third power:

$$M_{xy} = M_o e^{(-t/T_2)} e^{(-\gamma^2 G^2 D (2\tau_{echo})^2 \frac{t}{12N^2})} \tag{3.23}$$

3.1.5 T_1 measurement techniques

For what it concerns the measurement of T_1, which can be expressed as the time required to reconstruct about 63% of the magnetization, one of the most common sequences is the **saturation recovery Spin-Echo** (SRSE) sequence.

It consists of the application of a sequence of n-$\pi/2$ pulses sent in the $\hat{x}'$ direction, each of them separated by a time τ_{sat} with the aim of fully reversing the magnetization in the transverse plane, and followed by a π pulse along $\hat{y}'$ to generate an echo signal.
As soon as it is tilted, the transverse magnetization starts to decay, while the longitudinal magnetization $\vec{M}_z$ starts to reconstruct. The fact that T_2 is much shorter than T_1, generally two orders of magnitude different, causes a faster decaying of the transverse component, making it impossible to reconstruct $\vec{M}_z$ completely. After n-$\pi/2$ pulses, the longitudinal magnetization gradually recovers and by waiting a total time τ_{rec}, called **time of recovery**, it is then possible to reconstruct the entire curve, described by:

$$M_z(t) = M_0(1 - exp(-\frac{\tau_{rec}}{T_1})) \tag{3.24}$$

By varying τ_{rec}, it is possible to acquire the signal at different heights, which is related to the degree of reconstruction of longitudinal magnetization. For τ_{sat}, the optimal time choice has to be such that $T_2 \ll \tau_{sat} \ll T_1$. The SRSE sequence is represented in Figure 3.10.

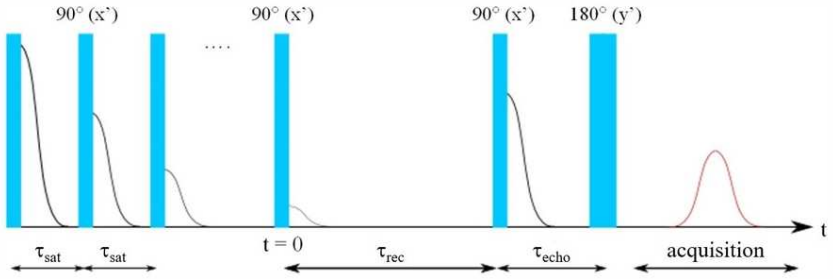

Figure 3.10: *Saturation recovery Spin-Echo sequence representation. τ_{sat} is the time separation between each $\pi/2$ pulse, τ_{rec} is the time duration that separates the n-$\pi/2$ pulses from the SE sequence and τ_{echo} the echo time.*

3.2 Fast Field-Cycling (FFC) NMR: low-frequency measurements

NMR experiments often relies on high values of the static magnetic field, such as few Tesla, to perform relaxometric studies but if we want to investigate the intrinsic behavior of a system at much lower frequencies (and so magnetic fields), a different approach is needed.

In the low-frequency range, the signal-to-noise ratio is very low, so the **Fast-Field-Cycling** technique, or **FFC**, enhances the signal by pre-polarizing the sample, allowing the acquisition of relaxation times down to frequencies of the order of 10 KHz. It exploits different values of $\vec{H}_0$ that range from 10^{-5} to 1 Tesla by varying its intensity during the duration of the application.

This is quite important because it enables to reconstruct the low-frequency part of an NMRD curve, which will be described in the following section [15].
At the base, the FFC circuit works in two modalities: **Pre-polarized** PP and **Non Polarized** NP.

In the Pre-Polarized mode, a first static magnetic field, called $\vec{B}_{POL}$, is applied along $\hat{z}$ at its maximum output (as we will see in Chapter 5 describing the materials of the experimental part, the STELAR SMARTracer Relaxometer operates at 8 mT max) in order to polarize the magnetic moments in the sample along the field direction and reach the saturation magnetization. The time duration T_{POL} of the field can be modified and is generally set to be 4 times the estimated T_1 of the sample. After that, multiple rapid switches can be executed on the field intensity, whose modify the current circulating in the coil that generates the field itself and bring the field from its maximum output to the minimum one.

These changes, electronically modulated and with a duration of 2-3 ms, are crucial to relax the polarized spins and measure their relaxation time parameter. For this reason, the field resulting after the switch is called **relaxation field** $\vec{B}_{RLX}$ and it is the one responsible for setting the system in resonance at the Larmor Frequency of $\omega_L = \gamma B_{RLX}$.

Lastly, a second switch is activated to increase the field intensity once again, resulting in a third static field $\vec{B}_{ACQ}$ called **acquisition field**, with the second maximum intensity possible (in our case the SMARTracer offers 7.2 mT), used to acquire the signal coming from the spins. Right after, a $\pi/2$ pulse, with frequency $\omega_{rf} = \omega_L$, is sent to the system in order to put it out of equilibrium and to generate an FID signal.

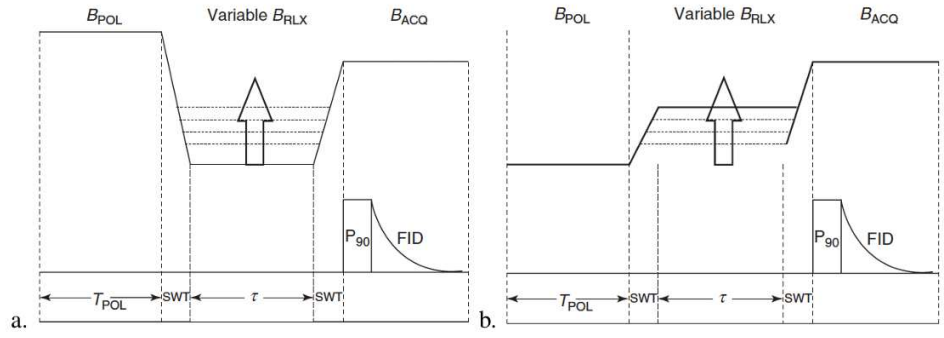

Figure 3.11: *(a) Pre-Polarized sequence acquisition and (b) Non-Polarized sequence acquisition in FFC Relaxometer [15].*

In case of Non-Polarized measurements, there is no polarizing field $\vec{B}_{POL}$, *i.e.*, $\vec{B}_{POL} = 0$, since this modality is mainly applied in the high frequency region (generally $\omega_L \geq 3.7$ MHz) for which it is not needed to pre-polarize the sample in order to make the spins more sensible for the acquisition field [15]. A scheme representing the PP and NP sequences is shown in Figure 3.11.

By varying the relaxing time τ for each acquisition and integrating the FID signal, a relaxation curve can be reconstructed, which has a different form based on the PP or NP technique.

In fact, for the Pre-Polarized sequence, at the time $\tau = 0$, the magnetization is saturated and has a value:

$$M_z(0) = M_0(B_{POL}) \tag{3.25}$$

As soon as $\tau \neq 0$, the magnetization starts to decay due to the decrease of the static field, according to:

$$M_z(\tau) = M_0(B_{RLX}) + [M_0(B_{POL}) - M_0(B_{RLX})]e^{-\frac{\tau}{T_1(B_{RLX})}} \tag{3.26}$$

which describes a decay curve for M_z.

For the NP sequence, $B_{POL} = 0$ and the previous equation becomes:

$$M_z(\tau) = M_0(B_{RLX}) - M_0(B_{RLX})]e^{-\frac{\tau}{T_1(B_{RLX})}} = M_0(B_{RLX})(1 - e^{-\frac{\tau}{T_1(B_{RLX})}}) \tag{3.27}$$

recalling a recovery behavior of the longitudinal magnetization, as shown in Figure 3.12.

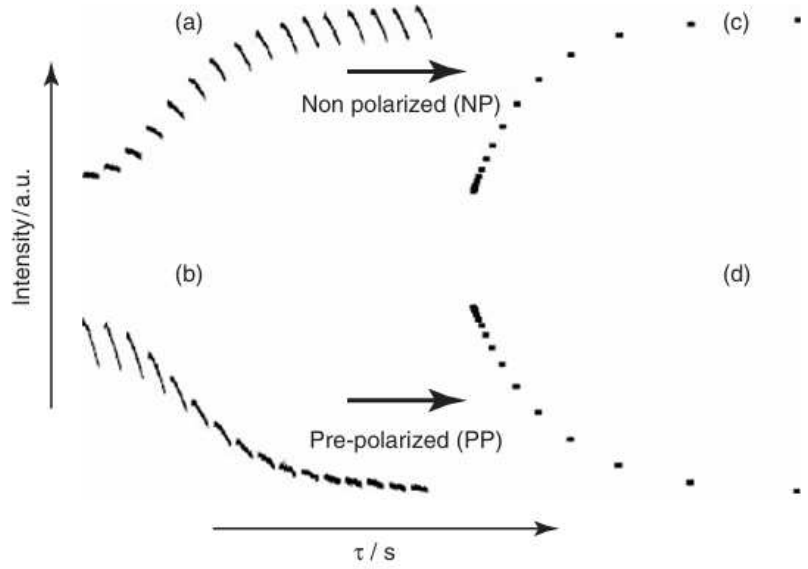

Figure 3.12: *Multiblock FID signal from (a) NP and (b) PP acquisitions. Curves (c) and (d) are obtained from the integration of their respective (a) and (b) curves from which a measure of* T_1 *can be evaluated [15].*

The Pre-polarization step is fundamental if a relaxometric study has to be performed at low frequencies, when the response signal is quite low.

On the other hand, this method has two important cons: one coming from the oscillating frequency that depends on $\vec{B}_{RLX}$, whose intensity is based on the magnet characteristics and cannot be too low, otherwise the system is affected by any "noisy" external magnetic field such as the Earth's one, and one from the dead time of the switch, which basically inhibit the possibility of measuring relaxing times that are lower than it, being usually of the order of few milliseconds.

To measure relaxation time parameters, a standard Saturation Recovery sequence can be used

to evaluate T_1, while for the T_2 measurement, which are less frequently performed with the FFC Relaxometer, only a Spin-Echo sequence is possible at low frequencies since the CPMG cannot be used under PP conditions.

For this reason, the resulting curve and measurement are expected to have a higher diffusion contribution compared to NP ones for which a CPMG sequence can be applied [15].

3.3 Proton relaxation induced by superparamagnetic nanoparticles

The characteristic use of superparamagnetic nanoparticles is to modify the relaxation times of the surrounding environment they are inserted in, *e.g.*, water. In fact, T_1 and T_2 relaxation times of the protons in the medium are shortened due to the intrinsic effects induced by the nanoparticles.

The **relaxivity** r_i is defined as the increase in the relaxation rate of a solvent, typically water, induced by 1 mmol/L of paramagnetic or superparamagnetic particles dispersed in it:

$$r_i = \frac{1}{C}\left(\frac{1}{T_{i_{obs}}} - \frac{1}{T_{i_{dia}}}\right) \tag{3.28}$$

expressed in $s^{-1}\ mM^{-1}$, and where i = 1,2 according to the considered relaxation time (1 for the longitudinal and 2 for the transverse one); C is the concentration of the para/superparamagnetic centers in the solution (expressed in mmol/L) while $T_{i_{obs}}$ and $T_{i_{dia}}$ are respectively the relaxation time of the aqueous system containing the magnetic agent and the relaxation time of the dispersant medium itself, often referred as the diamagnetic component of the material [18].

The same relation can be expressed as a function of the relaxation rate R_i, defined as the inverse of that relaxation time T_i, enhanced by the agent presence:

$$R_{i_{obs}} = \frac{1}{T_{i_{obs}}} = \frac{1}{T_{i_{dia}}} + r_i C \tag{3.29}$$

There are several mechanics with which the MNPs interact with the magnetic moments in the medium and they can be generally separated in two modalities: inner and outer sphere mechanisms [7].

The **inner sphere** relaxation considers the energy exchange between protons in the medium and the unpaired electrons located in the first hydration sphere of a paramagnetic center, which originates from the dipolar interaction.
Eventual fluctuations resulting from it are the sum of three main contributions:

- possible exchange of water molecules between the bulk water in the medium and the water in the first hydration sphere, described by a **residence time** τ_M for which that water

molecule remains inside it;

- rotation of the paramagnetic center characterized by a **rotation time** τ_R, which makes the spin rotate with the particle itself;
- intrinsic relaxation of the paramagnetic spin of the molecule described by the longitudinal and transversal correlation times τ_{S1} and τ_{S2}.

In the end, the total correlation time is given by the combination of all of them, giving:

$$\frac{1}{T_{Ci}} = \frac{1}{T_R} + \frac{1}{T_M} + \frac{1}{T_{Si}} \tag{3.30}$$

The **outer sphere** mechanism, on the other hand, considers the random diffusion of water molecules near paramagnetic ions and their local magnetic field, causing a dipolar coupling with characteristic time τ_D:

$$\tau_D = \frac{d^2}{D} \tag{3.31}$$

where D is the relative diffusion coefficient of protons and paramagnetic complex and d is the minimum approach distance [18] [19].

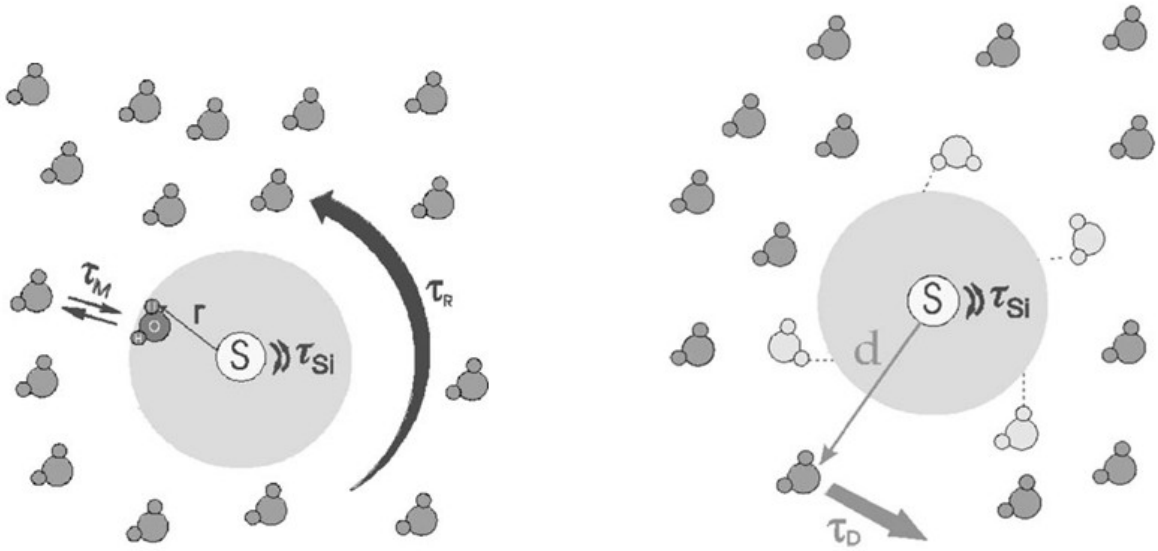

(a) *Inner sphere mechanism.* **(b)** *Outer sphere mechanism.*

Figure 3.13: *Representation of the inner sphere mechanism (a), characterized by the water residence time τ_M, electronic longitudinal and transverse relaxation times τ_{S_i} and the particle rotational correlation time τ_R, and of the outer sphere mechanism (b), characterized by the time parameters τ_{S_i} and the diffusion time τ_D [20].*

For small NPs with superparamagnetic behavior, the inner sphere contribution becomes negligible, while the outer one dominates. It should also be considered the contribution of the

Nèel relaxation τ_N, so a global correlation time can be defined:

$$\frac{1}{\tau_{c,outer}} = \frac{1}{\tau_N} + \frac{1}{\tau_D} \tag{3.32}$$

The relaxation efficiency produced by those fluctuations depends on the correlation time τ_C and the precession frequency of the proton spins ω_I over the external magnetic field $\vec{H}_0$.

For $\omega_I \cdot \tau_C < 1$, the precession is not enough to average the fluctuations and a relaxation in the system is generated. For $\omega_I \cdot \tau_C > 1$, no fluctuations are produced since the precession frequency is too fast and the system is not relaxed. The maximum effect is achieved when $\omega_I \cdot \tau_C = 1$, a condition that also defines a threshold over which τ_C cannot produce any further relaxation.

The precession motion of the crystal magnetic moment can also be extended to the electron moments, described by a gyromagnetic ratio γ_e that is nearly 658 times bigger than γ_I, meaning that an electron rotates with an angular frequency ω_e 658 times faster than the one of the protons [16]. Because of this, the electronic dispersion, centered around $\omega_S \tau_c \sim 1$ instead, appears at fields much lower than the dispersion centered around the proton frequency ω_I [18].

3.4 RMG model and MAR/SDR models for MNPs

Nuclear magnetic relaxation dispersion (NMRD) profiles are obtained from the study of relaxavity r_i of a magnetic system as a function of the external magnetic field applied, usually expressed in terms of proton Larmor frequency, from which it is possible to extrapolate microscopic properties of the relaxing agent and determine the field condition at which it provides the maximum efficiency.

As it was discussed in the previous paragraph, superparamagnetic relaxation effect is well described by the outer sphere theory, for which water protons relax faster because of their free diffusion inside a non-homogeneous local magnetic field generated by the mean moment of a crystal, a phenomenon also known as **Curie's relaxation**, and to the Nèel and Brown relaxation mechanisms.
In addition to that, anisotropy plays a huge role in relaxation rate studies, since it directly influences the Nèel relaxation time as a result of its dependence on the nanoparticle size and anisotropy constant (related to the characteristics of the particle itself).

NPs can be generally separated in two main categories according to their dimension:

- **SPIO**, small particles of iron oxide, referred to those "large" NPs with an average diameter greater than 15 nm;
- **USPIO**, ultra-small particle of iron oxide, corresponding to those particle with a crystal diameter inferior to 15 nm.

To describe the relaxation behavior, two different limits for the anisotropy have been considered: **high** and **low-intermediate anisotropy**.

3.4.1 High anisotropy model

When the anisotropy energy is greater than the thermal energy, which typically occurs in larger nanoparticles or crystals with an high anisotropy constant, the SPM spin is blocked along the anisotropy easy axis and no electronic precession over $\vec{H}_0$ is possible.
Depending on the intensity of the external applied field, the relaxation behavior dynamically varies as it describes the magnetic fluctuations generated by the change in spin orientation over time along the different easy directions [19].

At low fields, the relaxation induced in protons originates from the dipolar interaction between proton and MNP spins mediated by the diffusion motion of the water molecules and Nèel relaxation. Those two contributions are collected in the so called **Freed spectral density function**, characterized by a correlation time τ_C and with an inflection point on the condition $\omega_I\,\tau_C = 1$:

$$J_F(\omega_I, \tau_D, \tau_N) = Re\left(\frac{1 + \frac{1}{4}\Omega^{1/2}}{1 + \Omega^{1/2} + \frac{4}{9}\Omega + \frac{1}{9}\Omega^{3/2}}\right) \tag{3.33}$$

where $\Omega = \tau_D(i\omega_I + 1/\tau_N)$. From this equation, the longitudinal and transverse relaxation rates can be derived as follows:

$$R_1 = 1/T_1 = 10c\mu^2 J_F(\omega_I, \tau_D, \tau_N) \tag{3.34}$$

and

$$R_2 = 1/T_2 = c\mu^2[8J_F(\omega_I, \tau_D, \tau_N) + 2J_F(0, \tau_D, \tau_N)] \tag{3.35}$$

with c = $\frac{32\pi}{405000}\gamma^2 N_A[M]/r^3$, N_A the Avogadro constant, γ the proton gyromagnetic ratio, μ the magnetic moment of the particle, r the radius of the particle and *[M]* the molar concentration of SPM particles [19] [21].

At high fields, the spin orientation is blocked along the external magnetic field direction, so that no Nèel relaxation is allowed ($\tau_N \sim \infty$) and the dominant relaxation contribution comes from Curie relaxation. The function used to describe this different contribution is called **Ayant spectral density function** J_A:

$$J_A(z) = Re\left(\frac{1 + \frac{5z}{8} + z^2}{1 + z + z^2/2 + z^3/6 + 4z^4/81 + z^5/81 + z^6/648}\right) \tag{3.36}$$

where $z = \sqrt{2\tau_D\omega_I}$. The new correlation time is instead called τ_D, with which the condition

$\omega_I \tau_D = 1$ is achieved. The relaxation rate relations become:

$$R_2 = c\mu^2[4.5J_a(\sqrt{\omega_I \tau_D}) + 6J_a(0)] \tag{3.37}$$

and

$$R_1 = c\mu^2[9L^2(x)J_A(\sqrt{\omega_I \tau_D})] \tag{3.38}$$

where *L(x)* is the Langevin function, with $x = \frac{M_s V B_0}{k_B T}$.

For intermediate values of the external field, R_1 and R_2 are given by a combination of the low and high field components, meaning that both Ayant and Freed spectral density are required:

$$\begin{aligned} R_1 = c\mu^2 \Bigg\{ & \left(\frac{L(x)}{x} \right) \cdot 21\, J_F(\omega_I) \\ & + 9 \left[1 - L^2(x) - 2 \left(\frac{L(x)}{x} \right) \right] \cdot J_F(\omega_I) \\ & + 9\, L^2(x) \cdot J_A \left(\sqrt{2\omega_I \tau_D} \right) \Bigg\} \end{aligned} \tag{3.39}$$

and

$$\begin{aligned} R_2 = c\mu^2 \Bigg\{ & \left(\frac{L(x)}{x} \right) \cdot 19.5\, J_F(\omega_I) \\ & + \left[1 - L^2(x) - 2 \left(\frac{L(x)}{x} \right) \right] \cdot 4.5\, [J_F(\omega_I) + 6J_F(0)] \\ & + L^2(x) \cdot \left[4.5\, J_A \left(\sqrt{2\omega_I \tau_D} \right) + 6J_A(0) \right] \Bigg\} \end{aligned}$$

A schematic representation of various contributions to the proton relaxation is shown in Figure 3.14.

This model is suited to describe the behavior of SPIO particles due to their larger dimensions and anisotropy energies. In contrast, for smaller particles with a low anisotropy energy barrier, the low-field region does not experimentally match the NMRD curve profile, as shown in Figure 3.15 [18] [19].

3.4.2 Low-intermediate anisotropy model

The previous model assumed a system of NPs with almost infinite anisotropy energy for which the magnetic moments of the particles could be considered blocked along the anisotropy axis direction, depending on the intensity of the external field; if the size of the NPs is reduced under a certain critical radius (generally below 7.5 nm), the anisotropy energy of the system decreases, and it is no more sufficient to sustain the superspin along the easy direction due to the growing

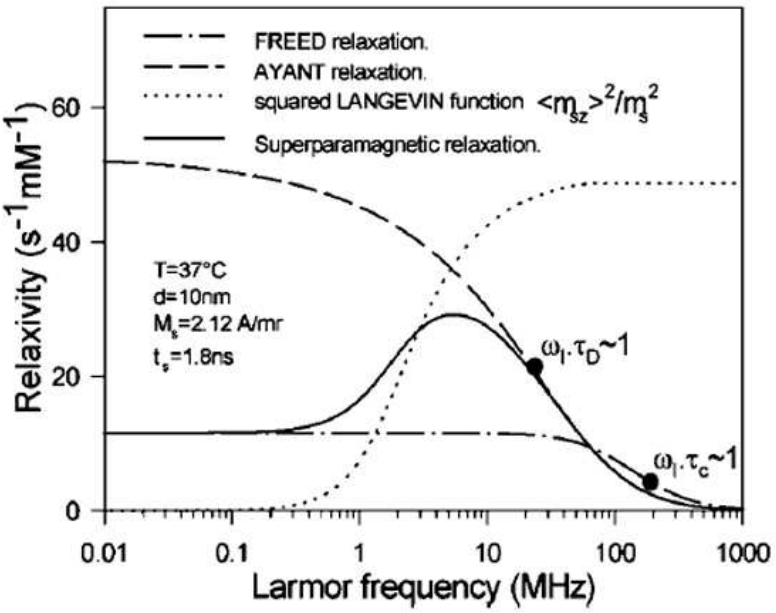

Figure 3.14: *Different contributions to the proton relaxation for magnetic crystals with elevated anisotropy [18].*

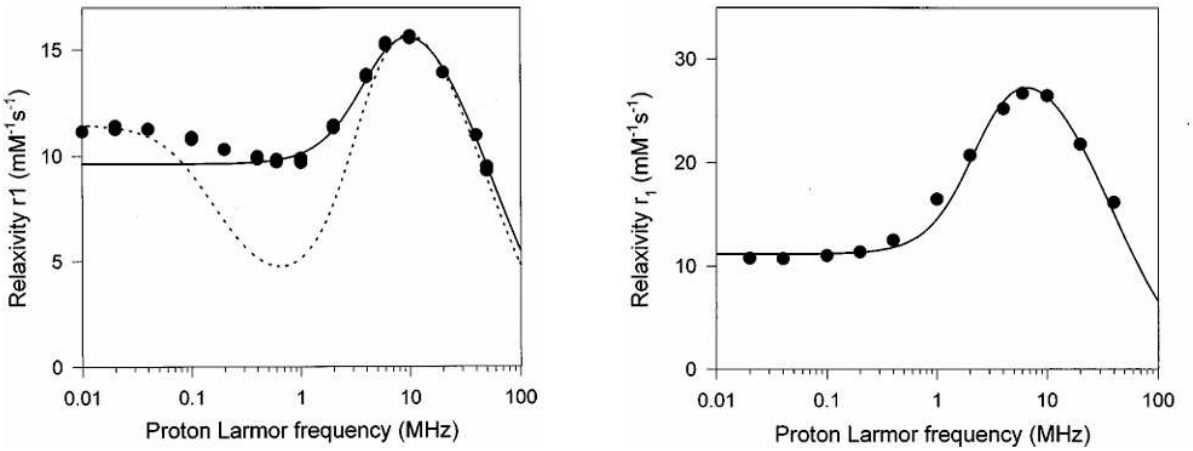

Figure 3.15: *Left picture: NMRD profile of a suspension of USPIO magnetite particles with R = 5 nm; Right picture: NMRD profile of a SPIO suspension of magnetite (R > 15 nm) [21].*

challenging contribution of the thermal energy.
Compared with the precedent scenario, the magnetic moment now may easily change its orientation and precess around $\vec{H}_0$, causing a low field region dispersion on the NMRD curve [19].

In the **Roch-Müller-Gillis** theory [21], the authors assume a quantum approach to explain the low-anisotropy behavior of NPs described above, which can be interpreted and explained by making three important assumptions: first, at low scale, the dominant interaction is the exchange interaction, which makes all the spin align along a certain crystal easy direction for which the

resulting magnetic moment is the "superspin". Second, a small particle volume implies a smaller Nèel time τ_N compared to the rotation time τ_R, so that the resulting correlation time:

$$\frac{1}{\tau_C} = \frac{1}{\tau_N} + \frac{1}{\tau_R} \tag{3.40}$$

becomes:

$$\tau_C \sim \tau_N \tag{3.41}$$

as $\tau_N << \tau_R$.

The third assumption imposes that the correlation time τ_N is the same for all electronic spin energy levels, not always valid unless the spins have the same occupation probability, which, on the other hand, is much more probable in the case of small nanoparticles and so low anisotropy [21].

Even if the model is now able to represent the dispersion at low fields, no analytical solution can be extrapolated from it, and the resulting calculations are quite difficult to compute. A substitute heuristic model can be used instead, experimentally predicting the proton relaxation curves in the limit cases of null and infinite anisotropy with the use of an additional parameter P:

$$\begin{aligned}\frac{1}{T_1} = &\left(\frac{32\pi}{135000}\right)\mu_{\mathrm{SP}}^2\gamma_I^2\left(\frac{N_a C}{RD}\right)\\ &\times\left\{\frac{7PL(x)}{x}J^F(\Omega(\omega_s,\omega_0),\tau_D,\tau_N) + \left[\frac{7QL(x)}{x} + 3\left(1 - L^2(x) - \frac{2L(x)}{x}\right)\right]J^F(\omega_I,\tau_D,\tau_N)\right.\\ &\left. + 3L^2(x)J^A\left(\sqrt{2\omega_I\tau_D}\right)\right\},\end{aligned} \tag{3.42}$$

$$\begin{aligned}\frac{1}{T_2} = &\left(\frac{16\pi}{135000}\right)\mu_{\mathrm{SP}}^2\gamma_I^2\left(\frac{N_a C}{RD}\right)\\ &\times\left\{\frac{13PL(x)}{x}J^F(\Omega(\omega_s,\omega_0),\tau_D,\tau_N) + \frac{7QL(x)}{x}J^F(\omega_I,\tau_D,\tau_N) + \frac{6QL(x)}{x}J^F(0,\tau_D,\tau_N)\right.\\ &\left. + \left[1 - L^2(x) - \frac{2L(x)}{x}\right]\left[3J^F(\omega_I,\tau_D,\tau_N) + 4J^F(0,\tau_D,\tau_N)\right] + L^2(x)\left[3J^A(\sqrt{2\omega_I\tau_D}) + 4J^A(0)\right]\right\}\end{aligned} \tag{3.43}$$

where P ranges between 0 and 1, the two limit cases, that means high anisotropy when $P = 0$, and low anisotropy when $P = 1$, and where $\Omega(\omega_s, \omega_0)$ is given by:

$$\Omega(\omega_s,\omega_0) = \begin{cases}\left(\omega_s^{1/4} - \omega_0^{1/4}\right)^4, & \text{if } \omega_s > \omega_0,\\ 0, & \text{if } \omega_s \leq \omega_0.\end{cases}$$

and represents the dispersion at low frequencies [21].

3.4.3 NMRD profile analysis

NMRD profile analysis plays a crucial role in the characterization and potential application of magnetic nanoparticles and assessing the efficacy of these superparamagnetic nanoentities implies to maximize their performance as possible relaxation modifier. When these nanoentities accumulate in a specific region, in fact, they modify the relaxation of the water protons and so their response when influenced by external magnetic fields [18].

Such studies can be carried out by determining the magnetic and morphological properties of the MNPs by fitting the NMRD profile of the longitudinal and transverse relaxivities according to the aforementioned models and theories. The most common parameters obtained from the fit of a typical NMRD curve, such as that in the figure, are:

- **average radius** r, which can be estimated from the diffusion time τ_D at high fields where the $\omega_I \tau_D = 1$ condition is valid and from $\tau_D = r^2/D$;
- **saturation magnetization** M_s, estimated at high fields from the condition $M_s = (\frac{R_{max}}{C\tau_D})^{1/2}$, where C is a constant and R_{max} the maximum relaxation rate;
- **anisotropy energy** E_a, which can be higher or lower than the thermal energy, depending on the absence or presence of dispersion at low field;
- **Néel relaxation time** τ_N, estimated from the low-field relaxation rate R_0, which is governed by a correlation time τ_{C0} at zero magnetic field equal to τ_N when $\tau_N << \tau_D$. However, the latter condition is not always achieved, and the estimation provides only qualitative information [22].

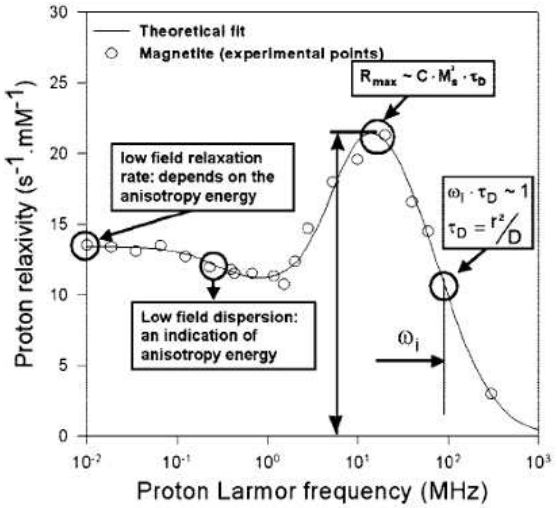

Figure 3.16: *Longitudinal relaxivity NMRD profile for a magnetite colloidal dispersion [18].*

3.4.4 MAR/SDR models for the transverse relaxation rate R_2

A different way to study and analyze the transverse relaxivity is given in the MAR-SDR model developed by Vuong et al. [22]. It allows to establish a universal scaling law to predict the value of r_2 knowing, for clusters of particles, their diameter, volumetric magnetization and volume fraction of magnetic material, while for single USPIO systems, only their diameter and volumetric magnetization are needed. The system is described in two different regimes, respectively called MAR, **Motional Averaging Regime**, and SDR, **Static Dephasing Regime** [22].

In the MAR model, protons can freely diffuse inside the non-homogeneous magnetic field generated by the NP magnetic moments, as described in the outer sphere mechanism, for which the relaxation rate is given by:

$$R_2 = \frac{16}{45} f \tau_D (\Delta\omega)^2 \tag{3.44}$$

with τ_D the diffusion time of the proton, equal to R^2/D where R is the particle/cluster radius and D the diffusion coefficient of water, $\Delta\omega = \mu_0 M\gamma/3$ is the difference in the angular frequency between the frequency experienced by the proton at the cluster surface and in the bulk component of the solvent and f is the volume fraction occupied by the cluster/particles in the suspension.
This regime allows properly to fit relaxation data when the Redfield condition is verified, which means that:

$$\Delta\omega\tau_D < 1 \tag{3.45}$$

To evaluate the transverse relaxivity, the relaxation rate has to be normalized by the equivalent iron concentration [Fe], which can be found using the general relation for iron spinel $MO \cdot Fe_2O_3$ structures:

$$f/[Fe] + [M] = V_{mol} = \frac{M_{MOFe_2O_3}}{3\rho_{MOFe_2O_3}} \tag{3.46}$$

where V_{mol} is the molar volume and ρ is the density of the iron spinel. M is a divalent cation, such as Fe^{2+}, Co^{2+} etc.
Then, r_2 can be expressed as:

$$r_2 = \frac{R_2}{[Fe]} = \frac{4\gamma^2\mu_0^2 V_{mol} M_V^2 d^2}{405D} \tag{3.47}$$

where d is the particle diameter [22]. If we divide it by the square of the magnetization, the relation becomes of the form:

$$\frac{r_2}{M_V^2} = a \cdot d^2 \tag{3.48}$$

with $a = 5.9 \times 10^{-12}$ if $D = 3 \times 10^{-9}$ $m^2 s^{-1}$ is the water diffusion coefficient in water at 37°.

In case of particle aggregation, Vuong et al suggest the introduction of an intra-aggregate

correction term ϕ_{intra} to be added to the previous r_2 relation, which becomes:

$$r_2' = \frac{r_2 \cdot \phi_{intra}}{M_V^2} = a' d^2 \tag{3.49}$$

where $a^{'} = 11.6 \times 10^{-12}$ [22].
A cluster can be idealized as a bigger magnetic sphere characterized by a different magnetic moment, given by the vector sum of all the magnetic contributions inside it, and a longer correlation time, for which the interactions occurring with nearby water protons differ significantly from those of an isolated nanoparticle. Its global structure and the magnetic field produced by the cluster, in fact, alter the local magnetic field distribution around and cause a faster dephasing of the spins, strongly affecting their transverse relaxivity r_2 [19].
As shown in Figure 3.17, the data representing both USPIO (single cores) and SPIO clusters are well fitted in a size range from 4 to 300 nm.

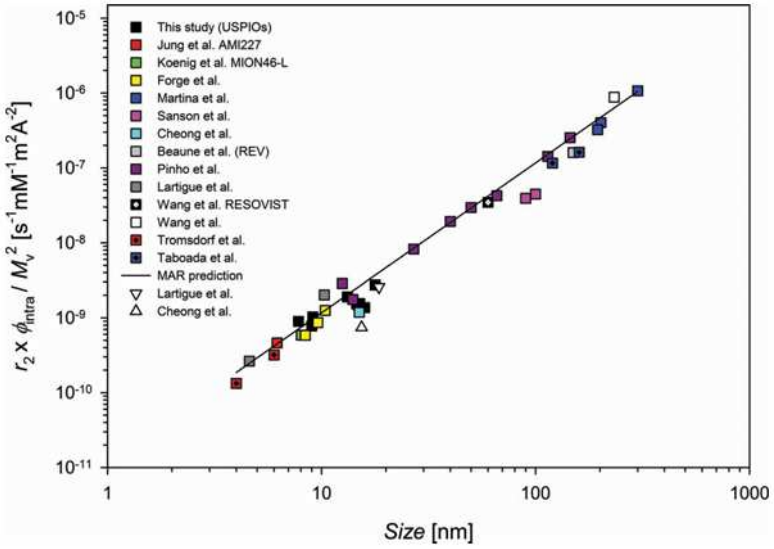

Figure 3.17: *r_2 values in the MAR regime as a function of the particle size. Values normalized by the square of the magnetization at high field ($\geq 1T$) and at 37° [22].*

When the Redfield condition is no longer satisfied, the MAR model is no longer valid and the SDR model is applied instead; in this regime, the validating condition becomes:

$$\Delta\omega\tau_D > 1 \tag{3.50}$$

This model is primarily valid for larger NPs, whose magnetic field can be considered to be basically static. The diffusion motion of the water protons is then limited to the point that they can be treated as motionless magnetic moments in a non-uniform magnetic field generated by their magnetic dipoles [22].

The resulting relaxation rate is now:

$$R_2^* = 1/T_2^* = \frac{2\pi}{3\sqrt{3}} f \Delta\omega \sim R_2 \tag{3.51}$$

and, when normalized by the iron molar concentration, the relaxivity becomes:

$$r_2^* = \frac{R_2^*}{[Fe]} = \frac{2\pi\gamma\mu_0 V_{mol} M_V}{9\sqrt{3}} \sim r_2 \tag{3.52}$$

SDR model does not take into account the eventual effects produced by the refocusing pulses used in T_2 measurement sequences, meaning that the results account for R_2^* and r_2^*.

SDR equations work only in a particular range of $\Delta\omega\tau_D$ since the system shifts between the different regimes: if $\Delta\omega\tau_D > 20$, a third regime called **partial refocusing model** "PRM" regulates the proton relaxation, for which the hydrodynamic diameter of a MNP increases to a point where its magnetic core and the outer region water protons become so distant that any refocusing pulses on the system are now effective [19].
Conversely, for $1 < \Delta\omega\tau_D < 5$, neither the MAR nor the SDR formulas accurately approximate R_2 and r_2, as the system experiences a transition between the two regimes.

As a result, the applicable frequency range is restricted to $5 < \Delta\omega\tau_D < 20$, with the maximum effect achieved when $\Delta\omega\tau_D \sim 10$ [22].

Chapter 4

Biomedical applications for magnetic nanoparticles

In recent years, magnetic nanoparticles (MNPs) have attracted considerable attention due to their unique magnetic and chemical properties, making them suitable for a wide range of biomedical applications. In fact, their tunable magnetic behavior, nanometric size, large surface-to-volume ratio, and possible functionalizable surface allow them to be integrated into diagnostic, therapeutic, and theranostic platforms [13]. Among the most explored applications, MNPs have been employed as contrast agents in magnetic resonance imaging (MRI), as mediators for localized heating release in magnetic fluid hyperthermia (MFH), and also as targeted drug delivery due to their sensitivity to external magnetic fields. All of these applications exploit different aspects of their magnetic response, ranging from their ability to enhance or decrease the relaxation signal in their accumulation regions, to the generation of heat when exposed to an alternating magnetic field. At the same time, some issues are still being studied to improve their clinical translation, as well as their colloidal stability, biocompatibility, and toxicity.

This chapter will first discuss the physicochemical properties of MNPs that are relevant to their biomedical use, followed by an overview of their common applications with a particular focus on MRI and MFH. Special attention will also be given to iron-gold nanoparticles, as they are the core of this thesis work.

4.1 Physicochemical properties and synthesis methods of MNPs

In Chapter 2, the concept of magnetic nanoparticle (MNP) was introduced and discussed, presenting all the fundamental properties that characterize it.
MNPs have a special role in a wide range of biomedical applications, such as diagnostics, serving as contrast agents for magnetic resonance imaging, or providing therapeutic effects as heating mediators in magnetic fluid hyperthermia and drug delivery. Morphostructural and magnetic properties, such as size, shape and elemental composition, determine their efficiency in each field of interest.

Reducing the magnetic particle size to the nanometric scale, usually below 100 nm, is key to generate a transition from a multi-domain configuration of the system into a single-domain one, for which, at even smaller sizes, they can enter the superparamagnetic regime, characterized by fast change of their magnetic state when an external field is applied (due to their higher magnetic susceptibility) and large "super" magnetic moment with no coercivity and no magnetic remanence at room temperature [23].

Moreover, these nanosystems possess a high surface-to-volume ratio, making them highly reactive and versatile if compared to their bulk counterparts; in terms of biological applications, thanks to their size comparable to that of bacteria and DNA strands, they can circulate in blood vessels for a longer time before being detected and eliminated, implying a much higher probability of penetrating inside the cellular membrane and effectively entering the intercellular environment.

MNPs can have different shapes and dimensions according to their specific applications: they can be represented as nanospheres, often constituted by ferrites (see Chapter 2 for the description) such as magnetite (Fe_3O_4) and maghemite (γ-Fe_2O_3), dispersed in a matrix (like water, gels and oils), taking the name of **ferrofluids** or **magnetic hydrogels**. The choice of iron-oxide, often referred to as the NP core, is motivated not only by its superparamagnetic behavior but also by its excellent biocompatibility with biological systems and chemical stability at ambient conditions [24].

However, these kinds of superparamagnetic structures tend to aggregate due to Van der Waals forces, attractive interactions with increasing intensity as the size of the interacting particle increases, leading to the formation of clusters of particles and possibly causing instability and intravenous diseases once injected into the patient's body. Furthermore, iron-oxide cores tend to chemically react with air, leading to oxidation and a consequent loss of magnetic susceptibility. When injected into the bloodstream, they can also be readily recognized by the reticuloendothelial system (RES) of the human body (responsible for detecting anomalies and foreign entities) and subsequently eliminated through phagocytic activity [7].

To overcome this, the core is covered with a coating, often made by surfactants [1] , polymers or carbons. It provides stability and protection to MNPs from biodegradation while circulating in the body, prevents the formation of aggregates by reducing the attractive forces between the superparamagnetic centers, and improves biocompatibility, thus diminishing residual toxic effects. It can also be used as an additional surface area over which it is possible to attach other NPs or ligands for many different functionalities, a process called **biofunctionalization**: proteins, antibodies, enzymes, etc., are placed on top of the coating to exploit their selective abilities for targeted drug delivery in tumors and biodetection, as can be seen in Figure 4.1 [23].

From a physical point of view, the coating can be engineered to be neutral or electrically charged, a fundamental functionality required to avoid electrical interactions with cell membranes or to improve particle selectivity with other charged structures. The coating can also be optimized in its thickness to increase the distance between two nearby magnetic dipoles (steric repulsion) and reduce the possible aggregation.

These features are essential for nanoentities that need to circulate for extended periods in the body, aiming to reach their target, and avoiding interactions with healthy tissues or organs.

One of the most commonly used morphologies for nanoparticles is the **core-shell** structure, consisting of a core (*e.g.*, ferrites) coated with another material, called shell. The shell itself can interact with the core, as it can be made of organic or inorganic polymer layers, relevant in terms of stability and biocompatibility of the particle, or of another ferro, antiferro, or ferrimagnetic metal, such as gold or silver, which can change the physical and biological capabilities of the system and make it more biocompatible and bioactive. These systems are mainly designed for biomedical applications, as the surface chemistry enhances the binding affinity of ligands, drugs, and receptors [25].

4.1.1 NPs synthesis methods

The synthesis of a specific class of nanoparticles is a crucial step, as their morphology determines their properties. The size of MNPs usually follows a **log-normal** distribution:

$$f(d) = \frac{1}{\sqrt{2\pi\sigma^2}d} exp[-\frac{ln^2(d/d_0)}{2\sigma^2}] \tag{4.1}$$

where d is the average diameter and σ is the standard deviation of the normal distribution. The latter shows the degree of dispersion of the NPs, which is fundamental to understand if the nanoentities were produced with (approximately) the same size, so their distribution is narrower around a certain more probable diameter [14].

[1]Surfactants are amphiphilic molecules with a hydrophilic head and a hydrophobic tail. They are commonly used as stabilizing or capping agents for nanoparticles to prevent aggregation, control size and shape during synthesis, and improve dispersibility [18].

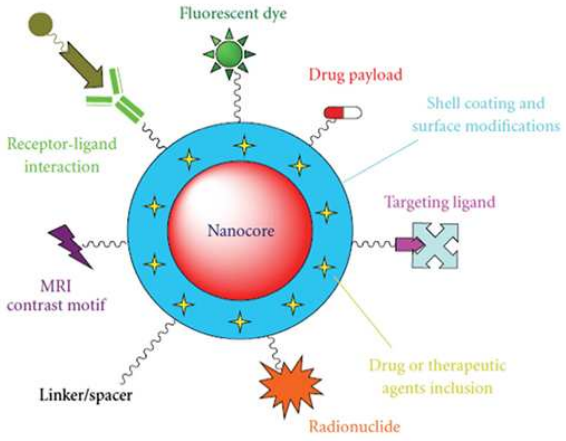

Figure 4.1: *Multifunctionalized core-shell NPs for molecular imaging, drug delivery and therapy [25].*

The most common methods to produce a set of nanoparticles are the **co-precipitation** and **thermal decomposition**.

The co-precipitation technique is based on a stoichiometric mixture of ferric and ferrous salts in an aqueous solution, with the addition of a basic agent such as NH_4OH or NaOH, according to the chemical reaction:

$$M^{2+} + 2Fe^{3+} + 8OH^{-} \rightarrow MFe_2O_4 + 4H_2O \tag{4.2}$$

where M is a divalent cation (*i.e.*, Fe^{2+}, Co^{2+}, etc.). This method can be easily replicated and produces sets of NPs with a possible average diameter of 50 nm in an aqueous salt solution. Despite that, a broad size distribution and irregular morphology of the particles are still unavoidable outcomes of the synthesis procedure [23].

The thermal decomposition technique employes the use of **organometallic precursors**, such as $[M^{n+}(\text{acetylacetonate})_n]$ (where M is Fe, Ni, Co etc, and n is 2 or 3), or carboxyls, for instance $Fe(CO)_5$, mixed in a nonpolar solvent with the addition of a stabilizer, like oleic acid or hexadecylamine, under high temperature conditions. The stabilizer is required to control the nucleation process and particle growth, so that MNPs with a spherical shape and a size inferior to 30 nm can be precisely synthesized. The use of organometallic precursors leads to the formation of metallic NPs, which will oxidize and form monodisperse metal oxides. This kind of process is optimal for producing nanoparticles with a high level of control over the morphology and a narrow size distribution [23].

NPs can be obtained in various shapes, but we can divide them in two main categories: **smooth surface particles**, characterized by a smooth, regular shaped surface (generally spherical or quasi-spherical) which gives them a uniform, homogeneous magnetic response, and **branched particles**, which instead exhibit a non-regular surface with bumps or spikes that create regions

where both magnetic and electric fields are locally amplified, also named "hot-spots" [26] [27].

4.2 Main biomedical applications: MRI and MFH

Several applications for MNPs have been cited in the previous paragraph; however, two of them deserve to be explored and discussed, as they are the most studied and researched: **Magnetic Resonance Imaging** MRI and **Magnetic Fluid Hyperthemia** MFH.

Both are based on the administration of a MNP dispersion to sustain a diagnostic exam, in the case of MRI, or to generate a tumor-killing effect, in the case of MFH, onto the target region of interest, showing the enormous versatility of these magnetic nanosystems.

4.2.1 Magnetic resonance imaging

One of the most important applications of NMR, in the biomedical field, is the **magnetic resonance imaging** MRI. This non-invasive diagnostic technique is based on the use of NMR sequences (see Chapter 3) combined with magnetic field gradients, to produce high resolution and high contrast images of tissue structures and to provide information about their functional properties.

The human body is known to be composed of nearly 70% of water, whose hydrogen nuclei (*i.e.*, protons) constitute a fundamental source of MRI signal. This diagnostic technique doesn't require the patient to be exposed to ionizing radiation, unlike CT or X-ray radiography, since the signal is produced from the relaxation of the protons.

The typical MRI signal has the following form:

$$S(t) \propto \rho e^{-\frac{TE}{T_2}} (1 - e^{-\frac{TR}{T_1}}) e^{-bD} \tag{4.3}$$

where ρ is the hydrogen nuclei density in the sample, TE and TR respectively the time of echo and repetition time of the pulse sequence used, and D the diffusion coefficient (the latter term can often be neglected when diffusion is negligible).

The generated image is characterized by different shades of gray, reflecting the intensity of the proton signal in each region, primarily depending on their density: white spots in the image correspond, in fact, to a great amount of hydrogen nuclei and stronger signals from that region, while dark spots indicate regions with low proton density and weak signal intensity.

Its intrinsic contrast can be modulated by changing the TE and TR parameters with respect to T_1 and T_2 relaxation times, to acquire **T1-weighted** and **T2-weighted** images and better visualize structures with high or low values of the corresponding relaxation times. The image contrast can be also enhanced using **contrast agents** (CAs): the signal is altered by injecting a dispersion of magnetic nanoparticles, responsible for interacting with the magnetic moments of the protons

and locally changing the signal of those regions where the agents accumulate, in this way we can discriminate lesions otherwise challenging to detect.

Different behaviors can be observed depending on the type of agent used to perform a certain contrast modification. Those dispersions can be divided into two separate classes: **positive CAs** or **negative CAs**.

The first class refers to magnetic particles that act more strongly on the relaxation time T_1 by shortening it, consequently generating a decrease in T_1 and an intensification of the MRI signal, which will make that contrast-modified region brighter in the image. These T_1 relaxing-CAs are associated with magnetic systems that exhibit a paramagnetic behavior, as in the case of gadolinium Gd^{3+}, responsible for the dipolar interaction between their magnetic moment and the proton spins, inducing faster relaxation [28].

The second class is conversely associated with the shortening of the relaxation time T_2, which suppresses the signal from the relaxed spins due to the action of contrast agents. This is associated instead with the intense superspin of the nanoparticles, which locally perturbs the magnetic field at the nuclear site level, mostly influencing the transverse component of the proton moments, as discussed in the previous chapter. For this reason, this class is also named T_2 relaxing-CAs and exploits iron oxide cores (such as magnetite and maghemite) that show superparamagnetic behavior at room temperature. In Figure 4.2, is shown an example of MRI images in the presence and absence of CAs.

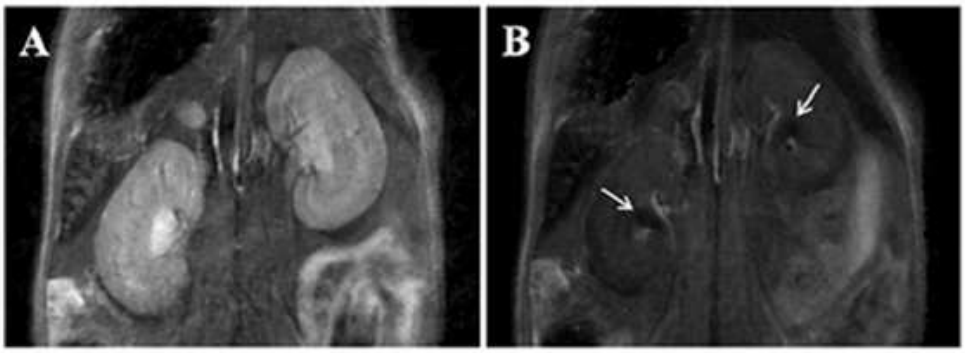

Figure 4.2: *Kidneys MRI images before (A) and after (B) the injection of a MNP-GA-PEG-OH CA dispersion [29].*

4.2.2 Magnetic fluid hyperthemia

Magnetic fluid hyperthemia is an anticancer therapy based on the increase in temperature of a local region up to 41 to 45 °C, taking advantage of the great sensitivity of tumor cells to heat compared to normal tissues. The hyperthermia treatment consists of the injection of a dispersion of MNPs in the tumor region and the application of an external oscillating magnetic field to the designated

target area: its electromagnetic energy is absorbed by the nanoparticles, which, in turn, dissipate it locally as heat, selectively killing tumor cells. A schematic representation of hyperthermia tumor treatment is shown in Figure 4.3. Moreover, this treatment can be administered separately or in combination with other cancer therapies, such as chemotherapy or radiotherapy, to increase their efficacy through synergistic effects [23] [29].

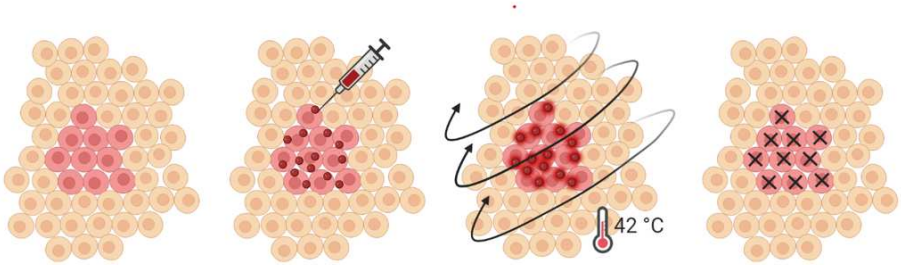

Figure 4.3: *Schematic representation of MFH treatment.*

The main mechanisms by which SPM nanoparticles generate heat are the Nèel and Brownian relaxation: the Nèel relaxation mechanism considers the internal reorientation of the superspin of a MNP under the influence of an external alternating magnetic field, between the two opposite directions of the easy axis determined by the magnetic anisotropy. The Brownian mechanism, instead, assumes that the magnetic moment experiences a torque that induces the physical rotation of the NP within the medium, generating friction between the NP surface and the solvent in which the nanosystem is dispersed. Both occur in parallel and are governed by different relaxation times (τ_N and τ_B), with the faster relaxation mechanism dominant in the heat production [23].

The efficiency of a given material in converting electromagnetic energy into heat, at specific frequencies and intensities of the alternating magnetic field, is quantified by the **specific absorption rate** or SAR (Wg^{-1}):

$$SAR = \frac{C}{m}\frac{\Delta T}{\Delta t} \tag{4.4}$$

where C is the specific heat capacity of the medium (for water, $C_{water} = 4185\ \mathrm{Jkg}^{-1}\mathrm{K}^{-1}$), m is the magnetic material mass in the dispersion and $\Delta T/\Delta t$ is the initial slope of the temperature increase as a function of time during the application of the alternating magnetic field [23].

SAR is influenced directly by the properties of MNPs, such as their saturation magnetization, anisotropy, and morphology, as well as by the solvent in which they are dispersed, according to its viscosity and heat capacity.

The reduced sizes of MNPs allow them to reach the tumor by intravenous administration and accumulate selectively within it. This process is influenced by the surface of the NPs which can be additionally functionalized by attaching apposite binding agents to enhance selectivity toward the target and ensure safer treatments by minimizing damages and side effects to healthy tissue.

However, the efficiency observed in clinical trials is not yet optimal. Major limitations arise from the low SAR values achievable with iron oxide nanoparticles (generally ranging from a few units to several hundreds of Wg^{-1}), from low tumor-targeting selectivity, and from difficulty in controlling the temperature reached in the treated area. Moreover, from the biological point of view, the internalization of a particle within the cellular environment can inhibit the Brownian relaxation mechanism, resulting in a reduction of heat dissipation [23].

4.3 A new biomedical frontier: Au-Fe nanoparticles

Over time, new approaches have been proposed to manage challenging diseases, such as cancer, or to improve the sensitivity of existing techniques for early diagnosis or tumor therapy. However, these procedures may require the administration of contrast agents to improve image contrast and selectivity, or the use of therapeutic agents that have intrinsic toxicity and may induce side effects in the healthy tissues [30].

In recent years, hybrid nanostructures combining iron oxide with noble metals, such as gold and silver, have been developed to further expand the biomedical potential and applicability of MNPs, since the two metals have shown biocompatibility, low reactivity and chemical stability when incorporated as NP shells or NP hetero-structures [31].

4.3.1 Physicochemical properties of gold nanoparticles

Gold is a multifunctional material recognized for its antioxidant, anticorrosive and bacteriostatic properties, making it highly synergistic if coupled with nanosystems [31]; what makes this metal so special is its physical properties: first of all, it is a good X-Ray attenuation material due to its high atomic number (Z = 79) (biological tissues are constituted mainly by carbon (Z = 12), oxygen (Z = 8) and hydrogen (Z = 1)), making it suitable for CT contrast agents. Furthermore, it possesses unique **local surface plasmon resonance** (LSPR), an optical phenomenon occurring when incident light encounters the surface electrons in the conduction band, which makes them oscillating and subsequently re-emitting light with a different wavelength [32]. Both scattering and absorption of light strongly depend on the dimensions and morphology of the Au nanoparticle, allowing a plasmon bandwidth modulation according to its diameter and shape.

Au NPs, thanks to their tunable surface plasmon resonance, can absorb light in a wide range of photon wavelengths, *i.e.*, [600-1300] nm, often referred to as **near-infrared region** (NIR). In Figure 6.1 (a), the absorption spectra of spherical gold nanoparticles with different diameters are shown. As the dimension increases from 9 to 99 nm, the plasmon resonance peak undergoes a red-shift from nearly 520 nm to 580 nm, along with a broadening of the absorption curve. Figure 6.1 (b), instead, illustrates how the LSPR response can be tuned across the visible and, most

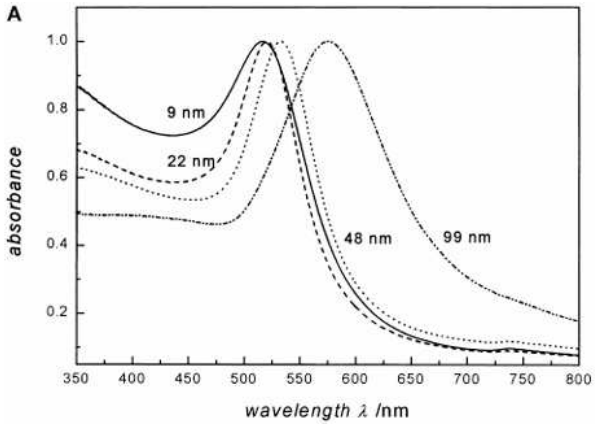

(a) *Absorption spectra of a gold NP in water, normalized by each respective absorption maximum.*

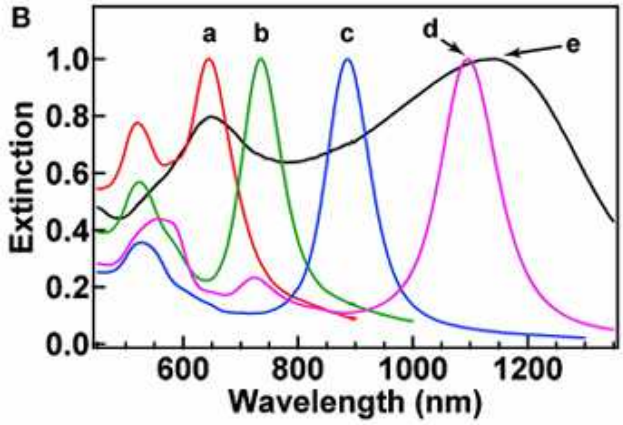

(b) *Normalized extinction spectra of gold nanostructures. a-d spectra represent nanobipyramid shaped particles while e-spectrum nanobranches shaped particles.*

Figure 4.4: *(A) Absorption and (B) extinction spectra of Au NPs [32].*

importantly, NIR regions by varying the morphology of gold nanoparticles and their dimensions [32]. The near-infrared region has a noticeable interest in the biomedical field: photons with that wavelength λ are "transparent" to normal tissues and once absorbed by gold nanoparticles, through light-to-heat transduction can be used to locally increase the temperature, inducing cell-deactivation mechanisms such as apoptosis or necrosis.

This process, called **photo-thermal therapy** (PTT) or even **photo-thermal ablation**, is a valid alternative to MFH, since light can be easily regulated, focused and remotely controlled, allowing a much more precise targeting therapy. Nevertheless, the main limitation of such treatments remains the insufficient penetration ability of laser or visible light in tissues, making them less suitable for targeting deep-seated tumors [32] [30].

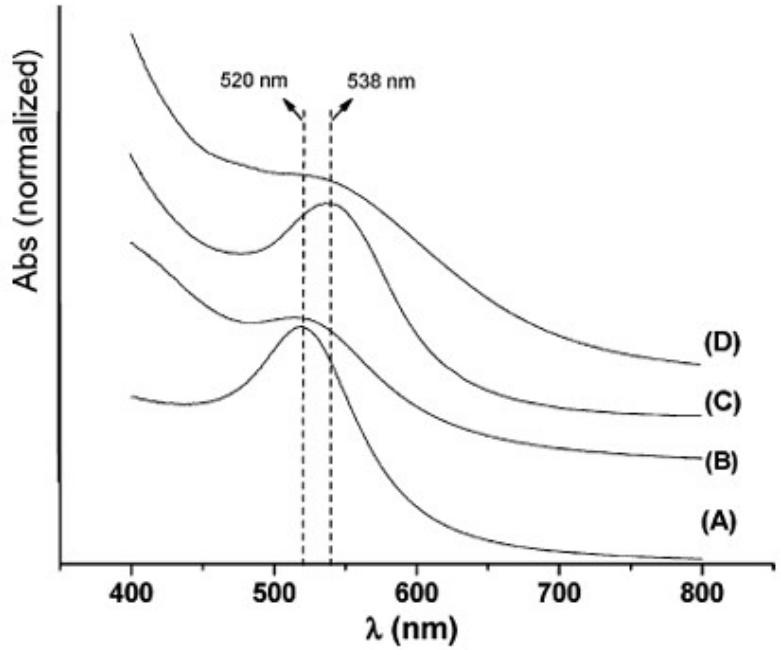

Figure 4.5: *Absorption spectra of UV light by Au and Au-Fe_3O_4 nanoparticles with different diameters, showing a red shift from 520 nm to 538 nm of (a) 8 nm Au to (c) 7-14 nm Au-Fe_3O_4 [33].*

4.3.2 Au-Fe combination advantages and properties

Ideal nanocomposites that can be used for both diagnostic and therapeutic applications, thus exhibiting **theranostic** properties, are one of the main research topics in the biomedical field. Advances in nanotechnologies paved the way for innovative, dynamic and multifunctional systems that can be exploited for both diagnostic and therapeutic purposes through the coupling of iron and gold. These hybrid nanoparticles, also called **multicomponent nanoparticles** (MCNP), take advantage of the synergy of iron's magnetic responsiveness and gold's plasmonic and chemical stability through the combination of them into a unique structure with different shapes and sizes: core-shell, dumbbell, flower and urchins-like are only a few of the possible configurations that can be found in literature [26].

The advantages of these systems are:

- Enhanced optical and magnetic properties compared to their individual single-component materials, since the presence of both iron oxide and gold amplifies their respective capabilities;
- Red shift of the surface plasmon resonance, which consists in the absorption of photons with a greater wavelength than the absorption of gold alone, as it is shown in Figure 4.5 for Au-Fe_3O_4 nanoparticles with different diameters;

- Multi-modal imaging, which involves the administration of a single type of CA that is suitable for different diagnostic exams, such as MRI or CT. Two different diagnostic images of the same area can be taken, leading to the extrapolation of complementary information. This is not possible when mono-modal CAs are used, resulting in a drastic reduction in the total dose delivered to the patient and an increased likelihood of side effects [30] [34].
- Adaptability for different cancer therapies, such as MFH, due to the superparamagnetic behavior of iron oxides, and PTT, due to the light-to-heat conversion ability of gold when irradiated with NIR photons.
- Biosensor capabilities, meaning that it can detect specific molecules, like DNA strands, proteins, and antibodies, in biological samples and separate them by applying an external magnetic field to these systems. This is achievable by combining a magnetic component (Fe_3O_4) with a plasmonic one (Au). The Fe_3O_4 domain enables rapid and efficient magnetic separation of biomolecules from complex media, while the Au domain provides a robust platform for functionalization with thiol-containing ligands, antibodies, or aptamers, allowing for selective recognition of specific targets [35].

In this thesis work, two prototypes of Au-Fe_3O_4 nanoparticles, known as **dumbbell**-like and **urchin**-like NPs, were studied. These two configurations provide two types of compounds composed of a magnetite nanoparticle and additional gold, differing in the amount of gold and in the resulting shape.

Dumbbell-shaped Au-Fe_3O_4 nanoparticles consist of two different NPs attached, forming a junction at their surfaces. This junction is responsible for the changes in the particle behavior, as it permits electronic communication between the two parts. Its final shape rather recalls a ”snowman-like” form, as it can be imagined as two spheres placed one on top of the other (see Figure 4.6) [26]. This particular structure offers two functional surfaces for attaching different types of molecules. For this reason, dumbbell-like NPs are considered a promising multifunctional probe for both diagnostic and therapeutic applications, as they exploit the plasmonic and superparamagnetic properties of gold and magnetite, respectively. Other important advantages come from their easily tunable size (size control up to 20 nm for each particle), and from the possibility of converting the core from Au-Fe_3O_4 to Au-Fe_2O_3 or Au-Fe, enabling a wide range of optical, magnetic and chemical properties [33].

The other hybrids are the spiky sea-urchins Au-Fe_3O_4 NPs, often referred to as nano-urchins (NU); these multipod gold nanostructures have attracted increasing attention due to their anisotropic morphology and high surface-to-volume ratio, being characterized by gold spikes on their surface. The latter displays ”hot-spots” on the particle border and an enhanced electromagnetic region that can be used to tune the surface plasmonic resonance to NIR region

to be suitable for the detection of biological tissues (as previously discussed) [27].

When a photon beam interacts with the molecules of a sample, two scattering mechanisms occur: elastic scattering or Rayleigh scattering, where the photon direction is deviated without any energy loss, or anelastic scattering, where a part of the energy is given to the molecular vibrations or vice versa. The scattered radiation can be detected as a characteristic signal emitted by the sample and takes the name of **Raman signal** [36]; its amplitude is rather low due to the small cross-section of the interaction, making it difficult to capture. However, the local surface plasmon resonance, drastically enhances the local electric field near the metallic nanoparticle by up to 100-1000 times, thereby increasing the Raman signal cross section by a factor 10^6-10^{10}. This process, called **surface-enhanced Raman scattering** (SERS), is a powerful non-destructive spectroscopy technique that enables ultrasensitive detection down to the single-molecule level, making it a valuable tool for biosensing and molecular diagnostics [37] [38].

Additionally, in the biomedical field, urchin-like NPs promote efficient light-to-heat conversion thanks to their irregular surface, making them suitable candidates for combined magnetic hyperthermia and photothermal therapy.

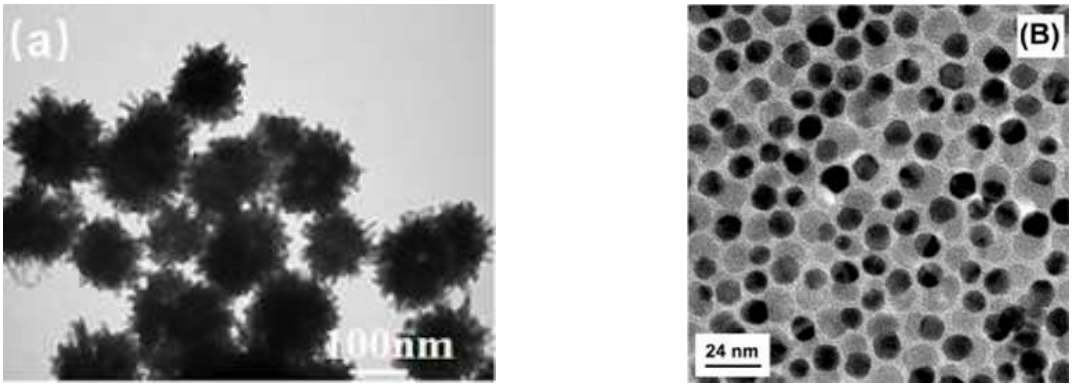

(a) *Sea-urchin-like gold NP[27].* **(b)** *Au-Fe_3O_4 dumbbell-like NP[33].*

Figure 4.6: *TEM images of sea-urchin-like gold nanoparticles and dumbbell-like Au–Fe_3O_4 nanoparticles.*

CHAPTER 5

INSTRUMENTS, MATERIALS AND METHODS

This chapter describes the instrumentation and methodologies employed, as well as the synthesis procedures and characterization of the four samples investigated in this thesis. The experimental work was conducted using two NMR spectrometers, operating respectively in the [7.2–63.864] MHz and [0.01–7.2] MHz frequency ranges, and a SQUID magnetometer for magnetic characterization.

Two kinds of nanoparticles will be presented and analyzed: dumbbell-like (DB) and nano-urchin-like (NU) structures. The magnetic and relaxometric studies of the first type of particles were conducted in aqueous and agarose-gel media, while the second type of particles was studied in agarose-gel.

5.1 Samples description

The samples studied in this thesis work were synthesized and produced by a research group of the Chemistry Department 'Ugo Schiff' & INSTM of the University of Florence (Sesto Fiorentino, Italy).

A set of two different specimens of nanoparticles were investigated in this work, all of them in the form of dimers constituted by a core of magnetite (Fe_3O_4), with an average diameter of 11.6 nm, and a gold (Au) component coupled to the magnetic core (as described in the previous chapter), in the form of dumbbell-like or urchins-like (that we will refer to as nano-urchins or "NUs") nano-heterostructures. Each sample possesses a coating, being, respectively, CTAB ((1-hexadecyl)trimethylammonium bromide) for the dumbbells and PEG (thiol-terminated polyethylene glycol) for the nano-urchins. The morpho-structural characterization was carried out on powder or water dispersions, while the magnetic and relaxometric studies were done on

the following water or agarose-gel dispersions:

- one sample of dumbbell-like Au-Fe_3O_4@CTAB NPs dispersed in water with an iron ion concentration of 0.1 mM (**DB_0.1_mM_H_2O**);
- two samples of dumbbell-like Au-Fe_3O_4@CTAB NPs dispersed in 1 wt% agarose gel with iron ion concentrations of 0.1 and 0.2 mM (**DB_0.1_mM_Agar** and **DB_0.2_mM_Agar**);
- one sample of nano-urchin-like Au-Fe_3O_4@PEG NPs embedded in 1 wt% agarose gel with an iron ion concentration below 0.1 mM (**NU_0.1_mM_Agar**).

The agarose-gel is a material formed from agarose, a linear polysaccharide extracted from a red algae called Rhodophyceae, dissolved in hot water and then cooled; it spontaneously forms a three-dimensional network thanks to hydrogen bonds, trapping large amounts of water inside it and becoming a gel-like solid. It finds relevant applications in the biomedical field due to its composition, able to mimic the behavior of tissues for in-vitro studies. Additionally, it has been shown that the tumor extracellular space convection/diffusion properties are similar to the agarose gel, making it suitable for drug delivery studies [39] [40].

5.1.1 Synthesis of naoparticles

The synthesis of the studied nanosystems is divided into three steps: gold seeds preparation, dumbbell-like particles formation, and nanurchines production.

Synthesis of gold nanoparticles

The gold nanoparticles were obtained through the reduction of $HAuCl_4 \cdot 3H_2O$ with morpholine–borane complex (MBC) at room temperature. Specifically, gold(III) chloride trihydrate (200 mg) and oleylamine (70%) (20 mL) were dissolved in 20 mL of heptane at 15 *C* under a nitrogen atmosphere. After 10 minutes of magnetic stirring, a solution of MBC (33.8 mg) previously dissolved in a mixture of oleylamine (70%) (1 mL) and heptane (1 mL) was rapidly injected, and the reaction was allowed to proceed for one hour under magnetic stirring at room temperature.

Synthesis of $AuFe_3O_4$ dumbbell-like nanoparticles

Au–Fe_3O_4 dumbbell-like nanoparticles were subsequently synthesized as follows: a mixture of oleic acid (1.695 g, 6 mmol) and oleylamine (90%) (1.59 g, 6 mmol) in 20 mL of 1-octadecene was heated to 140 °C at a rate of 5 °C /min under N_2 flow and maintained at this temperature for 20 minutes. Gold nanoparticles (20 mg dispersed in 2 mL of hexane) were then introduced into the solution and, after 5 minutes, 50 µL of iron(0) pentacarbonyl ($Fe(CO)_5$) was added. The

mixture was further heated to 280 °C at 2.33 °C/min and held at this temperature for 45 minutes. Finally, the system was cooled to room temperature and exposed to air in order to induce the oxidation of iron.

Synthesis of nano-urchin-like nanoparticles

For the synthesis of the NU sample, a seed-mediated growth approach was employed: it begins with the formation of Au NPs, serving as the seeds for Au-Fe_3O_4 nano-dumbbells that, in turn, act as seeds for the growth of highly anisotropic Au-Fe_3O_4 NUs.

Initially, the nano-dumbbells (approximately 2 mg in 1 mL of toluene) were subjected to three washing cycles with ethanol and ammonium hydroxide (NH_4OH) in order to remove oleylamine residues from their surface. The particles were then redispersed in 5 mL of deionised (MilliQ) water and to promote their dispersion in the aqueous medium, a small amount of (1-hexadecyl)trimethylammonium bromide (CTAB, 98%) (153 mg) was added and the solution was sonicated for 30 minutes. The growth solution was prepared by mixing 2.5 mL of 0.01 M $HAuCl_4 \cdot 3H_2O$ with 45 mL of 0.10 M CTAB, followed by the addition of 500 µL of a 0.01 M $AgNO_3$ solution and gentle mixing. Subsequently, 375 µL of 0.10 M ascorbic acid was introduced. Finally, 50 µL of the seed solution was added, mixed gently for 10 s, and left to react undisturbed for 20 minutes. Upon seed addition, the solution turned turquoise blue, suggesting the anisometric growth of the gold phase.

The resulting Au–Fe_3O_4 nano-urchins were functionalized with thiol-terminated polyethylene glycol (HS-PEG5000-COOH and MeO-PEG5000-SH) to improve colloidal stability and ensure biocompatibility of the nano-heterostructures. To this end, 2 mg of MeO-PEG5000-SH and 2 mg of HS-PEG5000-COOH were added to a freshly prepared aqueous solution of Au–Fe_3O_4 NUs, allowed to react for 5 minutes, and centrifuged at 11,000 rpm for 10 minutes. The pellet was washed and centrifuged three additional times, each time in the presence of 2 mg of MeO-PEG5000-SH and 2 mg of HS-PEG5000-COOH, to completely eliminate CTAB while preserving the stability of Au–Fe_3O_4 NUs against precipitation. In the final step, the NUs were rinsed with water to remove any excess PEG and redispersed in 5 mL of MilliQ water.

The agarose gel was produced by mixing water and agar in proportions to obtain a mixture of 1% agar concentration with respect to the total weight. The mixture, then, has been heated to 100°C and the NPs were added to it. As it cooled, reaching room temperature, the mixture solidified and a gel-like compound was reached.

5.1.2 Morpho-dimensional characterization

The samples have been analyzed to get the necessary information about their internal structure and dimensions through the use of three different measurement techniques: **transmission electron**

microscope (TEM), **X-Ray diffraction** (XRD) and **dynamic light scattering** (DLS).

Transmission electron microscope (TEM) is a high-resolution imaging technique based on the use of an external beam of accelerated electrons to probe thin samples (even below 100 nm). The electron beam, transmitted to the target, interacts with it through elastic or anelastic scattering or absorption processes. The contrast generated allows for getting information about the morphology of the material. In our case, it was used to estimate the dimensions of the magnetic core and of the gold component in dumbbell-like particles and NUs; moreover, the shape of the particles was observed through TEM acquisitions. From this procedure, it is not possible, however, to secure any information about organic coatings of the magnetic target [41].

The X-Ray diffraction (XRD) measurement is a non-destructive analytical technique that permits the investigation of the structural properties of a crystalline material. It is based on the elastic scattering interactions between the X-ray beams and the periodic atomic planes of the target crystal, producing characteristic diffraction patterns that can be studied through Bragg's law:

$$n\lambda = 2d \sin\theta \tag{5.1}$$

with n a positive integer that defines the order of the diffraction, λ is the wavelength of the incident radiation, d is the distance between the reticular planes and θ is the angle created by the incident radiation and the reticular planes. From these patterns, it is possible to obtain information about the crystalline size and the degree of crystallinity of the target, as well as its lattice parameters [42].

The dynamic light scattering (DLS) is a technique used to investigate the hydrodynamic size distribution of particles suspended in a liquid medium. It is based on the analysis of the fluctuations in the intensity of the scattered light, produced by the Brownian motion of the target particles. This procedure is extremely useful for characterizing nanoparticles, colloids and molecules in a solution, providing non-destructive and rapid measurements of their size and polydispersivity [43].

5.1.3 Magnetic characterization

The magnetic characterization has been conducted by using a SQUID (Superconducting Quantum Interference Device) magnetometer (Quantum Design MPMS, San Diego, CA, USA) located in the physics department of the University of Pavia. The SQUID is one of the five modules of Quantum Design's Magnetic Property Measurement System (MPMS) magnetometer, a highly integrated system designed for the study of magnetism in matter. It is divided in:

- **Temperature control system**, the module responsible for temperature changing in the range 2 K (-271 °C) to 400 K (27 °C)
- **Magnet control System**, the module responsible for setting the magnetic field in the range -7 to 7 Tesla
- **Superconducting SQUID amplifier system**, the module containing the rf SQUID detector that permits magnetic measurements of the sample
- **Sample handling system**, the module that permits to change the sample position without producing any undue mechanical vibration in the SQUID
- **Computer operating system**, the module responsible for checking the operating features of the MPMS, thanks to the computer control

The SQUID consists of a superconducting ring with a small insulating layer called **weak link** or Josephson junction. The flux that passes through the ring is quantized once the ring has become superconducting, but the weak link enables the flux trapped in the ring to change by discrete amounts (without it, no flux can enter in the ring). The device can therefore be used to measure the changes in flux quanta in the ring and in the external magnetic fields, even for values on the order of 10^{-15} T [1].

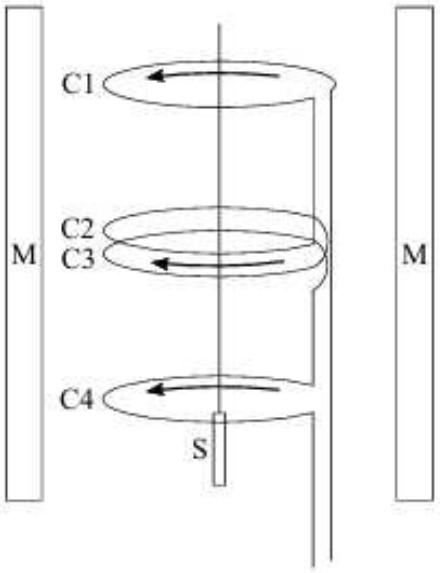

Figure 5.1: *Schematic representation of a SQUID magnetometer; C1, C2, C3, C4 are the pickup coils, M is the superconducting electromagnet and S is the sample to be inserted [44].*

The instrument was used to acquire the first magnetization curves of the magnetization (as a function of an external applied magnetic field H) and the ZFC/FC curves. The zero-field cooling/field-cooling (ZFC/FC) technique is an experimental method used to reconstruct the

magnetization curve of a sample as a function of temperature, either in the presence or absence of an external magnetic field. From the maximum of the ZFC curve, the blocking temperature can be estimated. This temperature corresponds to the point below which the superparamagnetic system becomes blocked along its easy axis and is unable to reorient, due to insufficient thermal energy to overcome the anisotropy energy barrier.

5.2 Instrumental apparatus for the NMR studies

The relaxometric studies were carried out in two laboratories using different NMR spectrometers. At the University of Pavia, an Apollo Tecmag spectrometer (Houston, TX, USA) equipped with a MAGNET B-E 25 electromagnet (Bruker, Billerica, MA, USA) was employed. At the University of Milan, a Spinmaster spectrometer (Stelar s.r.l., Mede, Italy) with a Bruker electromagnet was used. Both instruments were employed to analyze all four samples and to measure the T_1 and T_2 relaxation times over two different frequency ranges. In particular, the Milan setup operates at frequencies down to a few tens of kHz and provides sufficient sensitivity to acquire reliable signals from the samples that can be used to reconstruct the low region of an NMRD curve. The Pavia's setup was used to acquire the relaxation times of the investigated samples at frequencies greater than 7.2 MHz.

5.2.1 NMR spectrometer

The Apollo Tecmag NMR spectrometer was used to perform measurements of T_1 and T_2 in the frequency range [7.2 - 63.864] MHz. A scheme of the NMR setup is given in Figure 5.2.

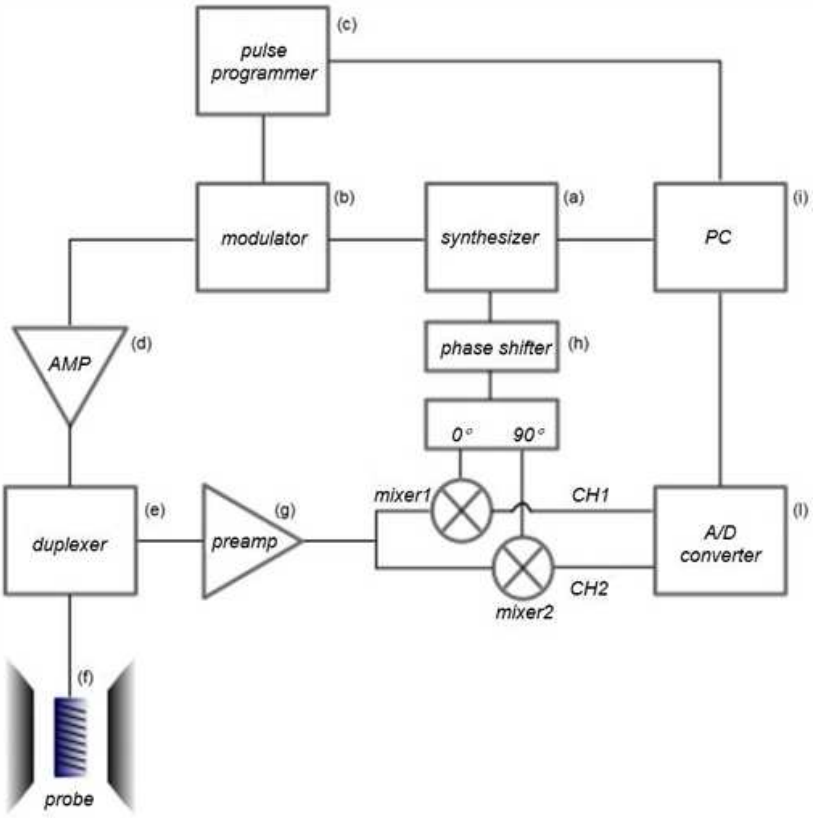

Figure 5.2: *Schematic representation of the components of the NMR spectrometer used to perform the T_1 and T_2 measurements in Pavia.*

The NMR setup encloses an electromagnet that generates the static magnetic field H_0, an amplifier, a pre-amplifier, a duplexer, and a coil (where the studied sample is placed), which is shielded from the electromagnetic noise.

The coil has a dual function: it transmits the radiofrequency pulse produced by the oscillating magnetic field H_1 to the sample and, conversely, collects the signal produced by the sample itself after it has been disturbed. Those sender-receiver modalities of the coil are controlled by the duplexer, a component of the spectrometer used to decouple the circuit into two blocks, transmission (TX) and reception (RX).

The frequency synthesizer, a quartz oscillating circuit, generates the desired ω_{rf} for the rf-pulse. Right after, a pulse generator called pulse programmer creates the excitation pulses to flip the nuclear magnetization, and a modulator permits to add an additional phase of 0, 90, 180 and 270 to the signal, to control its direction in the rotating frame Σ_{rot}. Those parts are controlled by the PC, which manages the timing of the pulses and the specific sequences to be used.

After that, an oscillating rf-signal, with a predetermined phase ψ, of the form:

$$S(t) \propto cos(\omega_{rf} t + \psi) \tag{5.2}$$

is generated and sent to the power amplifier (AMP), which increases its amplitude so that it can be detected by the duplexer and enter it.

As it can be seen in Figure 5.3, the coil's transmission line is an RLC circuit made by two capacitors and one inductance with their respective impedance; to maximize the signal reception and minimize its reflection, the three passive components need to be tuned and matched by varying their capacity, so that the condition:

$$\omega_{RLC} = \sqrt{\frac{1}{LC_{eq}}} = \omega_0 \tag{5.3}$$

is achieved, with C_{eq} the equivalent capacity of the two tunable capacitors, such that Z, the impedance of the coil, is equal to 50 Ω, a characteristic value for transmission circuits that provides the maximum power transfer.

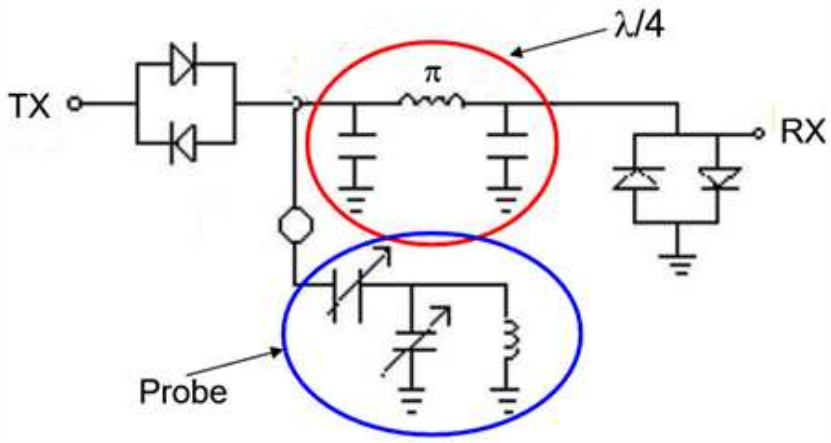

Figure 5.3: *Transmission and reception decoupling of the NMR spectrometer.*

When the probe receives the signal from the sample, it is then passed back through the transmission line and needs to be passed to the RX part of the circuit. The duplexer is the one responsible for that: it passes the signal directly to the pre-amplifier, a component used to receive signals with amplitudes in the order of mV, after the sample has produced it. The $\lambda/4$ bridge, consisting of two capacitors and an inductor, protects the pre-amp from signals that are too large, such as those coming from the synthesizer, allowing only low-intensity signals from the probe to pass through. Also in this case, an impedance matching has to be achieved by setting the total impedance of the line to 50 Ω.

After the pre-amp has received the signal, it amplifies it beyond the 0.6 V of conductive potential that characterizes the diodes of the receiving line, so that they can start conducting and

pass forward the new amplified electric signal, which now has the form of:

$$S(t) \propto M_0 e^{-t/T_2} cos(\omega_0 t + \alpha) \tag{5.4}$$

onto the Mixer1 and Mixer2 channels. These two channels separate the signal in two different signals, corresponding to the real part and the imaginary part of it, and mix it with two upcoming signals from the synthesizer and phase shifter with the chosen frequency ω_{rf} and a corresponding phase of 0° and 90°.
If the resonance condition is achieved, so that $\omega_0 = \omega_{rf}$, the resulting form of S(t) is given by:

$$S_1(t) = M_0 e^{-t/T_2} cos(\phi) \tag{5.5}$$

and

$$S_2(t) = M_0 e^{-t/T_2} sin(\phi) \tag{5.6}$$

Those two are then digitized thanks to an A/D converter and processed by the PC.

5.2.2 FFC spectrometer

The Stelar SMARtracer spectrometer (NMR laboratory, Physics Department, Milan) was used to perform T_1 and T_2 measurements of the samples in the frequency range [0.01 - 9] MHz using the Fast Field Cicling (FFC) technique (see Chapter 3 for details).
The electromagnet, shown in Figure 5.4, is highly homogeneous and rapidly switches the intensity of the static magnetic field, and allows for the acquisition of the signal from the sample even at frequencies of the order of 10 kHz.

Figure 5.4: *SMARtracer Relaxometer (Stelar s.r.l, Mede, Italy) used for the low-frequency measurements in Milan.*

The samples were studied in two different frequency ranges, depending on which modality

the system was asked to operate in order to perform the measurement:

- **Non-polarized** acquisition: [3.7-9] MHz
- **Pre-polarized** acquisition: [0.01-3.7] MHz

5.2.3 Relaxometric measurements

The nuclear relaxation times depend on the concentration of magnetic centers in the solution. When this concentration is too high, T_1 and T_2 become excessively short, making their measurement impossible due to the limited sensitivity of the instruments employed. Thus, the nanoparticle samples under investigation were diluted to very low concentrations, specifically of 0.1 and 0.2 mM, to relaxation times compatible with the sensitivity of the measuring system.
Each acquisition with the Pavia's spectrometer, in the high frequency range of [7.2 - 63.864] MHz, were conducted by setting the appropriate Larmor frequency of each sample and by performing the tuning and matching of the probe through the wobbling generator. The signal acquisition was performed through the use of the *NTNMR* software, which allows to select the optimal sequences parameters. The *QtNMR* software has been subsequently used to generate an output file for external data elaboration. The latter operation was finalized with the *Origin* software, which allows to perform scatter plots and curve fits.

To determine the T_1 relaxation time, a saturation recovery spin-echo (SRSE) sequence was used to study the recovery of the magnetization M_z as a function of time, optimized for each sample by setting each characteristic parameter on the NTNMR software, such as the repetition time *Rept*, the saturation pulse duration $\pi/2_{sat}$ and the recovery time τ_{rec}.
With Origin, the magnetization curve was analyzed by modifying the Bloch's equation:

$$M_z(t) = M_0(1 - e^{-t/T_1}) \tag{5.7}$$

into

$$e^{-t/T_1} = 1 - \frac{M_z(t)}{M_0} \tag{5.8}$$

where M_0 is the maximum value achieved by the magnetization following the recovery. After that, a mono-exponential fit $y = A + Be^{-t/T_1}$ (with A = 0 and B = 1) was set to extract T_1.

For T_2, a CPMG sequence was adopted to evaluate it and check eventual diffusion contribution on the transverse relaxation time. As for the T_1 measurement, each sample was checked with an FID signal before any acquisition, to be sure that the resonance condition was fulfilled. Any fundamental parameter, like the number of π pulses to refocus the magnetization in the x'-y' plane and the echo time τ_{echo}, was optimized to properly acquire each point of the curve. The sequence was then reconstructed through the height of each echo point produced throughout the

acquisition time, following the relation:

$$M_{xy} = M_0 e^{-t/T_2} \tag{5.9}$$

The latter was then analyzed with a mono-exponential fit (as in the case of the SRSE sequence) to determine T_2.

For the low frequency region [0.01 - 7.2] MHz, corresponding to the one studied with the FFC spectrometer in Milan laboratories, the determination of the characteristic relaxation times was performed using a saturation recovery spin-echo sequence (SRSE) for T_1 and, respectively, a CPMG and a spin-echo (SE) sequence for the non-polarized and pre-polarized acquisitions of T_2.

The calculated T_1 and T_2 values were then used to derive the relaxivity r_i by dividing the corresponding relaxation rate R_i for the concentration C of each sample:

$$r_i = \frac{1}{C}(R_{i,obs} - R_{i,diamag}) = \frac{1}{C}(\frac{1}{T_{i,obs}} - \frac{1}{T_{i,diamag}}) \tag{5.10}$$

with i = 1,2, respectively, the longitudinal and transversal relaxivity and $T_{i,obs}$ the relaxation time of the diamagnetic component of the sample, referred to the aqueous or agarose-gel environment in which the MNPs are dispersed.

CHAPTER 6

RESULTS AND DISCUSSION

In this chapter, the results from the morpho-dimensional and magnetic characterization are presented and discussed, followed by the analysis of Nuclear Magnetic Resonance Dispersion profiles and their fit performed with the Roch-Müller-Gillis model to estimate the parameters of interest for each sample.

6.1 Morpho-dimensional characterization of the samples

As mentioned in Chapter 5, each sample of this thesis work has been studied by performing TEM, XRD, DLS and SQUID measurements to determine their physical, morphological and magnetic properties.
The morpho-dimensional analysis was carried out by a research group from the Department of Chemistry at the University of Florence (Italy), the same group that synthesized the particles investigated in this thesis project.

6.1.1 TEM analysis and results

TEM analysis was performed using a TALOS F200X G2, Thermo-Fisher Scientific, equipped with a high-brightness Field Emission Gun (X-FEG, 80–200 keV), to determine the morphology and size distribution of the MNPs. The mean diameter and size distribution of each sample were obtained by statistical analysis over more than 100 NPs, using ImageJ software. A log-normal fit of the histograms of the two component distributions was performed to evaluate their mean diameter and standard deviation from the relations:

$$\mu = R_0 e^{\sigma^2/2} \tag{6.1}$$

and

$$\sigma_\mu = R_0 \sqrt{e^{\sigma^2} \cdot (e^{\sigma^2} - 1)} \tag{6.2}$$

TEM images of the two classes of nanoparticles and the relative dimensional analysis are shown(Figure 6.1). The Au NPs appear black in the image, while the iron oxide NPs appear light-colored, as expected by gold which possesses an higher electron density than Fe_3O_4.

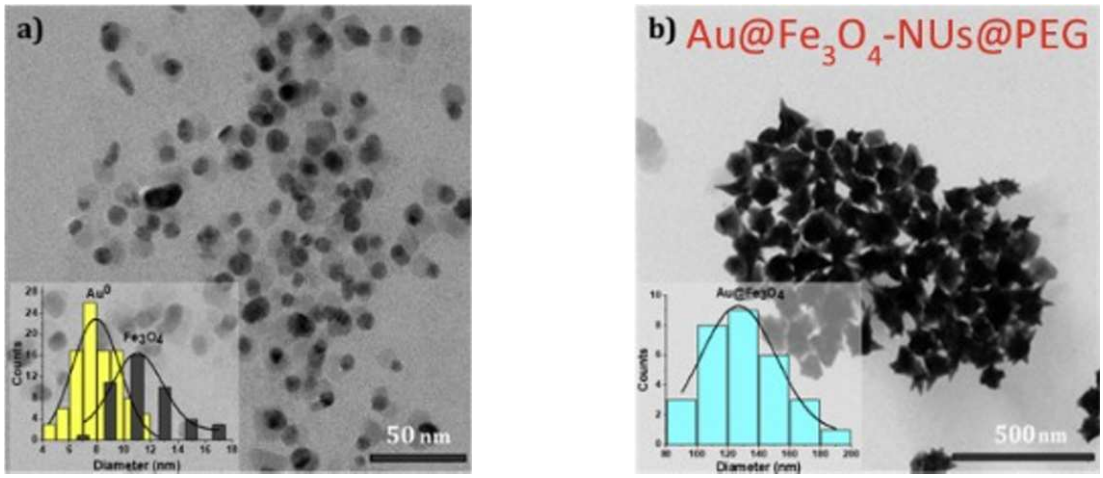

(a) *Dumbbell (DB) nanoparticles.* **(b)** *Nano-urchin (NU) nanoparticles.*

Figure 6.1: *TEM images and dimensional analysis of Au–Fe_3O_4@CTAB dumbbell nanoparticles (a) and Au–Fe_3O_4@PEG nano-urchin nanoparticles (b).*

The dimensions of the magnetite and gold components of dumbbell-like nanoparticles, as well as the overall size of the Au–Fe_3O_4@PEG nano-urchin-like nanoparticles, were evaluated. The magnetic component, common to both samples, exhibited an average diameter of 8.2 ± 1.8 nm. The gold domain in the dumbbell NPs measured 11.6 ± 2.4 nm, while the overall size of the NUs was 131.7 ± 26.4 nm (see Table 6.2).

Table 6.1: *Dimensions of gold and magnetite domains in the two classes of nanoparticles.*

Sample type	Magnetite diameter (nm)	Gold diameter (nm)
Dumbbell (DB)	11.6 ± 2.4	8.2 ± 1.8
Nano-urchin (NU)	11.6 ± 2.4	132 ± 26

6.1.2 XRD analysis and results

Powder X-Ray diffraction (PXRD) data were recorded using an Anton Paar XRDynamic 500 diffractometer equipped with a Co Kα (1.7928 Å) radiation source and operating in $\theta - \theta$ Bragg-

Brentano geometry at 40 kV and 40 mA. The measurements were carried out in the range 25°–70°, with a step size of 0.03° and a collection time of 1 s. The lattice parameters *a* was evaluated with TOPAS® software (Bruker) using the Fundamental Parameter Approach method considering a cubic space group Fd-3m.
In Figure 6.2, the XRD pattern of the dumbbell particles is shown, while data of nano-urchines are not available.

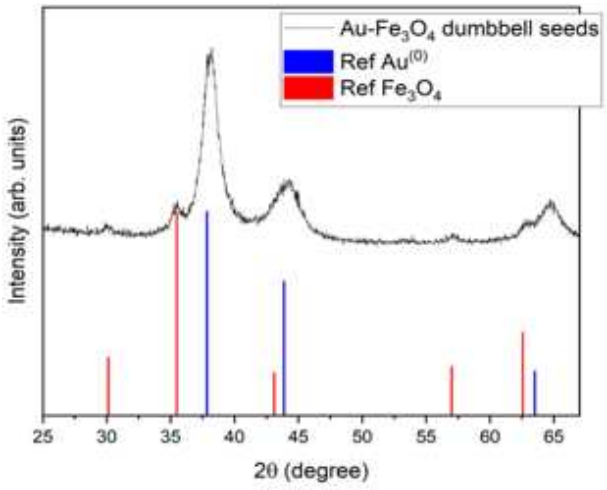

Figure 6.2: *XRD pattern of Au-Fe_3O_4 nano-dumbbells (black line) and reference patterns of magnetite (red bars) and gold (blue bars).*

The XRD pattern of the Au-Fe_3O_4 nano-dumbbells shows the presence of two different crystalline phases, compatible with the spinel cubic structure characteristic of magnetite (red bars) and with the face-centered cubic (fcc) structure of gold (blue bars). All the peaks match for position and intensity those of the reference patterns (JCPDS 19-0629 for magnetite; JCPDS 04-0784 for gold). No impurity peaks corresponding to other iron oxide phases can be recognized in the pattern.
The resulting lattice parameters (a = 8.399 Å) and (a = 4.087 Å) are close to those expected for magnetite (8.396 Å) and gold (4.078 Å), respectively, which confirms that the sample consists of Au-Fe_3O_4 nano-dumbbells.

6.1.3 DLS analysis and results

For the *Dynamic Light Scattering* (DLS) measurements, the average hydrodynamic size of Au-Fe_3O_4 NUs was analyzed using the NanoSight NS300 system (Malvern Panalytical); this technique consists of the use of an external incident beam that interferes with the Brownian motion of the nanoparticles while suspended in the medium and, through their diffusion coefficient and size, it is possible to determine their hydrodynamic diameter. In Figure 6.3, the DLS size distribution of Au-Fe_3O_4 NUs is presented.

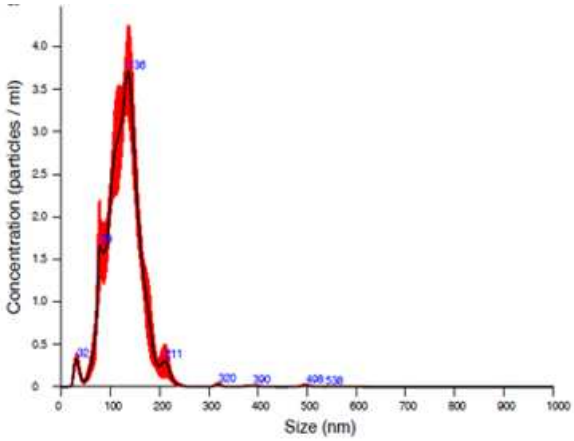

Figure 6.3: *Au-Fe_3O_4 NUs size distribution analysis obtained by dynamic light scattering.*

The NanoSight NS300 measurements revealed that Au-Fe_3O_4 NUs were well dispersed in water with an average hydrodynamic diameter of 130 ± 38 nm, which is in good agreement with d_{TEM} and confirms the successful PEG functionalization and the stability of the sample.

6.2 SQUID magnetic characterization: analysis and results

The magnetic characterization was performed using a SQUID magnetometer (Quantum Design). Both the **first magnetization** curves and the **zero-field-cooled/field-cooled** (ZFC/FC) curves were acquired for each sample (details of the acquisitions are listed in the following sections).

Sample Preparation for SQUID Measurements

The magnetic behavior of the studied nanoparticles has been investigated in a water dispersion and in three agarose gels dispersions in the case of DB particles, while the NUs were studied only in agarose gel. Regarding sample preparation:

- **Water dispersion**: 300 μL of nanoparticles (NPs) dispersed in water (DB_0.1_mM_ H_2O) were deposited onto a piece of paper. After air-drying, the paper containing the dried NPs was placed inside a SQUID capsule. However, due to the low concentration of the initial dispersion, the amount of deposited material was very small, below the sensitivity threshold of the balance used for weighing (analyzed sample: DB_0.1_mM_H_2O).
- **Agarose samples**: The hydrogels were collected and directly placed into the SQUID capsules. In this case, the unfilled spaces remained inside the capsules, preventing an accurate estimate of the actual sample volume (analyzed samples: DB_0.1_mM_Agar, DB_0.2_mM_Agar, NU_0.1_mM_Agar).

However, the determination of the absolute magnetization values was not possible due to large uncertainties in both the NPs mass and the agarose volume introduced inside the capsules. Therefore, magnetic data will be reported in arbitrary units. Although this prevents a direct quantitative comparison across different samples, the qualitative features of the curves still provide meaningful information on the magnetic behavior.

The first magnetization curves of the samples were reconstructed by varying the external magnetic field H from 0 T to 5 T (0 to +50000 Oe) at a temperature of 300 K. The results of the acquisitions are reported in Figure 6.4.

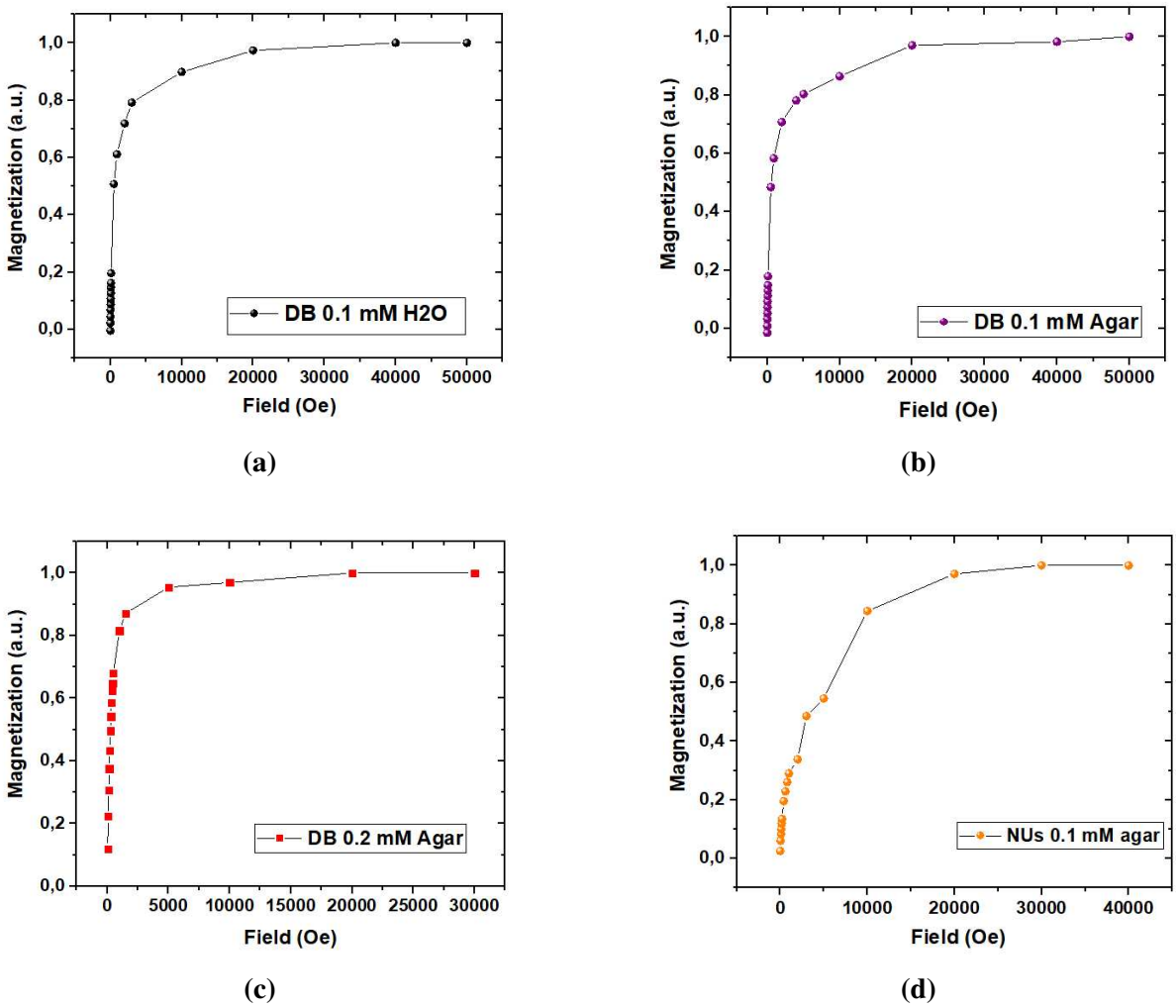

Figure 6.4: *First magnetization curves of the four samples (DB_0.1_mM_H_2O, DB_0.1_mM_Agar, DB_0.2_mM_Agar, NU_0.1_mM_Agar) acquired at T = 300 K.*

As previously mentioned, each first magnetization curve is reported in arbitrary units, as the conversion from emu to emu/g (Fe) was not feasible due to the large uncertainty in the determination of the iron concentration in each sample. As a result, no saturation magnetization

values could be estimated, and therefore, the discussion is limited to a qualitative comparison of the magnetization trends and to the coercive field H_C determination from the intersection of the hysteresis loop with the x-axis, which corresponds to the externally applied magnetic field needed to remove any remainance of magnetization.

The ZFC/FC measurements were carried out in the temperature range of 0-300 K under the application of small magnetic fields: 150 Oe for the DB 0.1 H_2O sample, 50 Oe for the DB 0.1 mM Agar sample, and 100 Oe for the NU 0.1 Agar sample. The ZFC/FC curve for the DB 0.2 mM Agar sample was not acquired, as it should be similar with that of the 0.1 mM Agar sample. The results are presented in Figure 6.5.

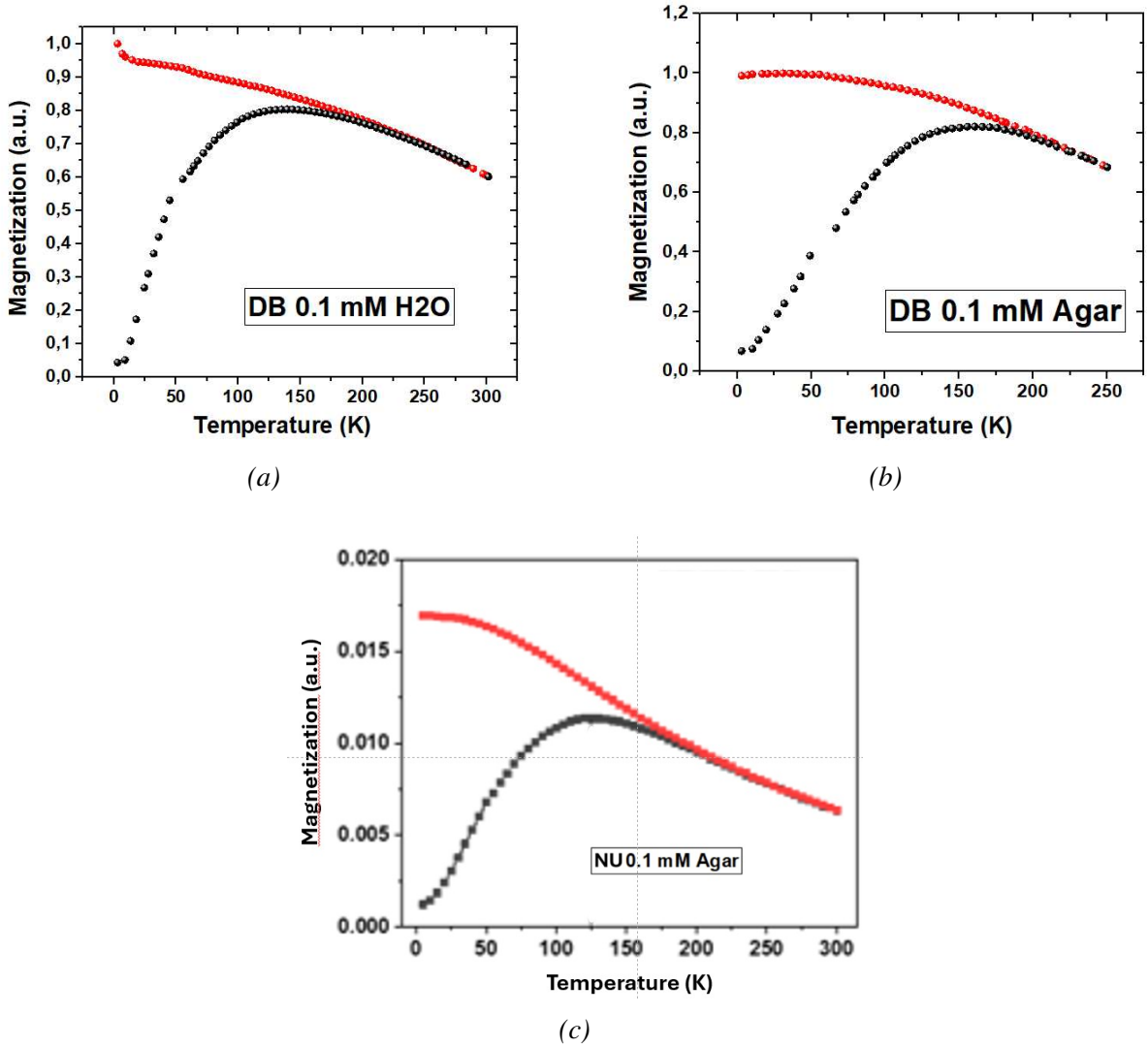

Figure 6.5: *ZFC/FC curves of DB_0.1_mM_H_2O (a), DB_0.1_mM_Agar (b), and NU_0.1_mM_Agar (c), acquired under a field of 150 Oe for the DB_0.1_mM_H_2O sample, 50 Oe for the DB_0.1_mM_Agar sample, and 100 Oe for the NU_0.1_mM_Agar sample.*

All the samples have shown characteristic features of superparamagnetic nanoparticles: a pronounced divergence between the ZFC/FC branches and a maximum in the ZFC curve corresponding to the blocking temperature value. The blocking temperature T_B for each sample can be estimated from the maximum, as it represents the temperature below which the system is no longer superparamagnetic and becomes magnetically blocked along the easy axis.

The dumbbells 0.1 mM H_2O and Agar ZFC/FC presented in Figure 6.5 (a) and (b) are the ones obtained from the Pavia's laboratory SQUID. The NUs ZFC/FC has been acquired by the Florence's research group. In Table 6.2 are listed the resulting blocking temperature and coercive fields.

Sample type	T_B **(K)**	H_C **(Oe)**
DB 0.1 mM H2O	144 ± 50	< 11
DB 0.1/0.2 mM Agar	161 ± 40	< 13
NU 0.1 mM Agar	125 ± 40	< 15

Table 6.2: *Blocking temperature T_B and coercive field H_C extracted from the ZFC/FC curves and first magnetization curves of each sample.*

For dumbbell samples, ZFC curves resulted in a broad distribution of magnetization around T_B values of 144 and 161 K, reflecting a certain polydispersion degree of the magnetic nanosystems. These values are in good agreement with those found in literature for magnetite nanoparticles of similar diameter (10-15 nm) For nanourcins agarose dispersion, the ZFC curve still indicates a superparamagnetic behavior of the nanoparticles, centered in T_B = 125 K, despite the enlarged hydrodynamic diameter (almost 131 nm) due to the gold envelopment.

Overall, the ZFC/FC curve measurements seem to confirm the superparamagnetic behavior of those nanoentities at room temperature. The similarity in their profile might reflect the fact that the Fe_3O_4 core is able to preserve its intrinsic magnetic properties even after the structural modification due to the larger and larger gold contribution and change of the dispersion medium.

6.3 NMR measurements and curve analysis

NMR measurements were carried out in two frequency ranges using two different NMR spectrometers, operating, respectively, in the [7.2–63.864] MHz and [0.01–9] MHz ranges (see Chapter 5 for more details).

The two species of NP (DB and NU) were synthesized by the research group at the University of Florence. For the preparation of NMR samples, the particles were dispersed in both water and agarose gel in the case of DB particles and only in agarose gel in the case of NUs, as surface modification with PEG could not stabilize in water ~130 nm particles for NMR studies. The

NMR samples were prepared at iron concentrations of 0.1 mM or 0.2 mM, to ensure that their relaxation times were within the measurable range of the low frequency instruments.

We will refer to NMR samples with the following labels that identify the type of nanoparticles (DB or NU), the iron concentration, and the dispersant medium:

- **DB_0.1_mM_H_2O**, to indicate the dispersion of dumbbell particles with a concentration of 0.1 mM of magnetic centers in water;
- **DB_0.1_mM_Agar**, to indicate the dispersion of dumbbell particles with a concentration of 0.1 mM of magnetic centers in agarose;
- **DB_0.2_mM_Agar**, to indicate the dispersion of dumbbell particles with a concentration of 0.2 mM of magnetic centers in agarose;
- **NU_0.1_mM_Agar**, to indicate the dispersion of nano-urchin particles with a concentration of 0.1 mM of magnetic centers in agarose.

In the following sections, the resulting longitudinal and transverse NMRD profiles evaluated from the relaxometric measurements are shown and discussed. The longitudinal profiles were subsequently fitted with the Roch-Müller-Gillis heuristic model, and its variations, to evaluate additional properties of the nanoparticles, studied in different environments (water and agarose gel).

6.3.1 Au-Fe_3O_4 dumbbell: aqueous *vs* agarose medium

The Au-Fe_3O_4 dumbbell particles have been studied in two different matrices: water and agarose-gel 1%w. In the agarose medium, two different iron concentrations were investigated (0.1 and 0.2 mM).

The two considered media were selected to investigate the Brownian relaxation contribution on the relaxation curves and possibly understand how it influences proton relaxation; in fact, agarose-gel might inhibit Brownian rotation and make the Néel contribution dominant. A similar rationale was applied to the variation in concentration, which plays an important role in the intrinsic behavior of the nanoparticles: an increase in the concentration of magnetic dipoles in the medium leads to stronger dipole-dipole magnetic interactions, an increase of the local magnetic field inhomogeneities and spin dephasing, thereby influencing their Néel's motion by accelerating their collective fluctuations. In addition, the probability of particle aggregation increases, leading to the formation of particles with a larger effective magnetic radius and different magnetic and relaxometric properties, even might reducing them.

In Figure 6.6 and Figure 6.7 the longitudinal r_1 and transverse r_2 relaxation profiles of the DB_0.1_mM_H_2O, DB_0.1_mM_Agar and DB_0.2_mM_Agar are shown. The error in r_i values

was estimated a priori to be 10% from uncertainties related to the selection of the acquisition parameters, the experimental instrumentation and its electronics, and the pulse sequences. The r_2 values are not reported for frequencies below 7.2 MHz due to the high fluctuations of the measured relaxation times that have been acquired with the FFC instruments. In fact, T_2 acquisitions are very sensitive to such conditions and to magnetic field inhomogeneities related to the SMARTracer setup at low frequencies. The r_2 profiles are therefore presented in the [7.2 - 63.864] MHz frequency range, corresponding to the data acquired with the NMR spectrometer in Pavia NMR laboratory.

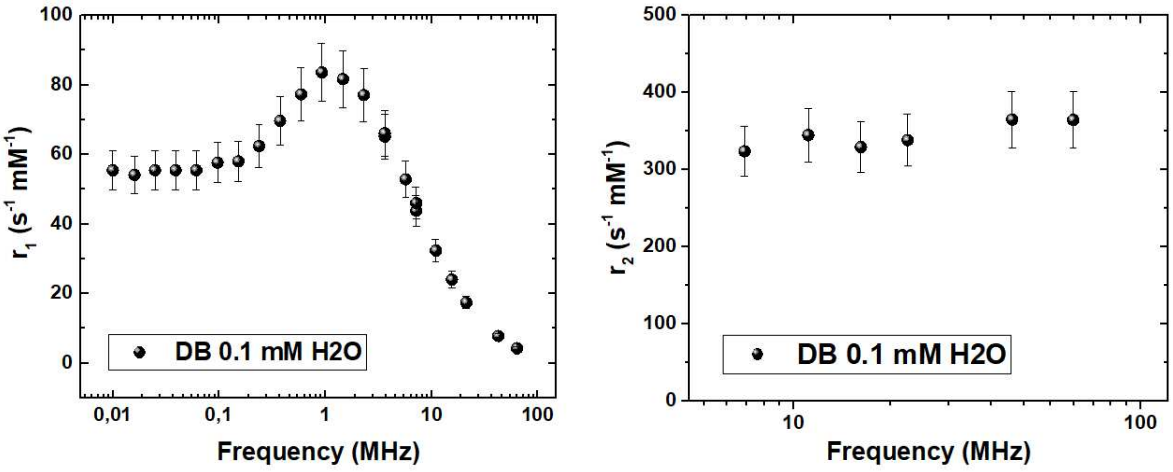

(a) *(b)*

Figure 6.6: *Longitudinal r_1 (a) and transverse r_2 (b) NMRD profiles of the DB_0.1_mM_H_2O, acquired at room temperature.*

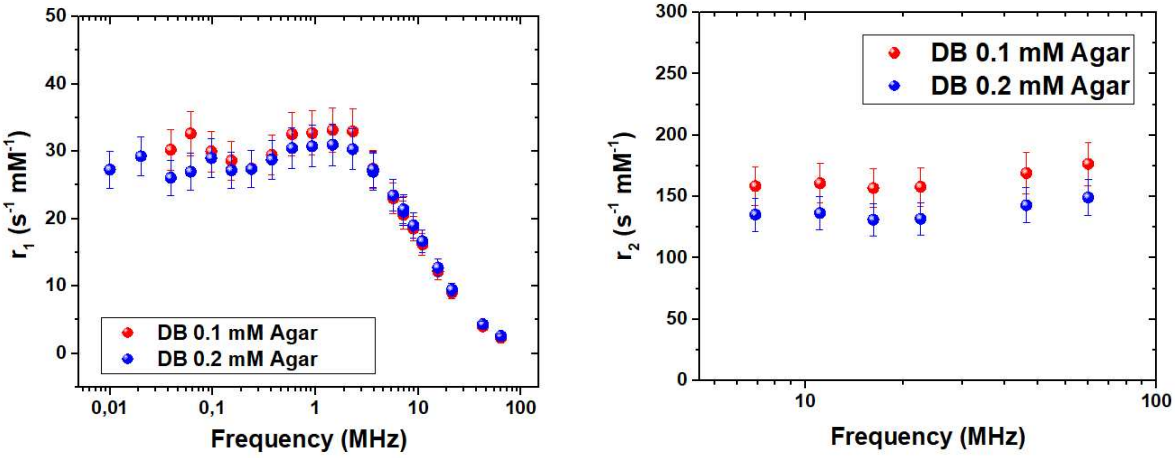

(a) *(b)*

Figure 6.7: *Longitudinal r_1 and transverse r_2 NMRD profiles of the DB_0.1_mM_Agar and DB_0.2_mM_Agar, acquired at room temperature.*

For the DB_0.1_mM_H_2O, the r_1 profile (shown in Figure 6.6) presents a plateau for low frequencies (0.01 - 0.1 MHz) in which the relaxivity remains constant around 55 $s^{-1}mM^{-1}$, before increasing and reaching the maximum value of 84 $s^{-1}mM^{-1}$ at 1 MHz. For higher frequencies, the curve rapidly decreases and the lower value of r_1 = 4.27 $s^{-1}mM^{-1}$ at 63.864 MHz is obtained. As discussed in Chapter 3, such behavior can be compared with a superparamagnetic SPIO NPs, described by a constant Freed spectral density function at low frequencies and no low-field dispersion, recognizable by the absence of a "well" in the plateau region before the relaxivity starts to increase to its maximum. Its absence is a distinctive feature of crystals with an high anisotropy energy, as in the case of dumbbell-like hetero-structures.

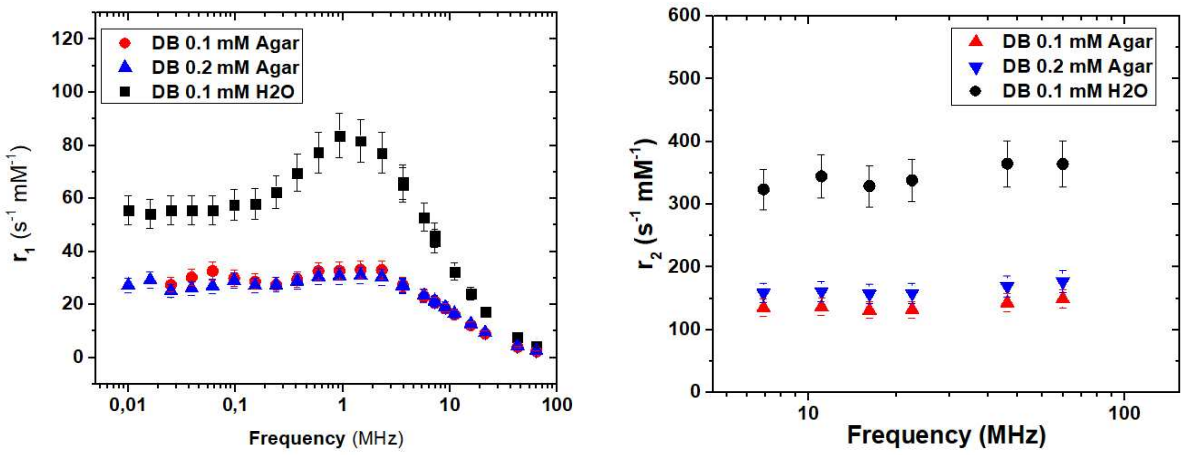

(a) *(b)*

Figure 6.8: *Longitudinal r_1 (a) and transverse r_2 (b) NMRD data of the three dumbbell solutions, shown as colored markers: black (DB_0.1_mM_H_2O), red (DB_0.1_mM_Agar), and blue (DB_0.2_mM_Agar).*

The same particles dispersed in agarose 1%w at concentrations of 0.1 and 0.2 mM (samples DB_0.1_mM_Agar and DB_0.2_mM_Agar, respectively) show longitudinal and transverse NMRD profiles that overlap within the experimental error, suggesting the linearity of the relaxivity as a function of the concentration, which does not appear to affect the relaxometric properties of the systems studied.

As shown in Figure 6.8, the same particles dispersed in agarose 1%w, show quite a different longitudinal frequency behavior from their aqueous counterpart. As for the maximum observed on the two curves, which is still present at 1 MHz frequency (as expected from particles with the same core and relative dimensions), it appears decreased (to nearly 30 $s^{-1}mM^{-1}$), flattened (there's not a single value that really stands out in that interval, making it approximately constant) and less pronounced if compared to the in-water case. This effect could be attributed to the presence of the agarose, which modifies the particle's Brownian rotational time but also the water dynamics, causing the reduction of the free-water fraction that is responsible for the relaxation

mechanisms with the magnetic core, the slowing down of water exchange with the hydration shell and, most importantly, the particle diffusion. The peak of the curve is achieved when the relation

$$\omega \cdot \tau_{eff} \sim 1 \tag{6.3}$$

is satisfied, where τ_{eff}

$$\frac{1}{\tau_{eff}} = \frac{1}{\tau_N} + \frac{1}{\tau_B} \tag{6.4}$$

is the total correlation time of the particle at the peak's frequency, shows that the two main contribution, coming from Néel and Brown relaxation times, drastically changes in the two media: in an aqueous environment, the Nèel contribution is still comparable with the dominant Brownian time, for which the NPs are able to rotate easier inside the matrix and interact faster with the surrounding water molecules. This is indeed reduced in case of gel-solutions, where the particles and the water molecules are roughly immobilized. The total effective time is then dominated by the Néel's contribution, associated to the magnetic moments of the nanoparticles and their anisotropy energy.

In Figure 6.9, the dumbbell water dispersion (DB_0.1_mM_H_2O) has been compared with *ENDOREM* (a commercial superparamagnetic contrast agent made of a mixture of magnetite (Fe_3O_4) and maghemite (γ-Fe_2O_3) and coated with dextran (a hydrophilic polysaccharide) no longer commercially available [45]) to assess its effectiveness and potential capabilities as contrast agents.

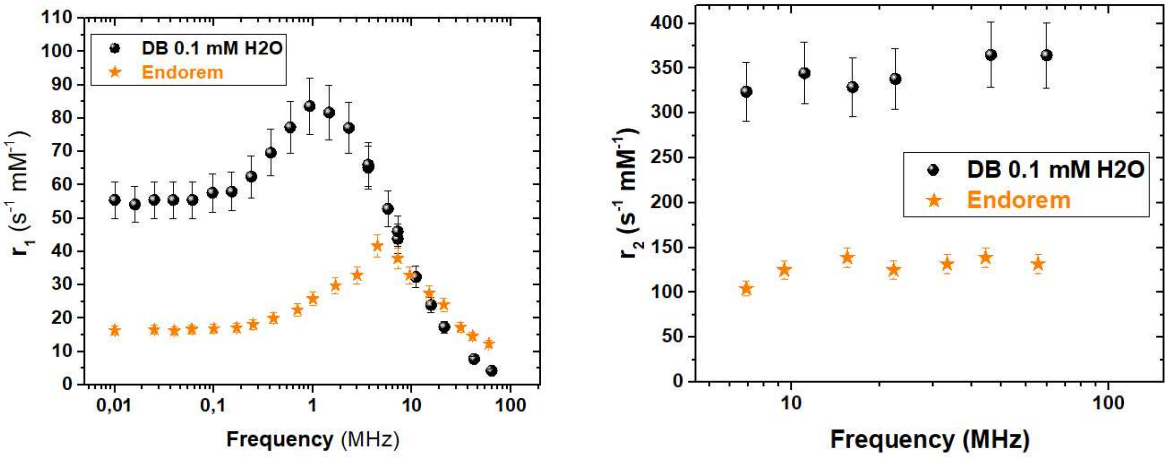

(a) *(b)*

Figure 6.9: *Comparison of longitudinal (a) and transverse (b) relaxation profiles of DB_0.1_mM_H_2O (black circles) with ENDOREM (orange stars).*

Comparing the two samples, it emerges that the DB_0.1_mM_H_2O is characterized by a general higher longitudinal and transverse relaxivity with respect to ENDOREM, showing at the

same time a much higher r_1 peak value of 80 $s^{-1}mM^{-1}$ at 1 MHz against the 42 $s^{-1}mM^{-1}$ at 4.5 MHz. As these particles have a superparamagnetic core, they are expected to be more effective in shortening the T_2 nuclear relaxation time, and it resulted that, at the clinical field of 1.5 T, and in the [7.2-63.86] MHz frequency range, they are ~3 times more efficient than the ENDOREM.

The efficiency of a contrast agent for MRI applications is determined by its ability to enhance the water protons relaxation rate per unit of concentration, and is quantified by the relaxivity. The r_2/r_1 ratio allows to classify a magnetic sample as a T_1- or T_2-relaxing contrast agent (CA), depending on whether the ratio is below or above 2, respectively.

Magnetite dispersions are known to be effective negative relaxing agents, and our results are consistent with this behavior in both water and agarose-gel matrices, as shown in Table 6.3.

Sample type	**Frequency (MHz)**	$\mathbf{r_1}$ **($s^{-1}mM^{-1}$)**	$\mathbf{r_2}$ **($s^{-1}mM^{-1}$)**	$\mathbf{r_2/r_1}$
DB_0.1_mM_H_2O	63.864	4.27	364	85
DB_0.1_mM_Agar	63.864	2.33	149	64
DB_0.2_mM_Agar	63.864	2.6	177	68

Table 6.3: *r_1, r_2 and r_2/r_1 values of DB_0.1_mM_H_2O, DB_0.1_mM_Agar and DB_0.2_mM_Agar at 63.864 MHz.*

At 1.5 T, the water dispersion has a r_2 value $\sim$ 2.5 times more efficient than the agarose samples. This can be expected by the aqueous solution since the interactions with the surrounding water molecules are facilitated. On the other side, the agarose environment, supposed to mimic the biological tissue network and possibly simulate in-vivo situations, tends to reduce the dephasing caused by the agent and so its relaxing effect.

6.3.2 Au-Fe_3O_4 nano-urchins shaped agarose profiles

The relaxivity profiles of the Au-Fe_3O_4 nano-urchins shaped particles in agarose 1%w are presented in Figure 6.10, with the same observations in terms of experimental error considered for dumbbell dispersions. These NPs feature the same magnetic core as dumbbell NPs, but with a larger gold component distributed in an urchin-like morphology.

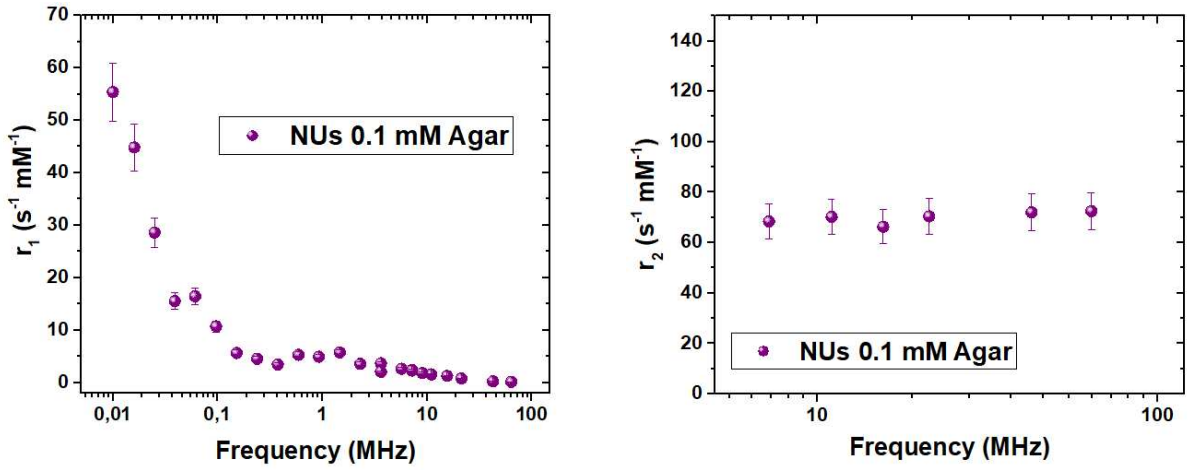

(a) *(b)*

Figure 6.10: *Longitudinal r_1 (a) and transverse r_2 (b) NMRD profiles of the NU_0.1_mM_Agar, acquired at room temperature.*

The NUs sample shows a different frequency behavior compared to dumbbell nanoparticles, in the same agarose medium (see Figure 6.11): a rapid increase of r_1 for frequencies below 0.1 MHz, and a strong reduction of r_1 values in almost all the studied frequency range, with the r_1 peak at 1.47 MHz (r_1 = 5.73 $s^{-1}mM^{-1}$).

The explanation of this important change in the longitudinal profile can be attributed to two main contributions: the increased Brownian relaxation time due to the agarose viscosity and the hydrodynamic volume of the particle itself (which is characterized by an hydrodynamic diameter of 130.3 nm, much larger if compared to the DB NPs), and the gold component that partially encloses the magnetic core, for which the distance between the core and the water molecules is further increased and their dipolar interaction is reduced (see inner sphere mechanism in Chapter 3), and the magnetite surface exposed to the medium is reduced. The overall effect is then reflected in the higher frequency range, where the relaxivity does not show values above 10 $s^{-1}mM^{-1}$, much lower if compared to those obtained for DBs, whose r_1 peaks approximately reached 30 $s^{-1}mM^{-1}$. Concerning the low frequency r_1 increment, one possible explanation could be the presence of a weak paramagnetic component in the sample. In particular, the contribution of surface spins (*e.g.*, Fe^{3+} ion defects sites at the Au-Fe interface) fluctuating at lower frequencies has been tentatively hypothesized, although this remains to be confirmed. Their contribution can be described according to the outer sphere mechanism, where bulk water molecules interact with the magnetic core (and so eventual surface spins) by diffusing in the vicinity of the nanoparticle, and so causing protons relaxation.

For the r_2 profile, the transverse relaxation in the frequency range 7.2 - 63.864 MHz remained constant as the previous dumbbell dispersions (see Figure 6.11 (b)), although the average particles r_2 efficiency is reduced from almost 150 $s^{-1}mM^{-1}$ to nearly 70 $s^{-1}mM^{-1}$. This result might be

traced back to the increased gold component that has been added to the magnetite core, which could suppress the magnetic interactions with the surrounding water molecules and approximately halve their effect.

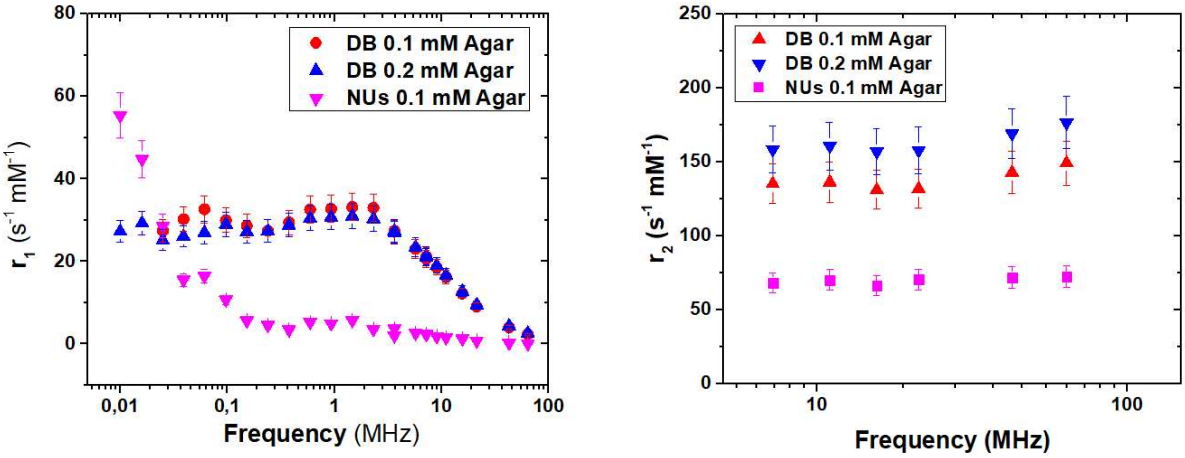

(a) *(b)*

Figure 6.11: *Comparison of the longitudinal r_1 (a) and transverse r_2 (b) NMRD profiles of the three in-agarose dispersions (DB_0.1_mM_Agar, DB_0.2_mM_Agar and NU_0.1_mM_Agar).*

In figure Figure 6.12, a complete line-up of all dispersions profiles is reported and shown in the same graph.

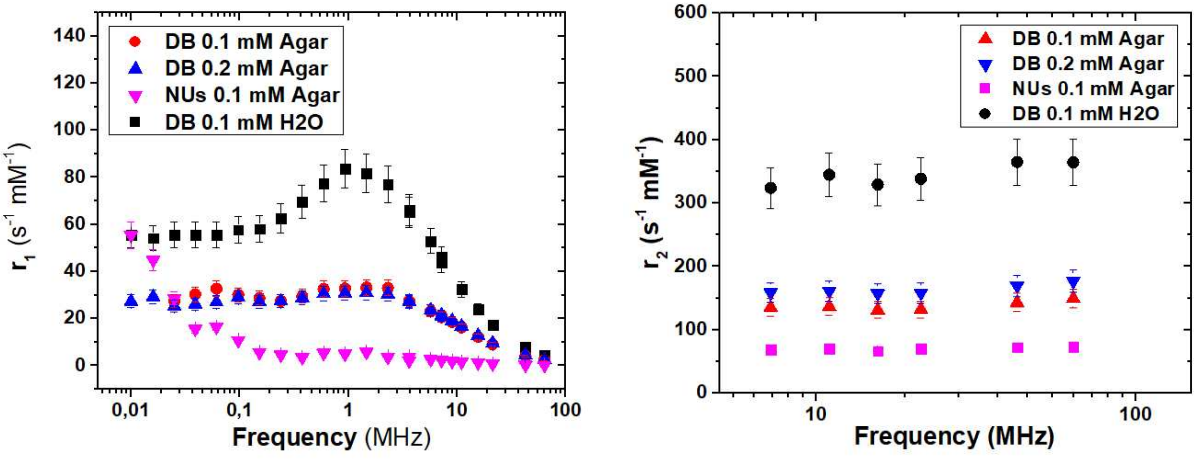

(a) *(b)*

Figure 6.12: *Comparison of the longitudinal r_1 (a) and transverse r_2 (b) NMRD profiles of the three DB dispersions and NUs.*

The r_2/r_1 values calculated at the clinical magnetic field intensity of 1.5 T, corresponding to a Larmor frequency of 63.864 MHz, are reported in Table 6.4.

As shown, the NUs can also be attributed as T_2-negative CAs (as expected by a ferrite magnetic core), as the r_2/r_1 ratio is higher than 2.

Sample type	Frequency (MHz)	r_1 ($s^{-1}mM^{-1}$)	r_2 ($s^{-1}mM^{-1}$)	r_2/r_1
DB_0.1_mM_H_2O	63.864	4.27	364	85
DB_0.1_mM_Agar	63.864	2.33	149	64
DB_0.2_mM_Agar	63.864	2.6	177	68
NU_0.1_mM_Agar	63.864	0.21	72	345

Table 6.4: *r_1, r_2 and r_2/r_1 values of the four dispersions at 63.864 MHz.*

6.3.3 RMG fit of the longitudinal relaxation profiles

To analyze the four different longitudinal r_1 relaxation profiles, the heuristic model proposed by Roch-Müller-Gillis (RMG), introduced and described in Chapter 3, was adopted to provide a semi-empirical description of the relaxation behavior of superparamagnetic NPs. This model permits to extract particles parameters, such as the saturation magnetization, the magnetic core radius, the Néel's relaxation time, the distance of minimum approach, and others, from the relaxivity curve. The heuristic formulation was initially applied to both aqueous and agarose sample curves. However, it appeared to be effective only for the DB_0.1_mM_H_2O, and incompatible with the other three agarose-based dispersions. To better predict their different behavior and refine its description, a modified version of the RMG model was employed. In this version, the effective correlation time characterizing both the Ayant and Freed spectral density was corrected by explicitly including the Brownian rotational time τ_B, which accounts for the contribution of the particle rotational dynamics to the fluctuation of the local magnetic field. This modification led to a more accurate fit, enabling the RMG model to realistically represent the relaxation mechanisms for particles where the Brownian relaxation time is comparable to, or longer than the Nèel relaxation time. It is important to note that the RMG model requires initialization through the assignment of initial values for its key parameters, along with predefined variation ranges. The model then performs parameter optimization by searching for the best-fitting values that minimize the difference between the experimental data and the prediction of the model.

Fitting of DB nanoparticles dispersed in water

The first longitudinal relaxivity profile analyzed was that of DB_0.1_mM_H_2O. From its analysis and parameter estimation, the accuracy of the chosen parameters for the in-agarose curves fit and the suitability of the modified RMG model were ascertained. The saturation magnetization was initially set at 73 emu/g (according to the magnetic measurements carried out by the Florence research group on dumbbell samples) and allowed to vary within a 10% error. The core radius r was set at the value determined by TEM characterization (5.8 nm) with the relative TEM error in the magnetite component. The theoretical value of the water diffusion coefficient was fixed

at the theoretical value $2.3 \cdot 10^{-9}$ m^2/s for the aqueous solution. The temperature was fixed at 300 K.

The fitting curves obtained are presented in Figure 6.13. The same profile was fitted with both the regular and the modified RMG models to prove the consistency of the two different approaches, resulting in their overlap (Fig. 6.13c). No discrepancy has been achieved in their superposition, meaning that the two models are reproducing the same behavior and that the Brownian term contribution is not directly implied in the observed relaxation.

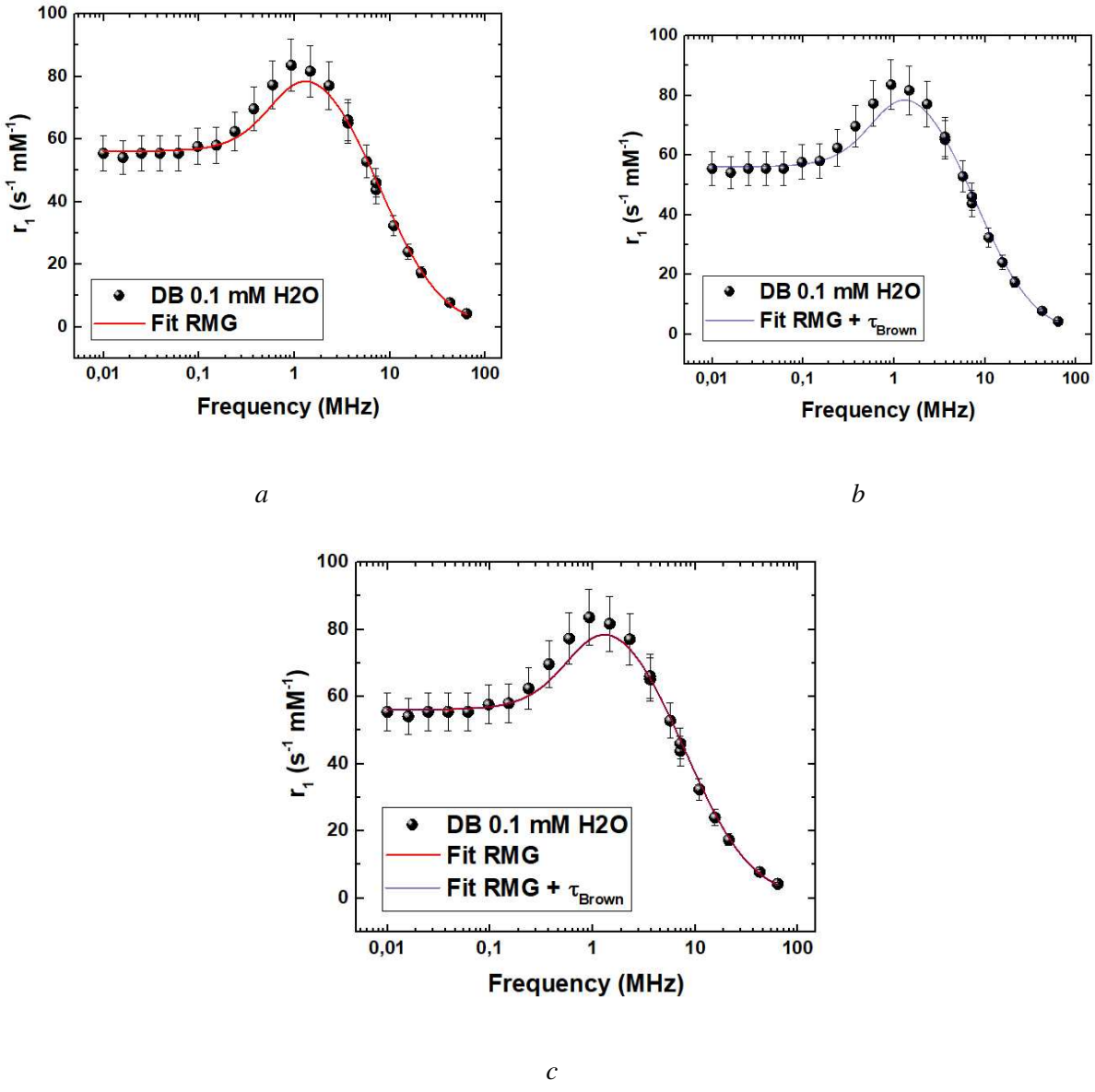

Figure 6.13: *Fig. (a) shows the fit obtained using the heuristic Roch–Müller–Gillis (RMG) model without considering the Brownian contribution, while fig. (b) displays the fit including the Brownian term. In fig. (c), both fits are compared on the same plot to highlight the differences between the two models, resulting in a complete overlap.*

The parameters evaluated from the fit will be shown and discussed in the next session, in comparison with the results obtained from the analysis of the agarose-gel dispersions data.

Fitting of DB and NUs nanoparticles dispersed in agarose 1%w

The parameters deduced from the fitting curves of the DB sample dispersed in water were then used as guidelines for the initialization of the parameters used to fit the following samples dispersed in agarose, since the DB particles are the same but dispersed in agarose, and the magnetic component of NUs is the same as the DB heterodiemrs. In fact, it is expected that some parameters such as magnetization, magnetic core radius and Nèel relaxation time remain within the same range of values assumed by these dispersion (varying by no more than 10%), being the magnetic core shared bewteen all the studied particles. So, all parameters were initialized at the values obtained from the fit of DB in water, particularly M_S was fixed at the value obtained from a first fitting procedure, to reduce the number of free parameters. Concerning the diffusion coefficient of agarose 1%w, it was difficult to assess a specific value as for the case of water, which is theoretically known, since diffusion in the agarose-gel varies according to multiple factors such as the gelation temperature and the kind of particle. To estimate it, in first approximation, the value was set free in the fit and allowed to vary between two orders of magnitude (10^{-10} and $2.3 \cdot 10^{-9}$), while the other parameters, such as Ms and r, were fixed. No significant changes were observed. Following a deeper research on the available literature, Sack et al [46] reported a value of 2188 ± 96 $\mu m^2/s$ for agarose diffusion, corresponding to $2.188 \cdot 10^{-9}$ m^2/s, approximately equal to water diffusion. For the agarose viscosity η, instead, the value was derived from the relaxation time τ_B for particles with an average magnetic diameter of 10-15 nm (which is on the order of 10^{-5} seconds) and it has been estimated to be 8.4 mPa·s.

The resulting fitting curves of DB particles dispersed in agarose at 0.1 and 0.2 mM concentrations are shown in Figure 6.14, where the modified RMG model has been used.

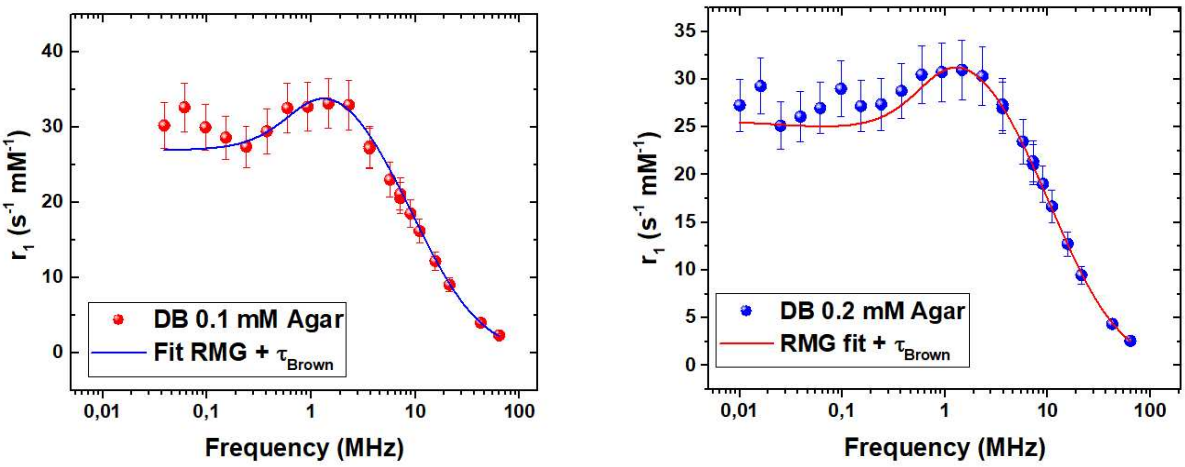

Figure 6.14: *Modified RMG fit of the DB Agar dispersions. Fig. (a) shows the DB_0.1_mM_Agar fit and fig. (b) the DB_0.2_mM_Agar fit.*

A first attempt with the modified RMG model was done on the NUs sample but no coherent results have been obtained. The model, as expected, was unable to predict and reproduce the low frequency region, that might be influenced by the possible presence of surface spins and therefore the additional paramagnetic component has been hypothesized. For this reason, the model was further modified by adding a Lorentzian contribution to the fitting function, described by a certain unknown correlation time τ_W.

The fitting was first performed using the modified RMG model in the frequency range [0.1 - 63.864] MHz, where no significant paramagnetic contribution is observed and the relaxation profile follows the expected behavior of a superparamagnetic nano-urchin embedded in agarose. After this first step, the main parameters, such as the Néel relaxation time τ_N, saturation magnetization M_s, core radius r, parameter P used to evaluate the anisotropy level of the NPs, and the distance of minimum approach dist, were estimated. These parameters were then employed into the Lorentzian-added modified RMG model, trying to fit the low-frequency region ($\omega < 0.1$ MHz) and gain knowledge of the correlation time of the Lorentzian component associated to the additional paramagnetic contribution.

The resulting curve fit is shown in Figure 6.15.

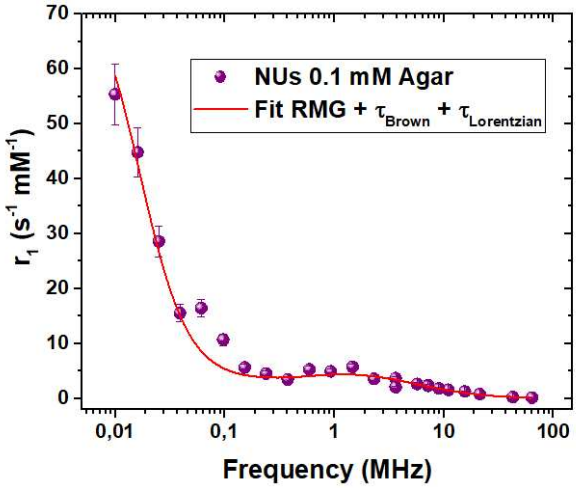

Figure 6.15: *RMG fit for NUs sample. The fit function was further modified to also include and study the low-frequency region.*

The Lorentzian correlation time τ_L was estimated from the fit and was found to be (1 ± 0.2) 10^{-13} seconds.

Fit-derived parameters

The parameters evaluate from each fit are τ_N and τ_B, saturation magnetization M_s, magnetic core radius r_{fit}, distance of minimum approach $dist$ and the anisotropy parameter P (the parameter specifically included in the heuristic model that allows high ($P = 0$) or low anisotropy ($P = 1$) conditions to be reproduced). The resulting values are shown in Table 6.5:

Table 6.5: *Parameters obtained from RMG fitting for the all studied samples. Saturation Magnetization M_S, core radius r_{fit}, parameter P, minimum approach distance dist. Néel relaxation time τ_N and Brown relaxation time τ_B.*

Parameter	DB_0.1_mM_H_2O	DB_0.1_mM_Agar	DB_0.2_mM_Agar	NU_0.1_mM_Agar
M_s (emu/g)	80	71	80	79
r_{fit} (nm)	7 ± 0.8	7 ± 1.3	7 ± 0.8	7 ± 1.5
τ_N (s)	$(2.3 \pm 0.2) \times 10^{-8}$	$(3 \pm 2) \times 10^{-8}$	$(3.0 \pm 0.4) \times 10^{-8}$	$(3 \pm 1) \times 10^{-8}$
τ_B (s)	$(3.4 \pm 0.3) \times 10^{-6}$	$(2.1 \pm 0.3) \times 10^{-5}$	$(1.6 \pm 0.2) \times 10^{-5}$	$(5.6 \pm 2.5) \times 10^{-5}$
P	0 ± 0.1	0 ± 0.5	0.05 ± 0.09	0 ± 0.3
$dist$ (nm)	10.4 ± 0.2	9.4 ± 0.3	8.5 ± 0.2	13 ± 2

Here, the reported errors are those obtained from the fit, with the sole exception of τ_B which was studied according to the error propagation of the viscosity η and hydrodynamic volume V_H in its formulation:

$$\tau_B = \frac{3\eta V_H}{k_B T} \tag{6.5}$$

The Nèel relaxation times τ_N are nearly constant across the four samples, ranging within the 0.2 - 0.3 ns interval. This could imply that the internal magnetic dynamics of the magnetite cores is not particularly affected by a change in the surrounding medium and by the presence of gold branches, as can be expected by particles of similar core dimension and composition. The Brownian relaxation time τ_B, instead, has decreased of an order of magnitude in the transition from water ($\sim 10^{-6}$ s) to agarose ($\sim 10^{-5}$ s), confirming the reduced rotational motion within the gel matrix. Moreover, NUs reported a value of τ_B that is nearly 3 times that of the DB_0.1_mM_Agar, reflecting the enlarged hydrodynamic radius and the reduced rotational freedom of NPs inside the gel. The saturation magnetization, which ranges from 71 to 80 emu/g, reported values that are consistent with the bulk magnetite, indicating that neither the agarose environment nor the gold component alters the magnetic properties of the core. The latter, which has given dimensions around 7 nm, is in good agreement with the TEM measurement of $r = (6 \pm 1)$ nm. The parameter P is basically 0 for all the samples, further reflecting the high anisotropy of the dumbbell and nano-urcins structures. Finally, the minimum approach distance *dist* (estimated from the inflection point at high frequencies where it follows $\tau_D \cdot \omega_I \sim 1$, with τ_D = (dist)^2/D and ω_I the proton Larmor frequency) decreases slightly from water to agarose and then increases again in the NUs sample, probably due to the gold shell that acts as a barrier and prevents nearby water molecules from getting closer to the magnetic core. It can be observed that in the case of dumbbell particles (both in water and agaorse media), *dist* hints a non thick layer of 2.5 - 3.5 nm, which turns thicker in the case of NUs ($\sim$ 5 nm).

Overall, the fitting analysis suggests that the relaxation of the dumbbell samples is primarily governed by the Néel relaxation, with the Brownian dynamics being suppressed in the passage from water to the gel-network and with the increasing particle size.

CONCLUSIONS

This work presented a detailed investigation of the magnetic and relaxometric behavior of hybrid gold–iron oxide (Au–Fe_3O_4) nanoparticles designed as potential MRI contrast agents. Two different morphologies were examined: dumbbell-shaped Au–Fe_3O_4@CTAB nanoparticles and nano-urchin-shaped Au–Fe_3O_4@PEG nanoparticles with elongated spikes. Both systems shared the same magnetite core, with an average diameter of 11.6 nm, but differed in geometry and surface configuration, enabling a comparison of how structure and environment influence magnetic relaxation mechanisms.

Four dispersions were studied in total: one aqueous dispersion of dumbbell-like nanoparticles (DB_0.1_mM_H_2O), two samples of dumbbell-like nanoparticles embedded in 1%w agarose gel at different iron concentrations (0.1 and 0.2 mM), and one sample of nano-urchin-like nanoparticles embedded in 1%w agarose at a concentration below 0.1 mM. Agarose-gel was selected as a tissue-mimicking matrix to reproduce the restricted diffusion conditions of biological environments.

Comprehensive physicochemical and magnetic characterizations confirmed the successful synthesis and structural integrity of all samples. TEM analysis revealed well-defined morphologies and size distribution of the MNPs, estimating a magnetite core diameter of (11.6 ± 2.4) nm and a gold component with a diameter of (8.2 ± 1.8) nm for the dumbbells and (131 ± 26) nm for the nano-urcins. The XRD confirmed two different crystalline phases, compatible with the characteristic cubic spinel structure of the magnetite and the face-centered cubic structure of gold, whereas no impurity peaks have been recognized in the pattern. SQUID magnetometry showed the typical superparamagnetic behavior of Fe_3O_4 nanoparticles at room temperature (300 K), with a pronounced divergence between the ZFC-FC branches of the curves. The maxima of the ZFC curves, corresponding to the blocking temperatures (T_B) of the samples, were found at: 144 ± 50 K for the aqueous dispersion, 160 ± 40 K for the dumbbells in agarose and 125 ± 40 K for the nano-urcins. Moreover, the ZFC/FC curves showed a broad maximum centered around T_B, suggesting the presence of a wide range of anisotropy energy barriers and a degree of

size polydispersity into the analyzed samples. The NUs sample was further analyzed via DLS, reporting an average hydrodynamic diameter of (130 ± 38) nm, in good agreement with the TEM evaluation.

Relaxometric measurements provided the longitudinal (r_1) and transverse (r_2) nuclear relaxation profiles in the frequency range of [0.01 - 63.864] MHz and [7.2 - 63.864] MHz, for r_1 and r_2, respectively. The peak of the longitudinal relaxivity curve was around 1 MHz for all samples, reflecting the fact that they are made by the same magnetic core; the resulting peak magnitude were 84 $s^{-1}mM^{-1}$ for the DB_0.1_mM_H_2O, nearly 30 $s^{-1}mM^{-1}$ for DB 0.1 and 0.2 mM Agar and 5.73 $s^{-1}mM^{-1}$ for the NU_0.1_mM_Agar. Moreover, no concentration effect on the DB 0.1 and 0.2 mM Agar appeared (longitudinal and transverse NMRD profiles that overlap within the experimental error), suggesting that the relaxometric properties of the sample are not affected by a variation of the concentration of magnetic ions (within the studied frequency range). The dumbbell nanoparticles in water exhibited the highest transverse relaxivity ($r_2 \sim 364$ $s^{-1}mM^{-1}$) and a large r_2/r_1 ratio of about 85 at the frequency of 63.864 MHz (which is the Larmor frequency produced by a static magnetic field of intensity 1.5 T, as used in clinical application), confirming their high efficiency as T_2-weighted contrast agents. When embedded in agarose, both r_1 and r_2 decreased ($r_2 \sim$ 150–175 $s^{-1}mM^{-1}$), reflecting the restricted Brownian motion within the gel. The nano-urchin sample displayed the lowest r_1 peak(~ 5.7 $s^{-1}mM^{-1}$) and moderate r_2 values (~ 72.5 $s^{-1}mM^{-1}$ at 63.864 MHz), with, at the same time, an extremely high r_2/r_1 ratio (> 300), confirming a T_2-type relaxation behavior. The transverse relaxivity r_2 of DB water sample was compared to that of ENDOREM, a commercially withdrawn contrast agent. The dumbbell in water resulted almost 3 times more efficient than ENDOREM, potentially resulting in a more efficient T_2-negative CA.

The Nuclear Magnetic Relaxation Dispersion (NMRD) profiles were analyzed using a heuristic model from Roch–Müller–Gillis (RMG) theory. The model fit makes use of Curie's relaxation mechanism to analyze the high frequency region of the NMRD profile, while for lower frequencies, the anisotropy dictates the behavior of the relaxation. It can be used for spherical nanoparticles with uniaxial anisotropy and adapted for different morphologies as well. In particular, three variants of the RMG model were used to perform the fit of the profiles: a "regular" RMG model, which does not consider the Brownian relaxation time term, a modified RMG model that accounts for τ_B in the total correlation time that regulates the formulation of the Ayant and Freed's spectral density, and a third model specifically used for the NUs sample curve to fit the lower frequency region that is apparently generated by an additional paramagnetic component (the presence of surface spins was hypothesized).

For the dumbbell water dispersion, the fit obtained from both models (with/without Brownian relaxation) were nearly identical, indicating that the Néel relaxation dominates the relaxation dynamics, with a characteristic τ_N of 2–3·10^{-8} s and a longer τ_B of 3·10^{-6} s in water. In agarose,

the regular RMG model was unable to reproduce the data and give an appreciable fit of the curve. In fact, τ_B increased to $2{\cdot}10^{-5}$ s for dumbbells and to $5.6{\cdot}10^{-5}$ s for the nano-urchins, confirming further suppression of Brownian motion. The other fitted parameters, such as M_s, r, P and $dist$, were first evaluated and studied for DB_0.1_mM_H_2O, resulting in M_s = 80 emu/g, r = 7 nm, P = 0 and dist ~ 10 nm. The agarose dispersions have shown similar values of M_s and r, being 71 emu/g and 7 nm for the DB 0.1 mM, 80 emu/g and 7 nm for DB 0.2 mM and 79 emu/g and 6.7 nm for the NUs 0.1 mM, in good agreement with the magnetic characterization performed with the SQUID (for M_s) by the research group in Florence that found a value of 73 and 72 emu/g for the DB and NU, respectively. The effective magnetite particle radius was found to be 7 nm, consistent with the error of the TEM measurement. The parameter P, which describes the anisotropy level of the system, also remained stable at 0, meaning that those crystals are characterized by a high anisotropy degree, as expected for dumbbell and urchin-like nanoparticles. Lastly, the minimum approach distance *dist*, representing the average distance between the magnetic center and the protons, gave slightly different values, ranging from 10.4 nm for the DB_0.1_mM_H_2O, 9.4 and 8.5 nm for the DB 0.1 and 0.2 mM Agar and nearly 13 nm for NUs. Those values of *dist* differ from the effective core radius for 1.5-5 nm nano-meters, indicating that the presence of a layer around the magnetite core creates a certain separation from the surrounding water molecules so that they cannot get closer to the magnetic center.

Overall, these fitted parameters support the interpretation that the relaxation in the dumbbell samples is primarily governed by Néel fluctuations, while the Brownian contribution becomes increasingly negligible in more viscous or larger systems such as agarose-embedded or gold-coated nanoparticles.

BIBLIOGRAPHY

[1] D. Jiles, *Introduction to Magnetism and Magnetic Materials*, 3rd ed. CRC Press, 2015. DOI: 10.1201/b18948.

[2] C. Kittel, *Introduction to Solid State Physics*, 8th ed. Hoboken, NJ: John Wiley & Sons, 2005.

[3] V. K. Varadan, L. Chen, and J. Xie, *Nanomedicine: Design and Applications of Magnetic Nanomaterials, Nanosensors and Nanosystems*. Chichester, UK: Wiley, 2008.

[4] S. Blundell, *Magnetism in Condensed Matter*. Oxford; New York: Oxford University Press, 2001.

[5] N. Manini, *Introduction to the Physics of Matter: Basic Atomic, Molecular, and Solid-State Physics*. Cham, Switzerland: Springer, 2014.

[6] P. Sandgren and I. Snowball, "Application of mineral magnetic techniques to paleolimnology," in *Environmental Magnetism*, M. E. Evans and F. Heller, Eds., vol. 2, Springer, 2006, pp. 217–237, ISBN: 1-4020-0628-4. DOI: 10.1007/0-306-47670-3_8.

[7] B. Issa, I. M. Obaidat, B. A. Albiss, and Y. Haik, "Magnetic nanoparticles: Surface effects and properties related to biomedicine applications," *International Journal of Molecular Sciences*, vol. 14, no. 11, pp. 21 266–21 305, 2013. DOI: 10.3390/ijms141121266.

[8] L. Kafrouni and O. Savadogo, "Recent progress on magnetic nanoparticles for magnetic hyperthermia," *Progress in Biomaterials*, vol. 5, no. 3-4, pp. 147–160, 2016. DOI: 10.1007/s40204-016-0054-6.

[9] F. Burrows, "A model of magnetic hyperthermia," Ph.D. dissertation, The University of York, Department of Physics, Mar. 2012.

[10] X. Batlle and A. Labarta, "Finite-size effects in fine particles: Magnetic and transport properties," *Journal of Physics D: Applied Physics*, vol. 35, no. 6, R15–R42, Mar. 2002. DOI: 10.1088/0022-3727/35/6/201. [Online]. Available: https://dx.doi.org/10.1088/0022-3727/35/6/201.

[11] R. Rosensweig, "Heating magnetic fluid with alternating magnetic field," *Journal of Magnetism and Magnetic Materials*, vol. 252, pp. 370–374, 2002, Proceedings of the 9th International Conference on Magnetic Fluids, ISSN: 0304-8853. DOI: https://doi.org/10.1016/S0304-8853(02)00706-0. [Online]. Available: https://www.sciencedirect.com/science/article/pii/S0304885302007060.

[12] O. Fruchart, "Lecture notes on nanomagnetism," 2011. [Online]. Available: https://api.semanticscholar.org/CorpusID:202614351.

[13] Q. A. Pankhurst, J. Connolly, S. K. Jones, and J. Dobson, "Applications of magnetic nanoparticles in biomedicine," *Journal of Physics D: Applied Physics*, vol. 36, no. 13, R167–R181, 2003. DOI: 10.1088/0022-3727/36/13/201.

[14] S. Dutz and R. Hergt, "Magnetic particle hyperthermia—a promising tumour therapy?" *Nanotechnology*, vol. 25, no. 45, p. 452 001, 2014. DOI: 10.1088/0957-4484/25/45/452001.

[15] P. Conte and G. Alonzo, "Environmental nmr: Fast-field-cycling relaxometry," in *eMagRes*. John Wiley & Sons, Ltd, 2013, pp. 389–398, ISBN: 9780470034590. DOI: https://doi.org/10.1002/9780470034590.emrstm1330. eprint: https://onlinelibrary.wiley.com/doi/pdf/10.1002/9780470034590.emrstm1330. [Online]. Available: https://onlinelibrary.wiley.com/doi/abs/10.1002/9780470034590.emrstm1330.

[16] R. W. Brown *et al.*, *Magnetic Resonance Imaging: Physical Principles and Sequence Design*. John Wiley & Sons, 2014, cit. alle pp. 1, 40, 43, 45.

[17] A. Rigamonti *et al.*, *Structure of Matter: An Introductory Course with Problems and Solutions*. Springer-Verlag Italia, 2009, cit. a p. 39.

[18] S. Laurent, D. Forge, M. Port, *et al.*, "Magnetic iron oxide nanoparticles: Synthesis, stabilization, vectorization, physicochemical characterizations, and biological applications," *Chemical Reviews*, vol. 108, no. 6, pp. 2064–2110, 2008. DOI: 10.1021/cr068445e.

[19] Q. L. Vuong, P. Gillis, A. Roch, and Y. Gossuin, "Magnetic resonance relaxation induced by superparamagnetic particles used as contrast agents in magnetic resonance imaging: A theoretical review," *Wiley Interdisciplinary Reviews: Nanomedicine and Nanobiotechnology*, vol. 9, no. 6, e1468, 2017, Review. DOI: 10.1002/wnan.1468.

[20] C. Burtea, L. Vander Elst, and R. Muller, "Contrast agents: Magnetic resonance," *Handbook of experimental pharmacology*, vol. 185, pp. 135–65, Feb. 2008. DOI: 10.1007/978-3-540-72718-7_7.

[21] A. Roch, R. N. Muller, and P. Gillis, "Theory of proton relaxation induced by superparamagnetic particles," *The Journal of Chemical Physics*, vol. 110, no. 11, pp. 5403–5411, Mar. 1999, ISSN: 0021-9606. DOI: 10.1063/1.478435. eprint: https://pubs.aip.org/aip/jcp/article-pdf/110/11/5403/19111110/5403_1_online.pdf. [Online]. Available: https://doi.org/10.1063/1.478435.

[22] Q. L. Vuong, J.-F. Berret, J. Fresnais, Y. Gossuin, and O. Sandre, "A universal scaling law to predict the efficiency of magnetic nanoparticles as mri t_2-contrast agents," *Advanced Healthcare Materials*, vol. 1, no. 4, pp. 502–512, Jul. 2012, ISSN: 2192-2640. DOI: 10.1002/adhm.201200078. [Online]. Available: https://doi.org/10.1002/adhm.201200078.

[23] V. F. Cardoso, A. Francesko, C. Ribeiro, M. Bañobre-López, P. Martins, and S. Lanceros-Mendez, "Advances in magnetic nanoparticles for biomedical applications," *Advanced Healthcare Materials*, vol. 7, no. 5, p. 1 700 845, Mar. 2018. DOI: 10.1002/adhm.201700845.

[24] M. Ali Dheyab, A. Abdul Aziz, M. S. Jameel, and P. Moradi Khaniabadi, "Recent advances in synthesis, medical applications and challenges for gold-coated iron oxide: Comprehensive study," *Nanomaterials*, vol. 11, no. 8, 2021, ISSN: 2079-4991. DOI: 10.3390/nano11082147. [Online]. Available: https://www.mdpi.com/2079-4991/11/8/2147.

[25] K. Chatterjee, S. Sarkar, K. Jagajjanani Rao, and S. Paria, "Core/shell nanoparticles in biomedical applications," *Advances in Colloid and Interface Science*, vol. 209, pp. 8–39, 2014, ISSN: 0001-8686. DOI: https://doi.org/10.1016/j.cis.2013.12.008. [Online]. Available: https://www.sciencedirect.com/science/article/pii/S0001868613001899.

[26] D. Duchêne and R. Gref, "Small is beautiful: Surprising nanoparticles," *International Journal of Pharmaceutics*, vol. 502, no. 1-2, pp. 219–231, Apr. 2016. DOI: 10.1016/j.ijpharm.2016.02.016.

[27] Y. Li, M. Zhai, and H. Xu, "Controllable synthesis of sea urchin-like gold nanoparticles and their optical characteristics," *Applied Surface Science*, vol. 498, p. 143 864, 2019, ISSN: 0169-4332. DOI: 10.1016/j.apsusc.2019.143864. [Online]. Available: https://www.sciencedirect.com/science/article/pii/S0169433219326807.

[28] E. Toth, L. Helm, and A. E. Merbach, "Relaxivity of gadolinium (iii) complexes: Theory and mechanism," in *The Chemistry of Contrast Agents in Medical Magnetic Resonance Imaging*, 2nd ed., Chichester, UK: John Wiley & Sons, 2001, pp. 1–47.

[29] Y. Wu, X. Yang, X. Yi, Y. Liu, Y. Chen, *et al.*, "Magnetic nanoparticle for biomedicine applications," *Journal of Nanotechnology, Nanomedicine and Nanobiotechnology*, vol. 2, p. 003, 2014.

[30] E. Christou, J. R. Pearson, A. M. Beltrán, *et al.*, "Iron–gold nanoflowers: A promising tool for multimodal imaging and hyperthermia therapy," *Pharmaceutics*, vol. 14, no. 3, p. 636, 2022. DOI: 10.3390/pharmaceutics14030636.

[31] M. F. Sanad, B. P. Meneses-Brassea, D. S. Blazer, S. Pourmiri, G. C. Hadjipanayis, and A. A. El-Gendy, "Superparamagnetic fe/au nanoparticles and their feasibility for magnetic hyperthermia," *Applied Sciences*, vol. 11, no. 14, p. 6637, 2021. DOI: 10.3390/app11146637.

[32] J. B. Vines, J. H. Yoon, N. E. Ryu, D. J. Lim, and H. S. Park, "Gold nanoparticles for photothermal cancer therapy," *Frontiers in Chemistry*, vol. 7, p. 167, Apr. 2019. DOI: 10.3389/fchem.2019.00167.

[33] H. Yu, M. Chen, P. M. Rice, S. X. Wang, R. L. White, and S. Sun, "Dumbbell-like bifunctional au–fe_3o_4 nanoparticles," *Nano Letters*, vol. 5, no. 2, pp. 379–382, 2005. DOI: 10.1021/nl048539f.

[34] V. Amendola, S. Scaramuzza, L. Litti, *et al.*, "Magneto-plasmonic au-fe alloy nanoparticles designed for multimodal sers-mri-ct imaging," *Small*, vol. 10, no. 12, pp. 2476–2486, 2014, ISSN: 1613-6829. DOI: 10.1002/smll.201303372.

[35] J. Gao, H. Gu, and B. Xu, "Multifunctional magnetic nanoparticles: Design, synthesis, and biomedical applications," *Accounts of Chemical Research*, vol. 42, no. 8, pp. 1097–1107, 2009. DOI: 10.1021/ar9000026.

[36] D. A. Long, *The Raman Effect: A Unified Treatment of the Theory of Raman Scattering by Molecules*. Chichester: John Wiley & Sons, 2002.

[37] K. D. Kneipp, "Raman spectroscopy of single molecules," *Single Molecules*, vol. 2, pp. 291–292, 2001. [Online]. Available: https://api.semanticscholar.org/CorpusID:94792820.

[38] J. F. Li, Y. F. Huang, Y. Ding, *et al.*, "Shell-isolated nanoparticle-enhanced raman spectroscopy," *Nature*, vol. 464, pp. 392–395, 2010. [Online]. Available: https://api.semanticscholar.org/CorpusID:4373801.

[39] M. Salloum, R. H. Ma, D. Weeks, and L. Zhu, "Controlling nanoparticle delivery in magnetic nanoparticle hyperthermia for cancer treatment: Experimental study in agarose gel," *International Journal of Hyperthermia*, vol. 24, no. 4, pp. 337–345, Jun. 2008. DOI: 10.1080/02656730801907937.

[40] R. K. Jain, "Transport of molecules, particles, and cells in solid tumors," *Annual Review of Biomedical Engineering*, vol. 1, no. 1, pp. 241–263, 1999. DOI: 10.1146/annurev.bioeng.1.1.241.

[41] D. B. Williams and C. B. Carter, *Transmission Electron Microscopy: A Textbook for Materials Science*, 2nd ed. Springer, 2009. DOI: 10.1007/978-0-387-76501-3.

[42] B. Cullity and S. Stock, *Elements of X-Ray Diffraction*, 3rd ed. Prentice Hall, 2001, ISBN: 978-0201610918.

[43] B. Berne and R. Pecora, *Dynamic Light Scattering: With Applications to Chemistry, Biology, and Physics*. Dover Publications, 2000, ISBN: 978-0486407262.

[44] M. Zahradník, "Dynamic control of magnetization for spintronic applications studied by magneto-optical methods," Ph.D. dissertation, Charles University, Prague, Czech Republic, Jun. 2019.

[45] M. Basini, A. Guerrini, M. Cobianchi, *et al.*, "Tailoring the magnetic core of organic-coated iron oxides nanoparticles to influence their contrast efficiency for magnetic resonance imaging," *Journal of Alloys and Compounds*, vol. 770, pp. 58–66, 2019, ISSN: 0925-8388. DOI: https://doi.org/10.1016/j.jallcom.2018.08.120. [Online]. Available: https://www.sciencedirect.com/science/article/pii/S0925838818329992.

[46] I. Sack, E. Gedat, J. Bernarding, G. Buntkowsky, and J. Braun, "Magnetic resonance elastography and diffusion-weighted imaging of the sol/gel phase transition in agarose," *Journal of Magnetic Resonance*, vol. 166, no. 2, pp. 252–261, 2004, ISSN: 1090-7807. DOI: https://doi.org/10.1016/j.jmr.2003.10.020. [Online]. Available: https://www.sciencedirect.com/science/article/pii/S1090780703003732.